UNIVERSITY OF MANITOBA

CONCEPTUAL DESIGN OF A SPACE VEHICLE FOR ORBITAL DEBRIS PROTECTION

4162 Thesis

Submitted by: Daniel Thomson
Student #: 7753146
Thesis Advisor: Dr. Igor Telichev
Date Submitted: 10/18/2013

Department of Mechanical & Manufacturing Engineering

ABSTRACT

As the orbital debris environment deteriorates, the threat to spacecraft is becoming increasingly significant. Additionally, current protection techniques leave them vulnerable to objects between 1 and 10 cm. The objective for this project was to design a “defender” space vehicle capable of shielding spacecraft from objects in this range of sizes. The design was divided into three stages: first, using SPH simulations, a shield capable of defeating large projectiles was designed based on existing shield types; next, a deployment mechanism that allowed the shield to be stored compactly for launch was designed and analyzed using a vector-based kinematics and dynamics method; finally, a general design of the service module was made. The final design consisted of an eight-layer shield with an umbrella-inspired deployment mechanism. It was 3 m in diameter by 7 m long with the shield folded and had a mass of 5100 kg; proving the feasibility of this measure.

ACKNOWLEDGEMENTS

Acknowledgements – advisor (IT), AC (SPH), WC, fam...

TABLE OF CONTENTS

LIST OF FIGURES

LIST OF TABLES

ACRONYMS AND ABBREVIATIONS

2D	2-Dimensional
3D	3-Dimensional
Al	Aluminum
CFRP	Carbon Fiber Reinforced Plastic
EOL	End of Life
EOS	Equation of State
ESA	European Space Agency
ESOC	European Space Operations Center
FEM	Finite Element Model
GEO	Geosynchronous Earth orbit
GTO	Geosynchronous Transfer Orbits
HEO	Highly Elliptical Orbits
HVI	Hypervelocity Impact
IADC	Inter-Agency Space Debris Coordination Committee
ISS	International Space Station
L2	Lagrangian Point 2
LEO	Low-Earth Orbit

LDEF	Long Duration Exposure Facility
MDB	Mesh Double-Bumper
MLI	Multi-Layer Insulation
MMOD	Micro-Meteoroids and Orbital Debris
MS	Multi-Shock
NASA	National Aeronautics and Space Administration
OD	Orbital Debris
SPH	Smoothed-Particle Hydrodynamics

1. INTRODUCTION

The European Space Agency defines orbital debris as all non-functional, man-made objects, including fragments and elements thereof, in Earth's orbit or re-entering Earth's atmosphere [1]. This collection of objects has been a growing concern for many years; ever since the hazard was first acknowledged in the early 1980s it has been the subject of numerous studies by space agencies, and it continuously increases the demands on spacecraft protection systems, thus leading to an increase in the weight, size and cost of spacecraft [2].

In addition, current protection techniques are not capable of protecting spacecraft from the whole range of orbital debris; there is a group of objects, from approximately 1 to 10 cm in diameter to which even well protected spacecraft remain vulnerable. Therefore, the objective of this project is the design of a conceptual space vehicle to act as a shield to other larger and higher-value spacecraft from orbital debris and to explore the feasibility of such a measure for orbital debris protection.

This chapter will go over the evolution of the orbital debris environment up to the present day and will review the measures, some of which are already being taken, that must be applied in order to protect spacecraft from the increasing number of objects in orbit and prevent catastrophic debris population growth in Low Earth Orbit (LEO). Then, the feasibility of implementing or improving these measures will be evaluated, justifying the selection of the measure that was proposed as the project's objective. Finally, the project's objectives will be defined in more detail, taking into account the characteristics of the orbital debris environment, which will be briefly reviewed.

1.1. EVOULUTION OF THE ORBITAL DEBRIS ENVIRONMENT

The first man-made spacecraft to be sent into Earth's orbit was the USSR's Sputnik 1 in 1957; since then there have been over 6800 others with a variety of different purposes and functions. Each space mission affects the space environment by leaving behind debris during launch and operation, and in many cases the spacecraft itself is also left in orbit at the end of its useful lifetime [3]. At present there are over 23 000 pieces of debris larger than 5 to 10 cm in diameter being tracked in orbit, and it is estimated there are over 100 million smaller pieces, tracking of which is not possible [4]. Figure 1-1 shows a representation of the catalogued debris in Earth's orbit in 2008[1].

(a) **(b)**

Figure 1-1. Trackable objects seen from outside geosynchronous Earth orbit (GEO) (a) and LEO (b) in 2008, artist's impression [5], [6].

Orbital debris is generally categorized by size into 3 groups: debris is considered large if it measures 10 cm or more, medium if between 1 and 10 cm, and small if less than 1 cm in diameter [3]. For this project, however, a more useful distinction is that between trackable and non-

[1] There are various different types of orbits around Earth. The three most frequented orbits are LEO, GEO and HEO: Low Earth orbits (LEO) are orbits with an altitude of between 160 and 2000 km; Geosynchronous Earth orbit (GEO) is a circular orbit above the Earth's equator at an altitude of 35786 km; and Highly Elliptical orbits (HEO) are elliptical orbits with a high altitude apogee and a low altitude perigee.

trackable debris. Whether or not an object is trackable does not depend solely on the object's size, but in general only objects over 10 cm in diameter can be considered trackable [7].

For both trackable and non-trackable debris, the main types of orbital debris and their sources are [3]:

- Defunct spacecraft left in orbit after their useful lifetime. Currently there are approximately 2400 non-operational spacecraft still in orbit.
- Debris released during launch. There are approximately 1700 upper rocket stages which remain in orbit.
- Mission-related debris which is released during the spacecraft's operation (e.g. sensor and engine covers, straps and springs, particles of coolant residue, aluminum oxide from solid rocket motor effluents, paint flecks etc.).
- Fragments from both active and inactive spacecraft breakups due to collisions. Such events can generate thousands of pieces of large and many more medium and small debris as happened during the 2007 Chinese FY-1C anti-satellite missile test and as a result of the collision between the Iridium 33 and the Kosmos 2251 spacecraft that occurred in 2009 [8].
- Fragments from explosions, both deliberate (to destroy sensitive information) and accidental (of pressure vessels, fuel tanks, batteries or other sources of stored energy). These can have a similar effect on the orbital debris environment to that of spacecraft breakup.

Overall, every year thousands of large and medium-sized items of debris are created. Figure 1-2 shows the evolution of the debris environment in Low Earth Orbit for objects catalogued by the U.S. Space Surveillance Network. The two evident jumps seen in figure 1-2 for 2007 and 2009 are results of the FY-1C anti-satellite test and the collision between Iridium 33 and Kosmos 2251.

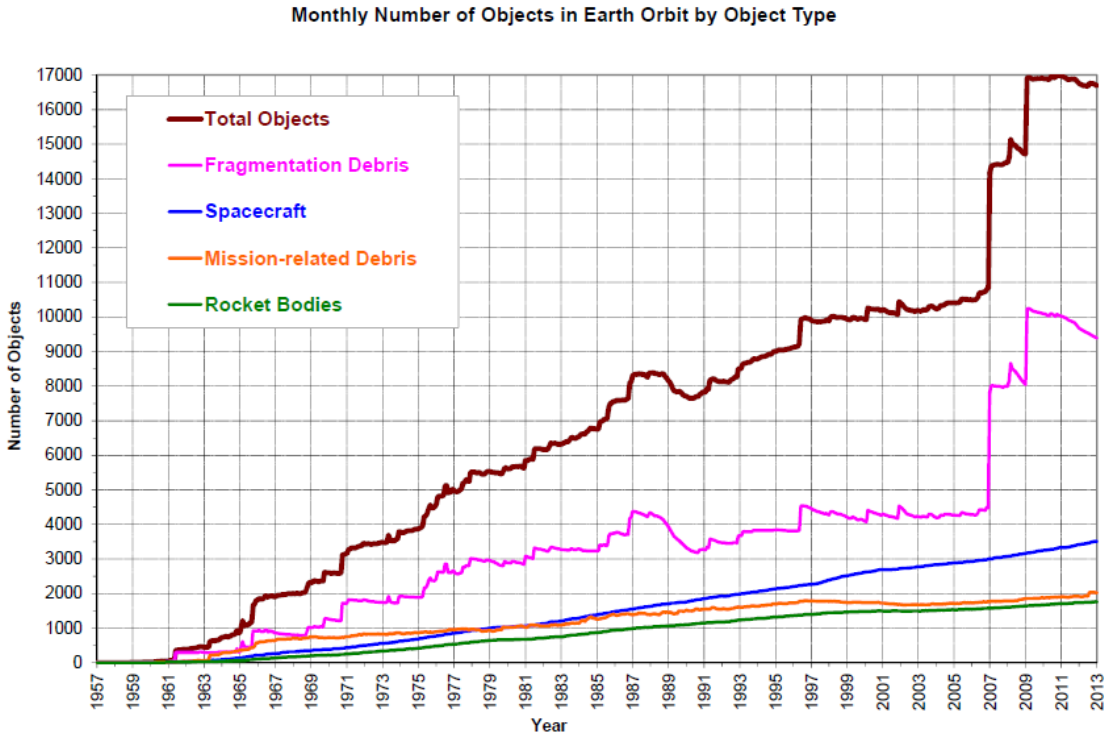

Figure 1-2. Monthly Number of Cataloged Objects in Earth Orbit by Object Type: This chart displays a summary of all objects in Earth orbit officially cataloged by the U.S. Space Surveillance Network. "Fragmentation debris" includes satellite breakup debris and anomalous event debris, while "mission-related debris" includes all objects dispensed, separated, or released as part of the planned mission [9].

In opposition to the overall trend of worsening the orbital debris environment, there are factors that cause orbit degradation, which causes objects to lose altitude and eventually fall out of orbit completely. While this effect is undesirable in the case of spacecraft, it is very positive in the case of orbital debris because it means a shorter orbit lifetime.

There are 3 main factors causing natural orbit degradation [10]:

- Atmospheric drag, which reduces the orbital energy of objects orbiting below altitudes of about 800 km.

- Solar radiation pressure, which has a greater effect on objects with a high surface-to-mass ratio.
- Lunar or solar gravitational perturbations, which primarily affect objects in highly elliptical orbits such as HEO (Highly elliptical orbits) or GTO (Geosynchronous transfer orbits). These perturbation forces mainly affect small debris, and in recent years have on average removed two or three catalogued objects from orbit per day.

There is also an external factor removing debris from orbit. For spacecraft, the rising concern over the orbital debris hazard has resulted in the implementation of EOL (end of life) maneuvers, which consist in using left-over fuel at the end of operation to reduce orbital lifetime, by moving the spacecraft to a lower orbit, or even deorbiting the spacecraft completely.

The problem with the orbital debris environment, however, is that the rate at which new debris is created is far greater than the rate at which items are removed from orbit, so that the orbital debris population will keep increasing over time as has been happening over the past 56 years (figure 1-2), as long as spacecraft continue to be launched into orbit. But the problem does not end there: there is an added risk in LEO, where spatial densities are highest, and that is the risk of collisional cascading, also known as the Kessler effect.

Collisional cascading is a situation where, above a critical debris density, collisions between objects would cause a cascade of further collisions, each in turn generating more debris and consequently increasing the likelihood of further collisions. In this situation, the number of pieces of debris would rise exponentially over time even if spacecraft launches were to stop completely, and eventually space exploration and use of satellites could be rendered unfeasible in affected orbits [11]. This critical density is believed to have been surpassed in the most densely populated altitudes within LEO (above 800 km), although it is uncertain whether collisional cascading has

started to take place. Other orbits, such as HEO or GEO, are not in immediate risk of collisional cascading because of their lower spatial density and lower orbital velocities, both of which mean there is a lower probability of collisions occurring [12].

1.2. ORBITAL DEBRIS MITIGATION AND SPACECRAFT PROTECTION MEASURES

For space activities to continue to be carried out safely in the future, due to the growing population of the orbital debris environment and the risk of collisional cascading, measures will have to be taken in two main areas: orbital debris mitigation, to slow and try to stop the growth of spatial density; and spacecraft protection, to avoid the failure of valuable spacecraft due to the increasing risk of impact in the orbital debris environment.

1.2.1. ORBITAL DEBRIS MITIGATION

If the collisional cascading scenario is to be avoided, space debris mitigation measures must be adopted: figure 1-**Figure 1**-3 illustrates the necessity for such measures as it depicts the number of pieces of space debris in LEO in 2209 predicted by the ESA with and without the implementation of space debris mitigation measures.

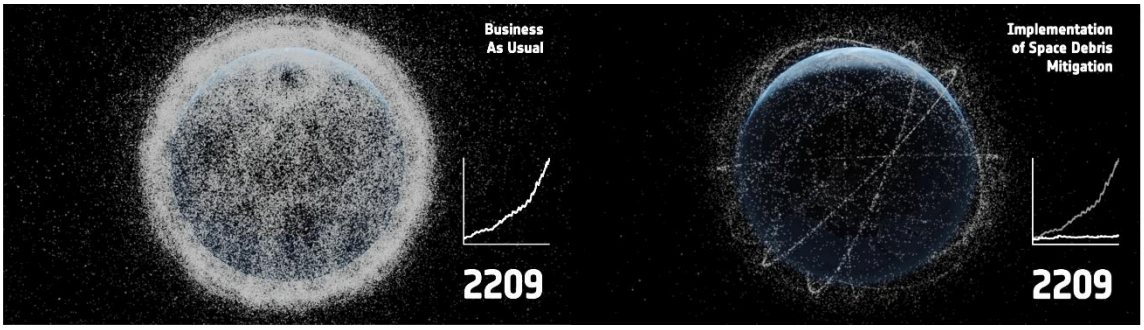

(a) (b)

Figure 1-3. Representation of predicted number of items of space debris in LEO in 2209 with (a) and without (b) implementation of space debris mitigation [13].

These measures can be grouped into 3 main categories:

- **Design improvements:**

This measure consists in reducing the generation of launch and mission-related debris, where possible, as well as improving spacecraft protection to reduce the risk of fragmentation upon impact. For various reasons, reducing the generation of launch and mission-related debris is not a suitable proposal for this project. For one, design improvements will have to be made and evaluated independently for each spacecraft during its design phase, which makes finding a global solution or improvement complicated. Secondly, the implementation of this measure is more of a policy-oriented problem. Lastly, it is already being applied by several national and international organizations of the space faring nations: in 2007, the Inter-Agency Space Debris Coordination Committee (IADC) published the IADC Space Debris Mitigation Guidelines, which tackles the reduction of debris generation and to which all of the IADC member agencies agreed [11]. However, the area of improving spacecraft protection still has room for improvement; this is reviewed in detail in section 1.2.2.

- **EOL maneuvers:**

The use of end of life (EOL) maneuvers, which is also being applied already, consists in minimizing the threat from spacecraft at end of life. Examples are deorbiting, using left-over fuel to remove the spacecraft from orbit completely or at least greatly reduce its orbital lifetime; reorbiting, using left-over fuel to place the spacecraft in an unused orbit; and passivation, releasing any remaining stored energy such as pressure vessels, fuel tanks or batteries, to avoid possible explosions.

Predictions can be made regarding the evolution of the debris population in LEO under different conditions to compare the effectiveness of this type of measure. Figure 1-4 shows the effectiveness of postmission disposal over the next 200 years.

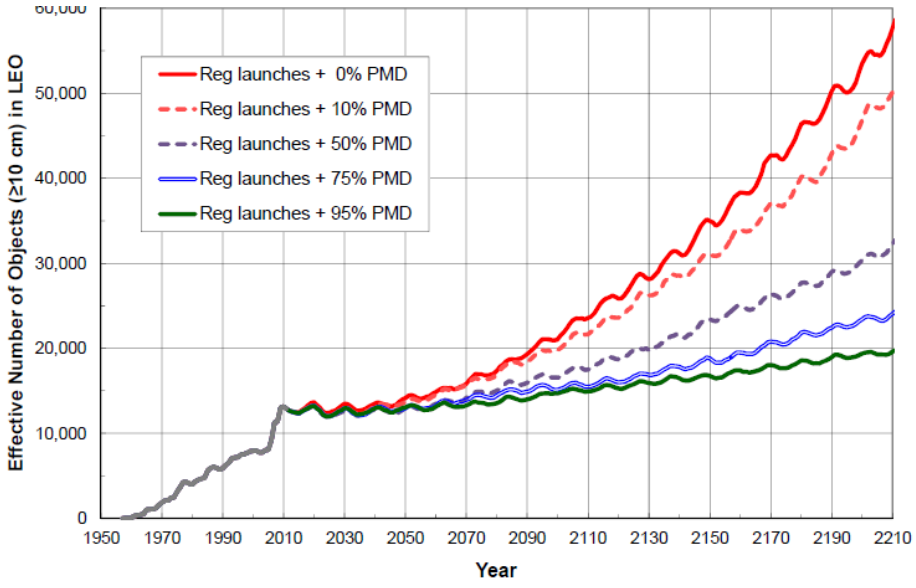

Figure 1-4. Effective numbers for the 10 cm and larger objects in LEO [14].

As can be seen in figure 1-4, postmission disposal is a very effective way of mitigating the growth of the orbital debris population: by removing 95% of spacecraft from orbit at the end of their operational lifetime, the collisional cascading effect can be greatly reduced. However, just like the previous measure it is policy oriented as well as already being enforced, which makes it unsuitable for this project. In addition, this measure alone will not be enough to completely stabilize the object population. A recent study by the IADC concluded that stabilizing the orbital debris population growth requires more aggressive measures, namely the active removal of the more massive non-functional spacecraft and launch stages [12].

- **Active removal:**

This measure consists in removing inactive spacecraft and large pieces of debris from orbit. This would require the design of a spacecraft capable of going into orbit and retrieving non-functional spacecraft and other large pieces of debris. Another approach that has been considered for smaller objects is the use of ground-based medium-powered lasers to perturb the orbit of debris and cause them to lose altitude or avoid a collision [15]. However, active removal of orbital debris is a measure that still has many difficulties to resolve before it can be implemented. The technical issues alone, concerning how debris removal would be carried out, make active removal excessively complex for a project of this magnitude, and there are also many other legal, political and economic issues that will have to be resolved before active debris removal missions can be carried out [16].

1.2.2. SPACECRAFT PROTECTION

Leaving aside orbital debris mitigation measures, even if the growth in spatial density were to be successfully stabilized, current spacecraft protection techniques would still need improvement since there is a range of objects for which no effective means of protection exists. Taking into account that active removal measures are unlikely to be implemented in the immediate future due to the issues they face, the orbital debris population will continue to rise, making improvements in spacecraft protection techniques even more necessary. This is especially true for high-value and crewed missions and spacecraft, such as the ISS.

In order to improve spacecraft protection, the shortcomings of current protection techniques must be evaluated. Current protection techniques can be grouped into three categories: active, passive and operational [17].

- **Active:** techniques that use ground-based sensors to warn of impending impacts and either move the spacecraft to avoid impact or reorient it to protect critical components. Currently, these systems can only guarantee protection from objects larger than 10 cm in diameter, because of the difficulty in tracking smaller objects [7]. Newer technologies, however, allow the tracking of debris in LEO as small as 5 cm, so it is reasonable to assume that over time, active protection techniques will keep improving and guarantee protection from debris of below 10 cm [18].
- **Passive:** techniques that use various forms of shielding to protect spacecraft and components from impacts with smaller debris. Shielding techniques are limited by the admissible size and weight of spacecraft; currently the most effective shields used on spacecraft can only protect them from head-on impacts with debris of up to 10 mm in diameter [19].
- **Operational:** techniques such as oversizing, redundancy and mission and architecture design, which reduce the risk of mission failure due to component damage. These techniques can prevent mission failure due to the failure of individual components, but they increase the cost of the spacecraft.

Current protection techniques cannot defend spacecraft against the entire range of orbital debris sizes: at present there are no effective techniques for objects between 10 mm and 10 cm in diameter. While the probability of impact from objects in this size range is typically so low that it does not significantly affect the likelihood of mission success, there have recently been cases of such impacts, even with small spacecraft, for which the probability is much lower (in 2013 the Ecuadorian nanosatellite Pegaso collided with remains of the Russian rocket S14, and the 85 mm diameter Russian BLITS Satellite was hit by debris from the Chinese anti-satellite missile test FY-1C [20], [21]). This indicates that a probabilistic analysis cannot be relied on completely. For this

reason, and considering the increasing amount of orbital debris, a shielding system to protect spacecraft from objects in this range of sizes could prove increasingly useful and even necessary to certain missions, and would also, in the longer term, help prevent collisional cascading by reducing the likelihood of unforeseen spacecraft fragmentation.

1.3. CONCEPT OF THE "DEFENDER" SPACECRAFT

Two of the previously reviewed measures stand out as the most important, or that would benefit the orbital debris situation the most. These are the active removal of debris and the improvement of spacecraft protection techniques. As was discussed in section 1.2.2., active removal is very complex measure and still faces many obstacles before it can be carried out. Therefore, for this project it seems most feasible to focus on the improvement of spacecraft protection techniques. Active protection techniques are limited by current technologies, whereas passive protection techniques are only limited by the size and weight of the spacecraft. By using an external shield, independent from the spacecraft that is to be protected, the effect of the size and weight restrictions is lessened and a more effective shield can be deployed.

1.3.1. PROPOSAL AND INITIAL OBJECTIVES

The proposed project was motivated by the ideas circulated in the early era of space debris research in 90's [22-26]. The objective of this project was to develop a conceptual design of space vehicle which is able to act as a relatively inexpensive, external form of passive orbital debris protection to other larger and higher-value spacecraft (such as the ISS). It is likely that these types of large spacecraft will become more common in the future, for use as refueling or docking stations or manned space stations, and due to their larger size and long expected lifetimes, they will be more susceptible to impacts from debris.

The proposed “defender” vehicle must consist of a shield to protect these spacecraft from the larger objects in the oncoming flux of orbital debris that cannot be detected with active protection methods. This shield will have to cover a large area to effectively protect the spacecraft it is shielding, and to keep the vehicle inexpensive it should have a mechanism that allows it to be folded and unfolded; in this way the shield can be compactly stored during launch and deployed to cover a large area while in orbit. A representation of the concept is shown in figure 1-5.

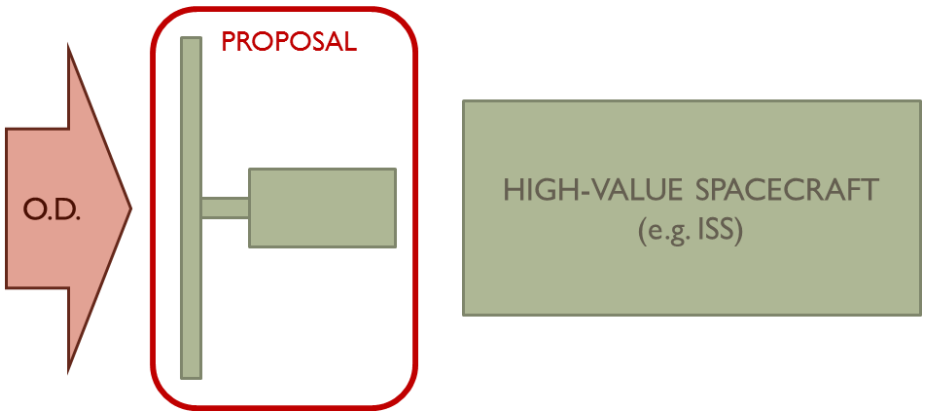

Figure 1-5. Representation of the initial proposal.

The shield must be able to defeat projectiles from the whole range of object sizes, from 1 to 10 cm in diameter, for which current protection techniques are ineffective. However, since the severity of an impact does not solely depend on the projectile’s size (it also depends on other factors such as the relative velocity, impact angle or the densities of both the shield and the projectile), in order to fully define the requirements for the designed shield, the characteristics of the orbital debris environment must be reviewed.

1.3.2. REVIEW OF ORBITAL DEBRIS CHARACTERISTICS

The evolution of the orbital debris environment since the launch of Sputnik 1 in 1957 has led to the present situation, where tens of thousands of items of large and medium-sized orbital

debris pose a high risk to the space infrastructure. The probability of collision of spacecraft with orbital debris and the severity of the consequences of the impact are strongly related to the spatial density of the spacecraft's orbit and orbital debris characteristics, e.g. size, shape and velocity of the debris, all of which are reviewed below.

1.3.2.1. ORBITAL DENSITIES AND VELOCITIES

To give a quick overview of these aspects, the orbital debris situation is described for each of the 3 most trafficked orbits: Low Earth orbit (LEO), highly elliptical orbit (HEO) and Geosynchronous Earth orbit (GEO) [27].

- **LEO:** Low Earth orbits, with an altitude of between 160 and 2000 km, are the most frequently used orbits: this is the altitude range of all manned space stations and the majority of artificial satellites. Low Earth orbits are the most densely populated: figure 1-6 shows the spatial density distribution of catalogued objects in LEO, which have the highest orbital velocities because they are closest to Earth. Velocities in LEO range from 8 km/s at the lowest altitudes to 7 km/s at 2000 km [10]; therefore relative velocities for head-on collisions can reach 15 km/s in the most populated altitudes.

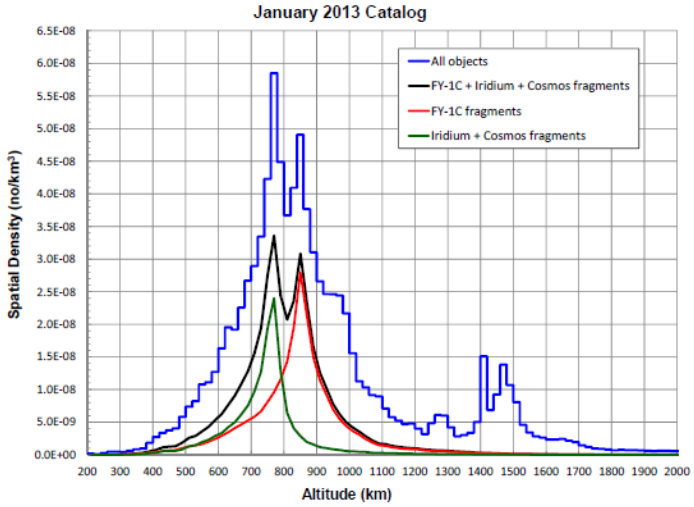

Figure 1-6. Spatial density distribution of the cataloged objects in LEO as of January 2013 [14].

- **GEO:** Geosynchronous Earth orbit is a circular orbit above the Earth's equator at an altitude of 35786 km. Communications and weather satellites often uses this orbit because that it has an orbital period equal to Earth's rotational period, so that they will always appear stationary to a ground observer. Spatial density at this altitude, figure 1-7, is significantly lower than in LEO mainly because of the far greater area that GEO covers. Similarly, due to the high altitude, orbital velocities are also much lower than in LEO: orbital velocity in GEO is about 3 km/s [10].

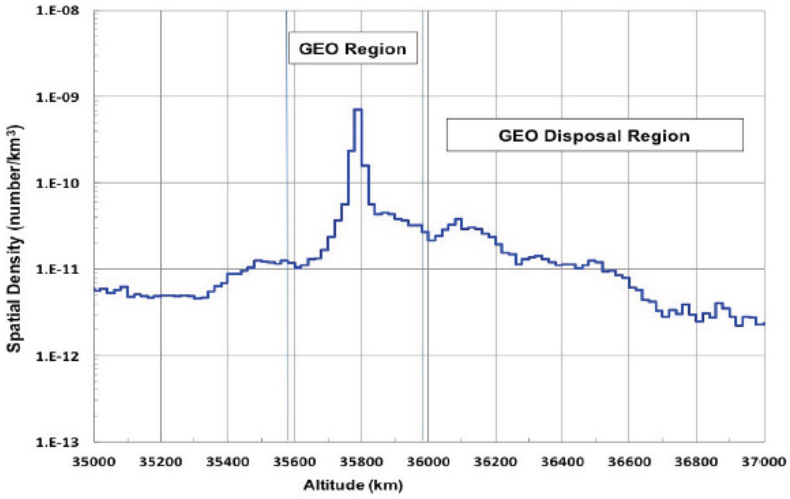

Figure 1-7. GEO spatial densities [28]**.**

- **HEO:** Highly elliptical orbits are elliptical orbits with a high altitude apogee and a low altitude perigee; the most commonly used orbit of this type is the Molniya-type orbit used by the Russian Molniya communication satellites. Due to the nature of these types of orbits, spatial density will vary as a result of changes in altitude, but will mostly be low with short spikes as they cross LEO. As for orbital velocity, in relation to the orbital velocity of the local circular orbit at each altitude, it will be lower at the apogee and higher at the perigee [10].

After this quick overview it can be concluded that LEO is the orbit in the most critical situation, given that spatial densities are over 50 times greater than at any other altitude (as can be seen in figures 1-6 and 1-7) and, at the same time, orbital velocity is more than twice that of the second most densely populated orbit, GEO. Therefore, by designing the shield for LEO, which is the most used orbit and the destination of all manned missions thus far, the shield will also be effective in other higher altitude orbits.

1.3.2.2. OBJECT SHAPES, SIZES AND DENSITIES

The shape of individual pieces of debris cannot be accurately measured using the same technology that is used for tracking. However, since the majority of objects in orbit, especially the larger ones, are fragments from satellites or other spacecraft, experiments can be used to determine the most common fragment shapes that are likely to compose the debris population. To this end, various experiments have been carried out, including the SOCIT 4 destruction of a completed Transit satellite bus, the Kyushiu University fragmentation of six microsatellites, and a rocket body explosion staged by the European Space Operations Center (ESOC) [29].

The analysis of the fragments from these experiments gives an idea of the likely composition of the shapes of the debris population by fragment size [29]:

- The smallest fragments, up to 4 mm, are predominantly “nuggets,” or pitted ellipsoids.
- Intermediately sized fragments, from 4 mm to 2 cm, are most commonly “flakes,” or facets often with one bent or curled edge.
- Larger fragments above 2 cm have a variety of shapes such as cubes, rectangular prisms, cylinders and spheroids. Additionally, objects > 5cm in size can be reasonably assigned to the following shape categories:
    1) Facets, which can include rectangular prisms.

2) Cylinders, both squat and elongated.

3) Spheroids or “globs,” which can be ellipsoidal but tend towards the spheroidical.

4) Needles/wires.

As for object densities, since orbital debris comes from the spacecraft launched into orbit, it can be assumed that most large and medium-sized objects are made of aluminum. With smaller objects there is more variation in materials, which include aluminum, aluminum oxide particles from rocket motor effluents, and flecks of paint [30].

1.3.2.3. IMPACT ANGLES

The final orbital debris characteristic to be reviewed is the impact angle. The angle at which an object impacts a spacecraft can greatly affect the severity of the collision, a representation of the impact probabilities at different angles can be seen in figure 1-8.

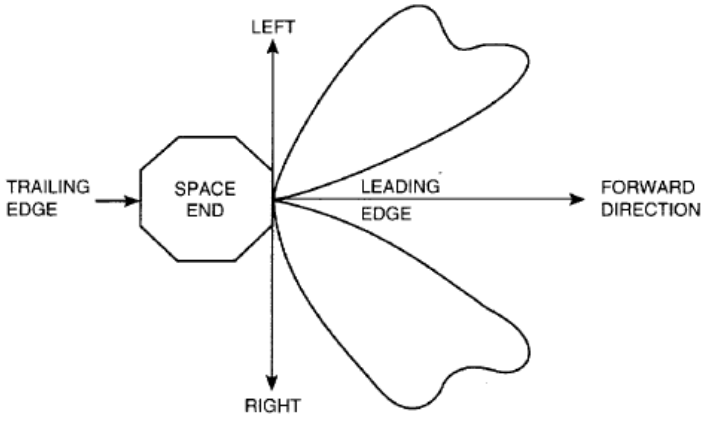

Figure 1-8. Direction of orbital debris impact predicted for the LDEF [10].

Generally, two impact angles are considered in simulations: 0^{o}, which is a head-on impact and represents the greatest danger to the spacecraft, although the probability is low; and 45^{o}, which is the most probable angle of impact.

1.3.3. DETAILED OBJECTIVES

After reviewing the characteristics of the orbital debris environment, the initial objectives can be expanded to include more detailed specifications for the shield:

The objective of this project is to design a light and inexpensive conceptual space vehicle to act as a form of protection to other spacecraft from pieces of orbital debris for which current protection techniques are ineffective. Specifically, the designed space vehicle must be able to protect spacecraft in LEO from impacts with the following projectile characteristics:

- Sizes ranging from 10 mm to 10 cm
- Relative velocities up to 15 km/s
- Impact angles of 0^{o} and 45^{o}
- Density of 2.70 g/cm³ (Aluminum)

Furthermore, the designed vehicle must be able to shield a large area from the flux of orbital debris while also maintaining a compact volume during launch. In order to achieve this, the shield must be able to be folded away during launch and deployed when the vehicle is in orbit.

To reach this objective the problem was split into three main design areas, which define the three design stages for the project. These are:

- Designing a shield configuration capable of protecting spacecraft from higher energy impacts than current shields. Specifically, the shield must be effective against objects up to 10 cm in diameter with relative velocities up to 15 km/s.
- Designing a mechanism to incorporate the previously designed shield into the conceptual space vehicle in such a way that:
  - The shield can be stored as compactly as possible during launch.

  - The shield can be deployed to cover a large area when the vehicle is in orbit.

- Selecting general characteristics of the spacecraft, such as dimensions, components and type of propulsion for launch and for maneuvers once in orbit.

2. SHIELD DESIGN

The first and most important step in the design of the current spacecraft for orbital debris protection was the design of the shielding capable of defeating impactors of up to 10 cm in diameter at relative velocities up to 15 km/s. The design of this shield was carried out in various stages. There was an initial stage of research into existing shield types, covering the principles on which they are based, the materials that are used and the feasibility of using each type for the higher energy impactors that were being considered in this project, while maintaining a low weight and a simple configuration to allow for it to be folded with a simple mechanism to be designed later. The next steps in the design of the shield were the initial design based on the previously researched shield types, followed by an analysis of this design using smoothed-particle hydrodynamics (SPH) simulations. Finally, any necessary modifications and improvements to the initial design were made to reach the final shield design.

2.1. REVIEW OF EXISTING SHIELDING TECHNIQUES

The effectiveness of current on-board shielding is limited by the allowable size and weight of the spacecraft for takeoff, as was mentioned in the introduction, in section 1.2.2. The idea in this project is not to design an entirely new type of shield, but rather to modify parameters such as thickness and standoff distance between layers of an existing shield type, and by removing the size limitation, make it more effective against larger objects. Therefore, before starting the design stage of the shield there is an overview of existing shielding techniques and how they work to show how they can be modified to provide a higher level of protection.

2.1.1. PHYSICS OF HYPERVELOCITY IMPACTS

In LEO collisions occur at very high relative velocities, around 11 km/s on average and up to 15 km/s for head-on impacts. A collision at these velocities can be referred to as a 'hypervelocity impact' (HVI), which is an impact where the relative velocity exceeds the speed of sound in solid material (about 4-5 km/s) [10], [31]. In these conditions shock waves travelling through both the impactor and the shield (figure 2-1) play an important role in the functioning of the shield.

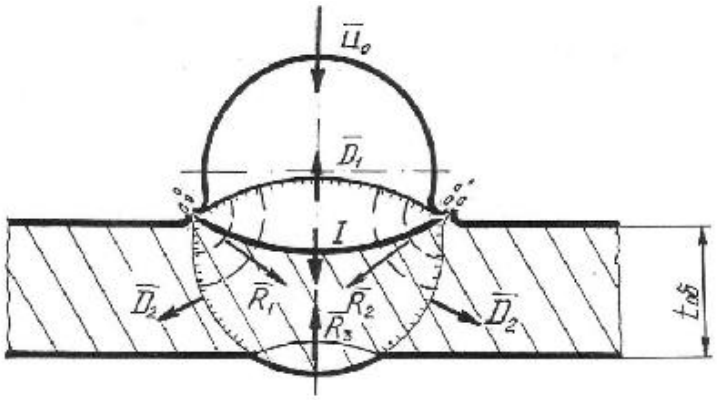

Figure 2-1. Shock waves travelling through a plate and projectile in a HVI [32].

When a collision occurs at such elevated velocities, high compressive shock waves generated at the point of impact move through the projectile and the shield, compressing the materials to high densities [33]. When they reach a free surface, these compressive shock waves are reflected back into the material as tensile, or rarefaction, waves that release the high density and pressure in the material created by the initial compressive shock waves. This sudden release of pressure causes an increase of the internal energy, and therefore of the temperature, in the material. A representation of this process is shown in figure 2-1. At this point there are various possible outcomes. Depending on the relative velocity of the impact, the temperature can reach the melting point and even the vaporization point of the material. At the same time, the result also depends on the thickness of the plate relative to the size of the projectile. If the plate is too

thin, the reflected tensile waves from the shield will overtake the compressive shock waves in the impactor, reducing their intensity and resulting in a lower increase in temperature and the possibility of solid projectile fragments penetrating the plate. However, if the plate is too thick, spalling or internal rupture can occur in the plate in the same way as it does in the projectile; in this case fragments can detach from the rear surface without penetration of the plate (figure 2-2). Figure 2-2 shows an HVI test sample using a thick plate relative to the diameter of the projectile; a spall plane has appeared but no fragments have detached from the rear surface.

Figure 2-2. Hypervelocity Impact on a thick plate, a spall plane can be seen near the bottom surface [34].

This figure (2-2) shows an HVI test sample using a thick plate relative to the diameter of the projectile; a spall plane has appeared but no fragments have detached from the rear surface.

2.1.2. REVIEW OF EXISTING SHIELD TYPES

The most effective types of shield being used for spacecraft protection are based on the Whipple shield, invented by Fred Whipple in the 1940's [35] [36]. This type of MMOD shield consists of 2 separated solid layers, taking advantage of the physics involved in HVI. The first thin layer called the bumper gets perforated by the projectile but breaks it up in the process, generating a small debris cloud made up of fragments of both the bumper and the projectile. There is then a standoff between the first and second layers during which the debris cloud spreads over a larger area, making it easier for the second layer, the rear wall, to withstand the impact. The rear wall must be thick enough that no solid fragments penetrate it. Figure 2-3 shows a representation of the principles behind the Whipple shield in action.

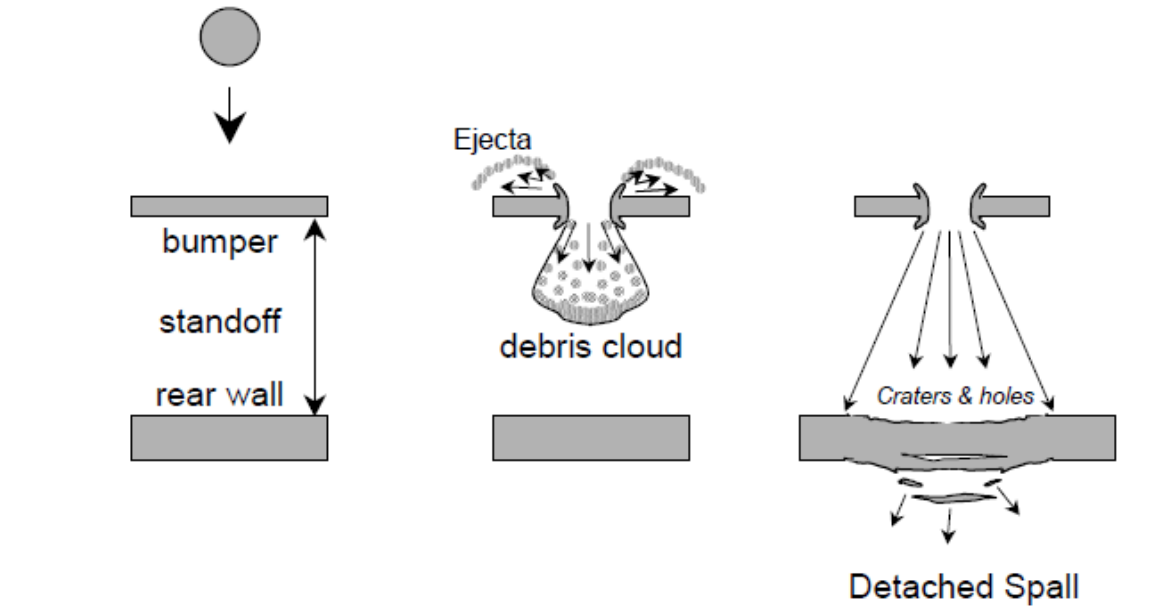

a) Whipple shields consist of a bumper, standoff (gap or spacing), and rear wall.

b) Hypervelocity impacts will generate a cloud of bumper and projectile debris that can contain solid fragments, liquid, and vapor particles.

c) The rear wall must survive the fragments and debris cloud impulsive loading. It could fail by perforation from solid fragments, spall, or tear and petal from the impulsive loading.

Figure 2-3. Representation of a hypervelocity impact on a Whipple Shield [36].

Since the invention of the Whipple shield, many variations have been made on the original design by adding layers of various types and materials. The most commonly used types of MMOD shields that will be reviewed are the Whipple or double wall shield, the stuffed Whipple or triple wall shield, the mesh double-bumper shield and the multi-shock shield, as seen in figure 2-4 [37], [38], [39]. A brief description of each one will be made in the following sections, with a more detailed assessment found in Appendix A that includes a brief description, including advantages and disadvantages; equations for the preliminary design of the shield as a function of the size and velocity of the projectile; and performance equations that define the critical particle size as a function of its velocity for a given shield.

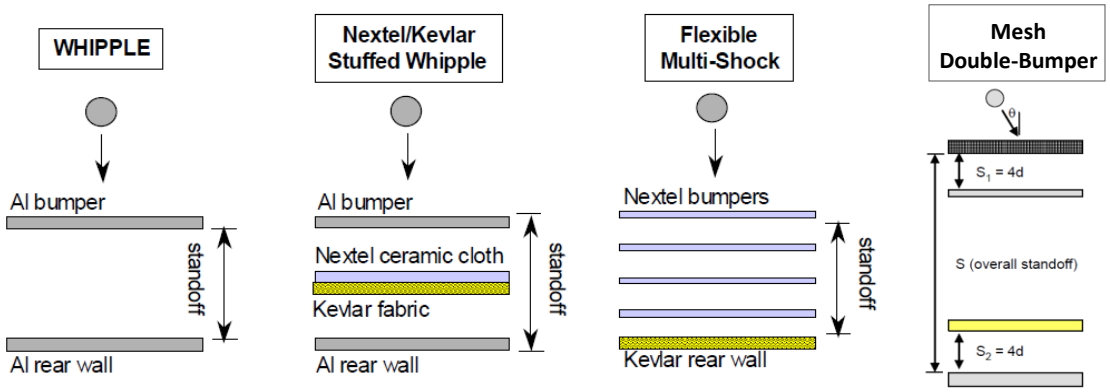

Figure 2-4. Representations of the 4 commonly used types of multi-layer shields [39].

All design and performance equations for each type of shield given in Appendix A have been taken from Dr. E. L. Christiansen's "Handbook for Designing MMOD Protection" [39]; other sources are available but this is the most recent and therefore is backed up by more experimental data [37], [38]. It should be noted that these equations are obtained experimentally from hypervelocity impact testing, and their validity is therefore limited beyond the range of projectile sizes and velocities from which they have been determined. Unfortunately, the size of projectile being tackled in this project falls outside of this range; typically hypervelocity impact tests achieve

impacts at up to 7.5 km/s for up to 22.2 mm diameter projectiles, and therefore data is not available for impacts beyond these sizes [40]. Because of this, these equations cannot be used directly for the shield design in this application; alternatives will be discussed in chapter 3.2, initial shield design.

2.1.2.1. WHIPPLE SHIELD

The original double wall shield, figure 2-5, designed by Fred Whipple in the 1940's consists of a solid aluminum bumper and rear wall. The bumper breaks up the projectile and the rear wall absorbs the impact over a larger surface. The effectiveness of this type of shield depends on the state of the debris cloud formed after the bumper, whether it contains solid, liquid or vaporized pieces of the projectile and bumper [39].

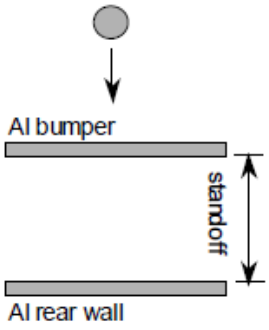

Figure 2-5. Whipple shield schematic [39].

2.1.2.2. KEVLAR/NEXTEL STUFFED WHIPPLE SHIELD

The Kevlar/Nextel stuffed Whipple shield, figure 2-6, more effective than the simple Whipple shield, adds an intermediate layer of advanced materials such as Nextel ceramic cloth reinforced with a layer of high strength fabric such as Kevlar. This intermediate layer slows down the debris cloud and can defeat some of the particles in it, but also reduces the cloud's expansion rate [39].

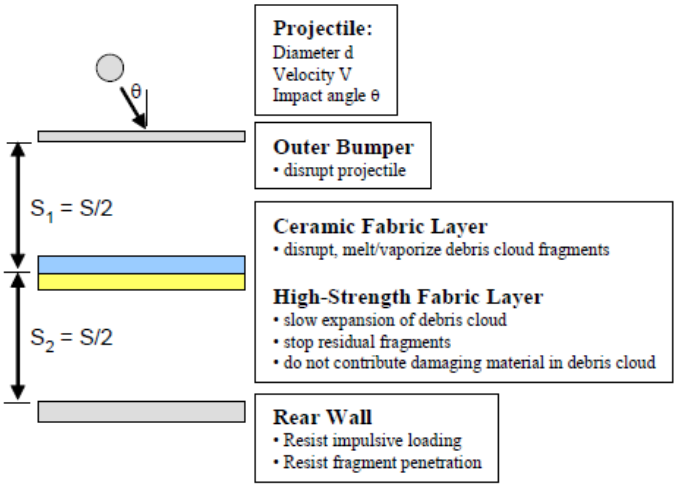

Figure 2-6. Stuffed Whipple shield schematic [39].

2.1.2.3. MESHED DOUBLE-BUMPER SHIELD

The mesh double-bumper (MDB), figure 2-7, shield adds a first aluminum mesh bumper to the concept of the stuffed Whipple shield. The aluminum mesh bumper is more effective at breaking up the projectile by creating multiple shocks; this also produces a wider spread angle of the resulting debris cloud. Another advantage over the solid bumper is that the mesh creates smaller and less damaging bumper fragments [39].

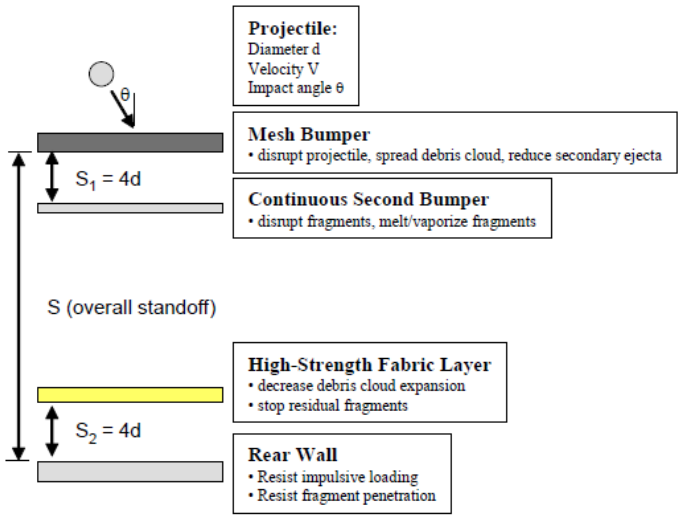

Figure 2-7. Mesh double-bumper shield schematic [39].

2.1.2.4. MULTI-SHOCK SHIELD

The multi-shock shield, figure 2-8, consists of four ceramic cloth layers with either a solid aluminum or a Kevlar rear wall. The four Nextel ceramic layers break up the projectile more effectively than a solid aluminum bumper because they produce higher shock pressures, and for the same level of protection a multi-shock shield will weigh less than a Whipple shield. The ceramic fabric bumpers also have the advantage of producing close to no secondary ejecta, or bumper fragments [39].

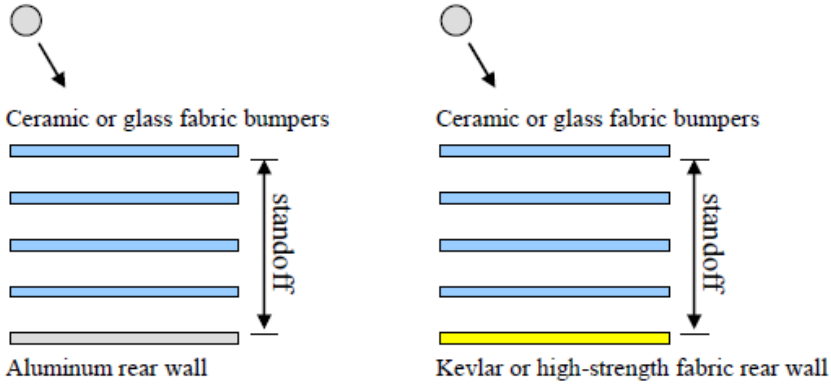

Figure 2-8. Multi-shock shield schematic [39].

2.2. INITIAL SHIELD DESIGN

The shields reviewed so far are typically designed for objects up to 1-2 cm in diameter and, as was previously mentioned, the given shield design equations are not verified for larger projectiles. Not only that, but these equations are given for solid spherical projectiles, which, as was seen in section 1.3.2.2, is unlikely for objects in this range of sizes (1- 10 cm). Because of this, it is not reasonable to use these equations directly for the design of the shield. Instead, two different approaches were considered.

The first approach, inspired by the MDB shield, was to add one or more bumper layers tasked with breaking up the large projectile into smaller fragments that can then be defeated with one of the existing shield models deigned with the given design equations. This way, the shield would consist of two stages, the first stage being the bumpers that break up the projectile and the second stage being the shielding capable of defeating these smaller fragments. An alternative within this approach was to only have the initial bumpers that break up the projectile into fragments small enough for the on-board shielding of the spacecraft that is being protected to defeat; this would reduce the size and weight of the shielding for this conceptual design but would result in significant damage to the shielding of the spacecraft that is being protected.

The second approach was to design a new, simple multi-layer shield through the use of numerical simulations by determining the necessary number of layers of a certain material and thickness that would be necessary to defeat the considered projectile.

In both cases the resulting shield design is would be fairly unoptimized in regard to their overall weight and dimensions. However, the design of a fully optimized shield of these characteristics would be excessively resource-consuming and, therefore, fell outside of the scope of the conceptual design.

2.2.1. TWO-STAGE SHIELD: MS SHIELD WITH ADDITIONAL BUMPERS

The initial design for this approach was limited to selecting the type and dimensions for the second stage of shielding after the projectile has passed through the bumper layers. The design of these bumper layers was done in parallel with the design of the simple multi-layered shield for the second approach with the use of numerical simulations.

For the selection of the second stage of shielding it was assumed that the bumpers could successfully break up the projectile into fragments of up to 3 cm with enough separation between them to be considered separately. Therefore, allowing the reviewed MMOD design equations to be used with a projectile diameter of d = 3 cm and a relative velocity of 15 km/s. The objective in this section was to select a shield configuration that maximized the performance while minimizing the overall mass.

2.2.1.1. SECOND STAGE SHIELDING CHARACTERISTICS AND PERFORMANCES

For every shield model, the design equations were used with different values of standoff (S) and an optimal value was selected that minimized the overall weight, or areal density, of the shield while keeping its dimensions reasonable. With the optimal standoff selected, the theoretical performance of each shield was obtained from the equations and, finally, the different models were compared to determine which one should be used for the final design.

The initial calculations showed that, with a projectile of the given characteristics, the weight reduction was minimal beyond around 100 cm of standoff between layers; this was an acceptable value so it was used as the optimal standoff with which the performance was determined for all four types of shield.

- **Whipple Shield**

Based on the shield design requirements and design equations, table I shows the minimum dimensions that were obtained for each layer as a function of the standoff:

TABLE I. WHIPPLE SHIELD SIZING RESULTS.

S (cm)	t_b (cm)	t_w (cm)	m (g/cm^2)
25	0.75	1.63	6.43
50	0.75	1.15	5.14
75	0.75	0.94	4.57
100	**0.6**	**0.82**	**3.82**

For S = 100 cm, the areal density and the performance across velocities from 0 to 15 km/s are shown in the following figure 2-9. The shield has a 0.6 cm aluminum bumper and a 0.82 cm aluminum rear wall, which result in a total areal density of 3.82 g/cm^2.

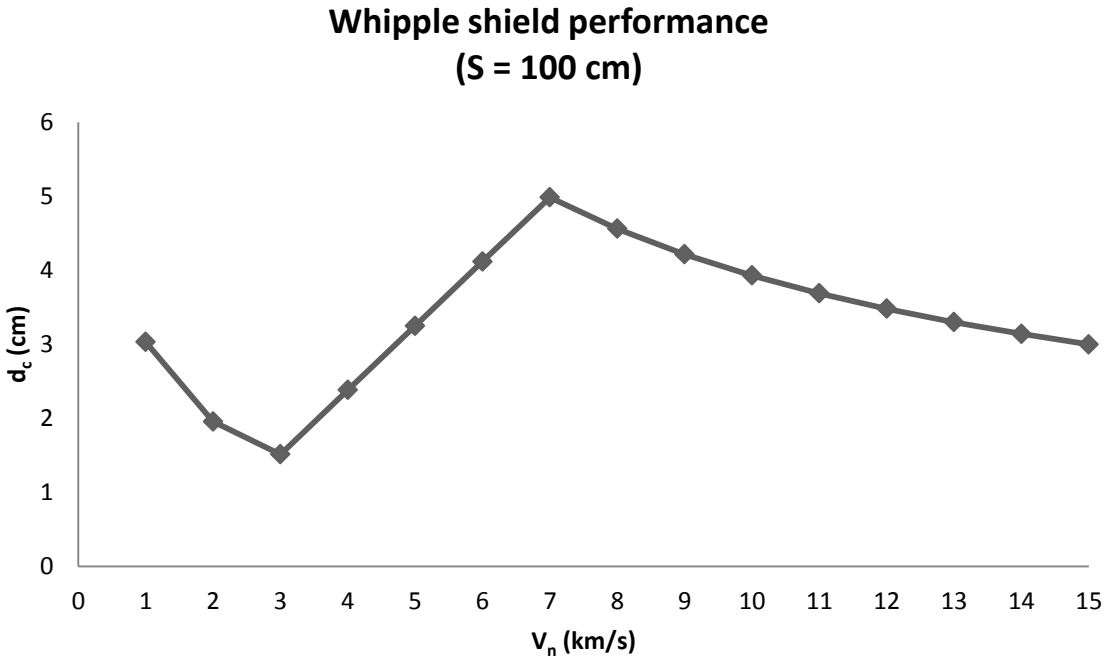

Figure 2-9. Whipple shield performance with S = 100 cm**.**

- **Kevlar/Nextel Stuffed Whipple Shield**

Based on the shield design requirements and design equations, table II shows the minimum dimensions that were obtained for each layer as a function of the standoff:

TABLE II. STUFFED WHIPPLE SHIELD SIZING RESULTS.

S (cm)	t_b (cm)	m_{NK} (g/cm^2)	t_w (cm)	m (g/cm^2)
25	0.45	1.86	0.95	5.64
50	0.45	1.86	0.24	3.72
75	0.45	1.86	0.11	3.36
100	**0.45**	**1.86**	**0.06**	**3.24**

For S = 100 cm, the areal density and the performance across velocities from 0 to 15 km/s are shown in the following figure 2-10. The shield consists of a 0.45 cm aluminum bumper, a 1.86 g/cm^2 Nextel-Kevlar stuffing and a 0.06 cm aluminum rear wall; the overall areal density of the shield is 3.24 g/cm^2.

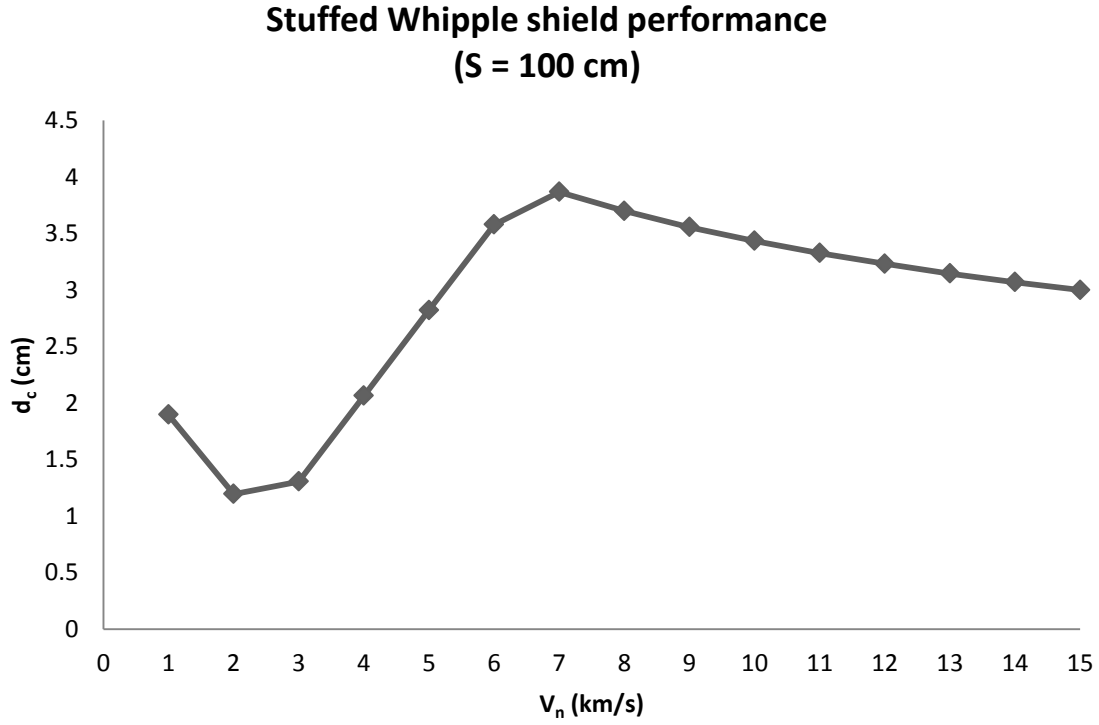

Figure 2-10. Stuffed Whipple shield performance with S = 100 cm.

- **Meshed Double-Bumper Shield**

Based on the shield design requirements and design equations, table III shows the minimum dimensions that were obtained for each layer as a function of the standoff:

TABLE III. MESHED DOUBLE-BUMPER SHIELD SIZING RESULTS.

S (cm)	m_{mesh} (g/cm^2)	$m_{AlBumper}$ (g/cm^2)	m_K (g/cm^2)	m_W (g/cm^2)	m (g/cm^2)
25	0.32	0.75	0.52	13.04	14.63
50	0.32	0.75	0.52	4.61	6.20
75	0.32	0.75	0.52	2.51	4.10
100	**0.32**	**0.75**	**0.52**	**1.63**	**3.23**

For S = 100 cm, the areal density and the performance across velocities from 0 to 15 km/s are shown in the following figure 2-11. In these conditions, the minimum dimensions for the shield's different layers are 0.32 g/cm^2 for the Al mesh, 0.75 g/cm^2 for the Al bumper, 0.52 g/cm^2 for the Kevlar stuffing and 1.63 g/cm^2 Al rear wall; the overall areal density of the shield is 3.23 g/cm^2.

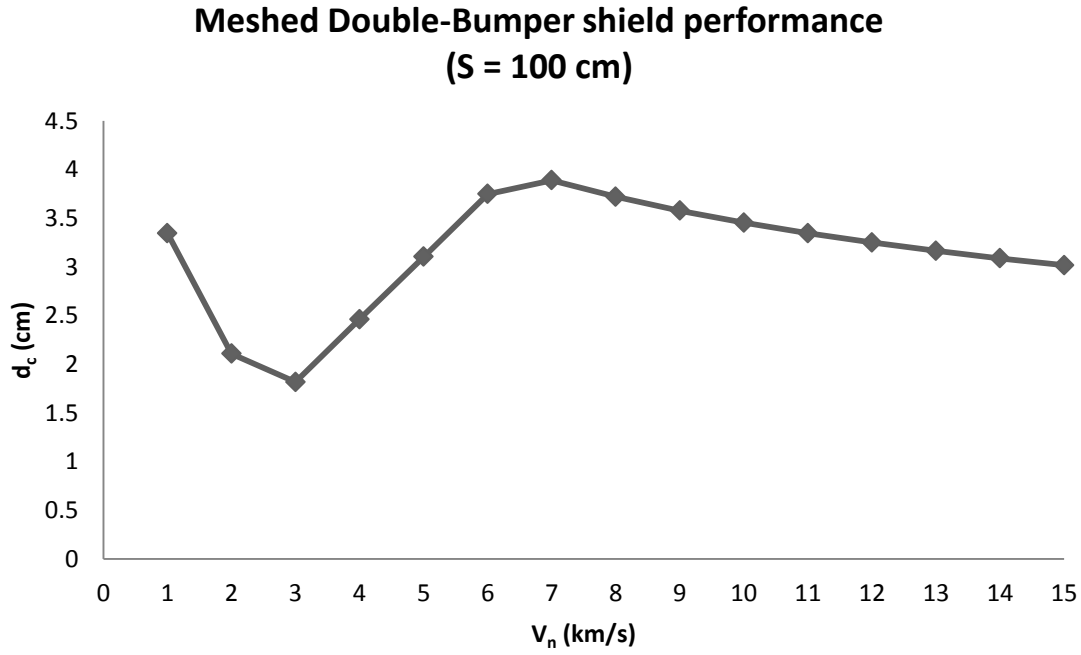

Figure 2-11. Meshed Double-Bumper shield performance with S = 100 cm.

- **Multi-Shock Shield**

Based on the shield design requirements and design equations, table IV shows the minimum dimensions that were obtained for each layer as a function of the standoff:

TABLE IV. MULTI-SHOCK SHIELD SIZING RESULTS.

S (cm)	m_b (g/cm^2)	t_W (cm)	m_W (g/cm^2)	m (g/cm^2) (Al wall)	m (g/cm^2) (Kevlar wall)
25	1.50	4.46	26.57	13.55	28.07
50	1.50	1.12	6.64	4.51	8.14
75	1.50	0.50	2.95	2.84	4.45
100	**1.50**	**0.28**	**1.66**	**2.25**	**3.16**

For S = 100 cm, the areal density and the performance across velocities from 0 to 15 km/s are shown in the following figure 2-12. In this case, the minimum dimensions are 1.50 g/cm^2 for the combined areal density of all 4 Nextel bumpers and either a 0.28 cm Al or a 1.66 g/cm^2 Kevlar rear wall. The shield's total areal densities are 2.25 g/cm^2 and 3.16 g/cm^2 for Al and Kevlar wall, respectively.

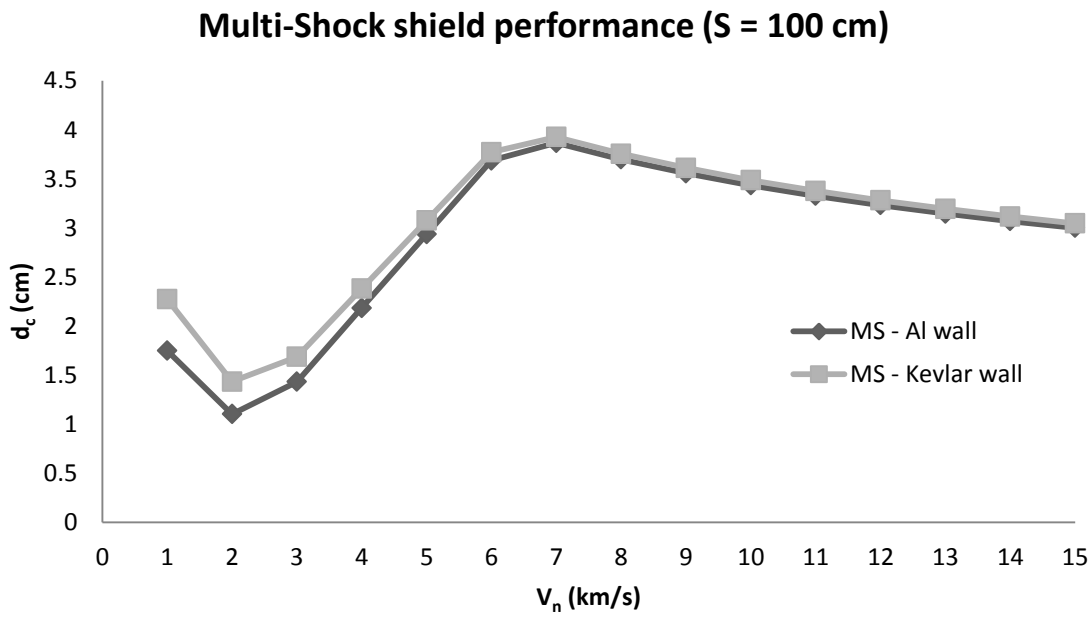

Figure 2-12. Multi-Shock shield performance with S = 100 cm.

2.2.1.2. DISCUSSION AND SELECTION

When comparing the different shield types and their performance, the first thing that stood out was that, in all shield models, performance suffers greatly below the hypervelocity range (V < 6-7 km/s). Going back to the review of the physics of HVI in section 2.1.1, this is explained by the fact that below the hypervelocity range, the projectile no longer breaks up completely, to the point that, in the ballistic range (V < 2-3 km/s), it doesn't break up at all and only suffers plastic deformation. Since all multi-layer shields are based around breaking up the projectile to later absorb the impact energy over a larger surface area, they become ineffective at these lower velocities; to be effective at these velocities, the shields would become prohibitively heavy, similar to the weight of monolithic (single layer) shields, considering the size of the projectile. Currently, there is no real solution to this problem but, since the relative velocity of a collision in orbit depends on the incidence angle, as seen in section 1.3.2, the probability of an impact occurring at these velocities is extremely low. The same situation occurs with the Whipple shields used in the ISS, which were designed for 1 cm Al projectiles but the critical diameter falls to as low as 0.5 cm below the hypervelocity region [41]. Therefore, shield performance was considered acceptable as long as the critical diameter was greater than 10 cm for velocities in the hypervelocity range up to 15 km/s.

Having said this, all considered shield configurations had an acceptable performance and, as was to be expected, the obtained results show that the shields become increasingly efficient as the standoff between layers (S) grows; this can be seen in table V.

TABLE V. SHIELD WEIGHT COMPARISON TABLE.

S (cm)	Whipple m (g/cm^2)	Stuffed m (g/cm^2)	MDB m (g/cm^2)	MS-Al wall m (g/cm^2)	MS-K wall m (g/cm^2)
25	6.43	5.64	14.63	13.55	28.07
50	5.14	3.72	6.20	4.51	8.14
75	4.57	3.36	4.10	2.84	4.45
100	**3.82**	**3.24**	**3.23**	**2.25**	**3.16**

Of the considered configurations, although they all had very similar performance, the aluminum rear wall multi-shock shield with 100 cm of standoff had a significantly lower areal density. Therefore, this was the configuration that was used in the second stage of shielding. Figure 2-13 shows a representation of the initial shield design for this model.

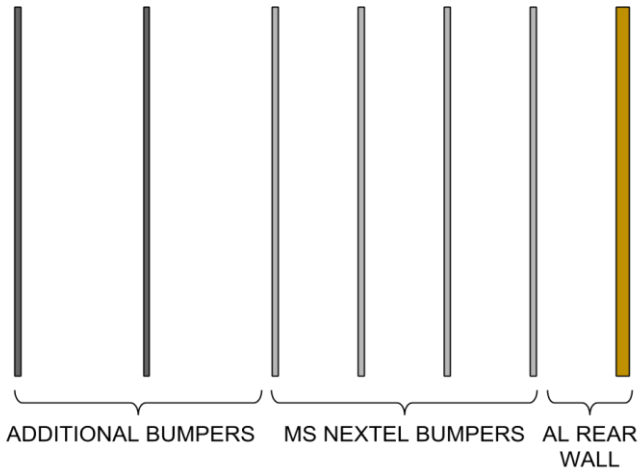

Figure 2-13. Representation of the shield model consisting of a MS shield with additional bumpers.

To finalize the design of this first alternative, the initial bumper layers had to be dimensioned. Since both alternatives used the same bumper layers and these were actually dimensioned during the design of the multi-layer shield alternative, the process is explained in the following chapter.

2.2.2. MULTI-LAYER SHIELD

For this design, an iterative approach was used. An initial estimate of the necessary types, dimensions and standoff between layers was made and this was tested in a numerical simulation. This simulation would determine the number of layers that were required in this configuration; if the number of layers was too great, the initial setup was to be modified and the process repeated until an acceptable shield configuration had been obtained. The objective of this design process was not to find the optimal shield configuration, but to find an acceptable one. Therefore, as soon as a configuration was found that did not have an excessive weight or number of layers, this was selected as the final design of the multi-layer shield approach.

The initial configuration consisted of a combination of aluminum mesh and aluminum plate layers. The aluminum mesh was used for the first few layers because it is more effective at breaking up the projectile than a solid plate of the same areal density, but once the projectile had been successfully broken up the aluminum plates were used to slow down the debris cloud [42]. The initial estimate for the dimensions of the aluminum mesh was made by scaling up the mesh from an existing MDB shield. Dr. E. L. Christiansen's *Handbook for Designing MMOD Protection* describes the mesh used in some of the screening tests using a 0.32 cm diameter aluminum projectile as consisting of 0.3 mm diameter aluminum wires in a square pattern with 30 by 30 wires every 2.5 cm by 2.5 cm [42]. This was scaled up to a mesh with 2 mm diameter wires in a square pattern with a wire every 5 mm, as seen in figure 2-14.

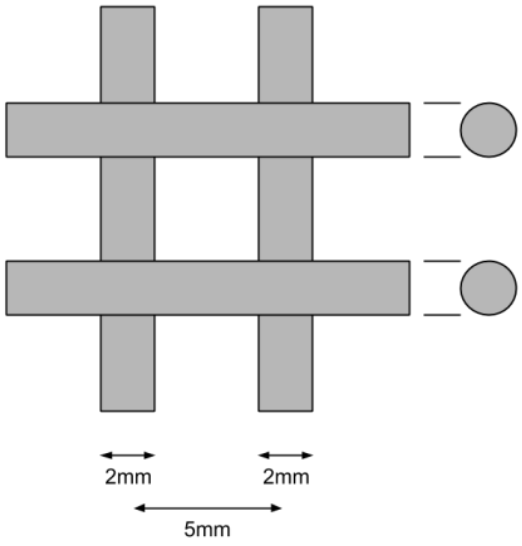

Figure 2-14. Initial dimensions of the mesh used in the bumper layers.

In order to simulate the shield in 2D, since running the simulation in 3D was too time-consuming given the available time and resources for this project, the aluminum mesh had to be modelled as a solid plate. Therefore, the thickness of an aluminum plate that would produce a debris cloud equivalent to that resulting from the aluminum mesh had to be found before the simulation could be executed. To do this, a 3D simulation of the projectile hitting the first layer of mesh was compared to 2D simulations of projectiles hitting aluminum plates with different thicknesses, and the results were compared. Since a simulation of the aluminum mesh bumper had to be done before the full analysis of the shield, the number of mesh layers to be used was selected after the first simulation based on the obtained results.

The thickness of the aluminum plate layers for the first simulation was set at 2 mm to try to keep the shield light in the hope that a greater standoff between layers would result in an acceptable number of layers required to defeat the projectile. With this in mind, the standoff

between each layer was set at 500 mm. Figure 2-15 shows a representation of the initial shield configuration for the first simulation.

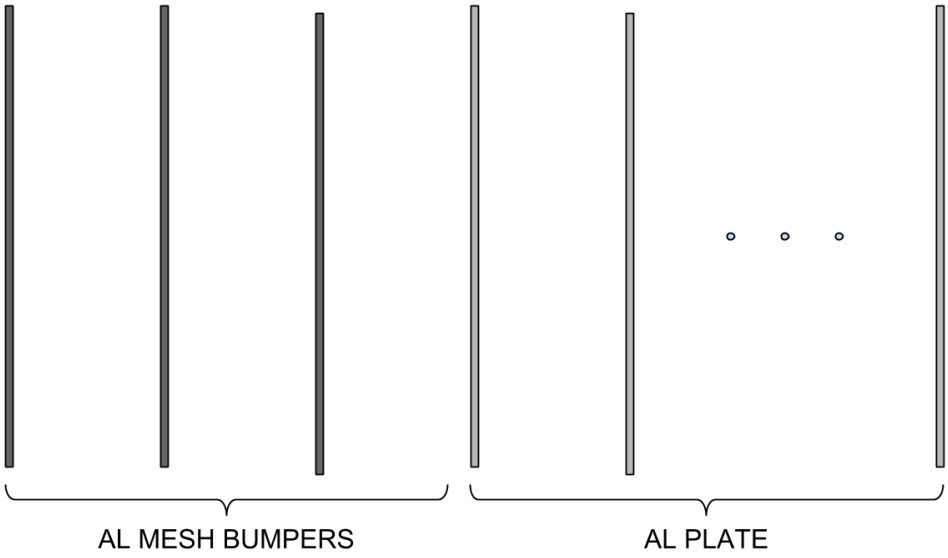

Figure 2-15. Representation of the Multi-layer shield model.

To continue with the design process for both shielding approaches, it was necessary to use numerical simulations. The following chapter explains the method used for these simulations and the results that were obtained.

2.3. NUMERICAL SIMULATIONS

Numerical simulation is a useful alternative to carrying out physical experiments, since these can be dangerous, expensive and time consuming. In this case numerical simulation allowed testing of the different shields under conditions for which physical experiments would not be possible; currently, HVI tests are carried out with projectiles of up to 22.2 mm in diameter at velocities exceeding 7.5 km/s: this falls short of the 10 cm in diameter projectiles for which the initial designs must be tested [40]. Because of this, the testing of the two initial designs was

carried out using numerical simulations. More specifically, the smoothed particle hydrodynamics (SPH) method was used.

2.3.1. RATIONALE FOR USING THE SPH METHOD

Traditionally, grid or mesh-based methods have been used for numerical simulations in many different fields; however, these methods have drawbacks that make them difficult to apply to cases like this one [43]. There are two approaches to grid-based numerical simulations: Lagrangian and Eulerian.

In Lagrangian grid-based methods, the grid is fixed to and describes the material, so that the mesh deforms as the material does [43]. This is useful for computational solid mechanics (CSM) because it focuses on the material, and the entire time history of all field variables can be obtained for any material point, but in problems with large deformations, the mesh becomes heavily distorted. This severely affects the accuracy of the solution and can lead to the breakdown of the computation. A method that has been used to avoid this situation is to re-mesh the material when the mesh becomes excessively distorted, but this is inefficient and time-consuming, and therefore not adequate for ballistic problems, where deformations are extremely large.

The second approach to grid-based simulations is the Eulerian method. In which the grid is fixed in space and the material moves across it [43]. This approach is useful for computational fluid dynamics (CFD) problems but it is difficult to use in solid mechanics when the material has complicated geometries and deformations, because the same fixed cells have to fit the different geometries of the material as it deforms. Another issue with the Eulerian method is that it is difficult to obtain the time history of field variables at fixed material points; instead, this method gives the time history of variables at fixed points in space.

Mesh free methods have become a popular alternative to both Lagrangian and Eulerian grid based methods in problems where conventional FDM and FEM are difficult to apply, such as large deformation analyses in solids, structure buckling problems, incompressible flows and impact and explosion simulations [43]. In this project the smoothed particle hydrodynamics (SPH) method was used. This method was first developed by Gingold and Monaghan in 1977 and is the most widespread particle-based method [44].

2.3.2. SPH REVIEW

The SPH method is a mesh free, particle based Lagrangian method, which means it is material-focused, so it is adequate for solid mechanics problems, and at the same time it offers the advantages of mesh-free methods; due to the adaptability of the SPH method it is not affected by particle distribution and it can therefore tackle problems with extremely large deformations [43]. In the SPH method the studied system is formed by a set of particles that have material properties, and a kernel approximation is used to obtain the spatial derivatives [45]. In this method each particle interacts with all nearby particles within a certain distance and, by weighting these interactions with a smoothing function, the values of a continuous function or its derivatives can be estimated for any individual particle from the values of these functions at the particles surrounding it. Figure 2-16 shows the particles within a distance of 2h of particle I, which are considered its neighboring particles.

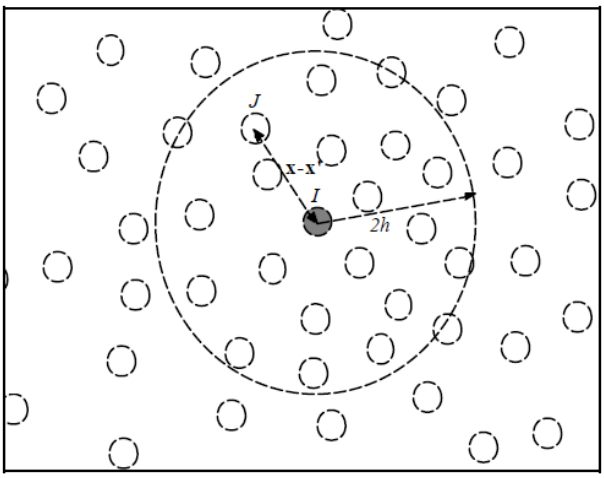

Figure 2-16. Neighboring particles of a kernel estimate [45].

Based on these principles, problems are solved cyclically by applying the following computational cycle [45]:

1. Knowing the initial conditions of the system at the start of the cycle, the particles are sorted so that each particle is associated with its neighboring particles.
2. Once they are sorted a kernel approximation is used to obtain the density and strain rate functions throughout the system.
3. Then, using the conservation of energy and the equations of state, the pressure and internal energy can be obtained, which, in turn, are used to obtain the deviatoric stresses.
4. From applying a second kernel approximation to these deviatoric stresses and including the effect of external forces, the internal particle forces are determined.
5. These obtained particle forces are transformed into particle accelerations, which are then integrated twice to obtain particle velocities and, finally, the new particle positions.
6. With these new particle positions a new computational cycle can be performed.

2.3.2.1. BASIC SPH FORMULATION

There are two fundamental steps in the SPH formulation: The integral representation, or kernel approximation of field functions, and the particle approximation [43], [46].

In the first step, an arbitrary function is multiplied by a smoothing kernel function and then integrated to give the integral representation of the function.

$$f(x) \approx \int f(x')W(x - x', h)dx' \quad [2\text{-}1]$$

$$\nabla \cdot f(x) \approx \int \nabla \cdot f(x')W(x - x', h)dx' \quad [2\text{-}2]$$

Where:

$f(x)$ is a function of the three-dimensional position vector x

dx' is a volume

W is the smoothing kernel function

h is the smoothing length defining the influence area of the smoothing function W

The smoothing function W can be any function, although it is usually an even function, which satisfies 3 conditions:

The first condition is the normalization condition that states

$$\int_{\Omega} W(x - x', h)dx' = 1 \quad [2\text{-}3]$$

The second condition is the Delta function property that is observed when the smoothing length approaches zero

$$\lim_{h \to 0} W(x - x', h) = \delta(x - x') \quad [2\text{-}4]$$

The third condition is the compact condition

$$W(x - x', h) = 0 \; when \; |x - x'| > kh \qquad [2\text{-}5]$$

Where:

k is a constant related to the smoothing function for point at x

In the second step, the continuous integral representations of the function are converted to discretized forms of summation over all the neighboring particles within the domain shown in figure 2-16. This is commonly known as particle approximation.

$$\nabla \cdot f(x_i) \approx \frac{1}{\rho_i} \sum_{j=1}^{N} m_j (f(x_i) - f(x_j)) \cdot \nabla W(x_i - x_j, h) \qquad [2\text{-}6]$$

$$\nabla \cdot f(x_i) \approx -\rho_i \sum_{j=1}^{N} m_j (\frac{f(x_i)}{(\rho_i)^2} - \frac{f(x_j)}{(\rho_j)^2}) \cdot \nabla W(x_i - x_j, h) \qquad [2\text{-}7]$$

Where:

∇W is the gradient with respect to x_j

m is the mass

ρ is the density

To give an example of this method, figure2-17 shows the formula for the calculation of the density at the particle I as a function of the mass of its neighboring particles with the use of a weighting function (W).

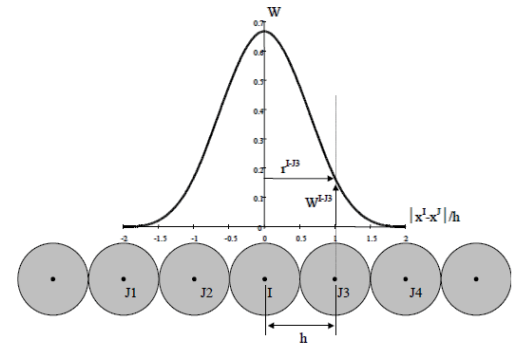

Density Calculation

$$\rho^{I} = \sum_{J=1}^{N} m^{J} W^{IJ}\left(x^{I} - x^{J}, h\right)$$

Figure 2-17. Example Density calculation by interpolation from values of neighboring particles [47].

There are also some numerical problems inherent in the SPH method related to the particle approximation, such as the particle inconsistency and the tensile instability. Some instability problems in mesh-free methods based on weak forms for solid mechanics problems can be avoided if the number of the sampling points for integration is more than the number of particles. For mesh-free methods based on weak forms, stability can also be restored using stabilization terms in the weak form for solid mechanics [48].

To conclude the SPH review, the material properties that were used in the experiments are explained. The Al 7039 alloy used had a Shock equation of state (EOS), a Johnson Cook Strength equation and a Johnson Cook failure model [49]:

- **Shock EOS**: An equation of state is a thermodynamic equation describing the state of matter under a given set of physical conditions.

The shock EOS is a Mie-Gruneisen form that uses the shock Hugoniot, which defines a relation between the variables u_p (particle velocity) and U_s (shock velocity), as a reference curve:

$$U_S = C_1 + S_1 u_p \quad [2\text{-}8]$$

- **Johnson Cook Strength**: The Johnson Cook strength model is a plasticity model that is used to model materials under high strains, strain rates and temperatures. It defines the yield stress, Y, as a function of these three parameters:

$$Y = \left[A + B\varepsilon_p^n\right]\left[1 + Clog\dot{\varepsilon}_p^*\right][1 - T_H^m] \quad [2\text{-}9]$$

Where ε_p is the effective plastic strain, $\dot{\varepsilon}_p^*$ is the normalized effective plastic strain rate and T_H is the homologous temperature.

The plastic flow algorithm used can also reduce high frequency oscillations that can appear under high strain rates, and a specific heat capacity must be defined to calculate the temperature for thermal softening.

- **Johnson Cook Failure**: The Johnson Cook failure is used to model the ductile failure of materials under high pressures, strain rates and temperatures and it consists of three independent terms that define the dynamic fracture strain, ε^f, as a function of these three parameters:

$$\varepsilon^f = \left[D_1 + D_2 e^{D_3\sigma^*}\right][1 + D_4 ln|\dot{\varepsilon}^*|][1 + D_5 T^*] \quad [2\text{-}10]$$

Where σ^* is the pressure, $\dot{\varepsilon}^*$ is the strain rate and T^* is the temperature.

2.3.3. SPH ANALYSIS

The first analysis that was executed was the analysis of the multi-layer shield, starting with the analysis of a single mesh layer to determine the equivalent thickness for a solid aluminum plate. Once a final design was reached, the results were used to select the type and number of bumper layers to be used for the two-stage shielding option, thus avoiding extra unnecessary simulations.

The simulations were executed with the SPH solver in the ANSYS Autodyn 14 explicit dynamics software, using a research license and a Dell Workstation desktop with 2 8-core Xenon E5-2680 CPUs running at 2.7 GHz and 32 Gb of RAM.

2.3.3.1. ANALYSIS SETUP

The simulations were done using the ANSYS Autodyn SPH solver and material models from the included material library with some slight modifications. While in the 3D simulations it was not necessary to set up any type of symmetry, in the case of the 2D analyses the model was set up with 2D planar symmetry and a section cutting through the projectile and the different layers of shielding was modelled. Aside from that, both the 3D and 2D analyses were set up the same way with the same initial conditions, material models and solver controls.

2.3.3.2. GEOMETRY

For these simulations the projectile was modelled as a 60x60 mm^2 aluminum plate with a thickness of 5 mm (figure 2-18).

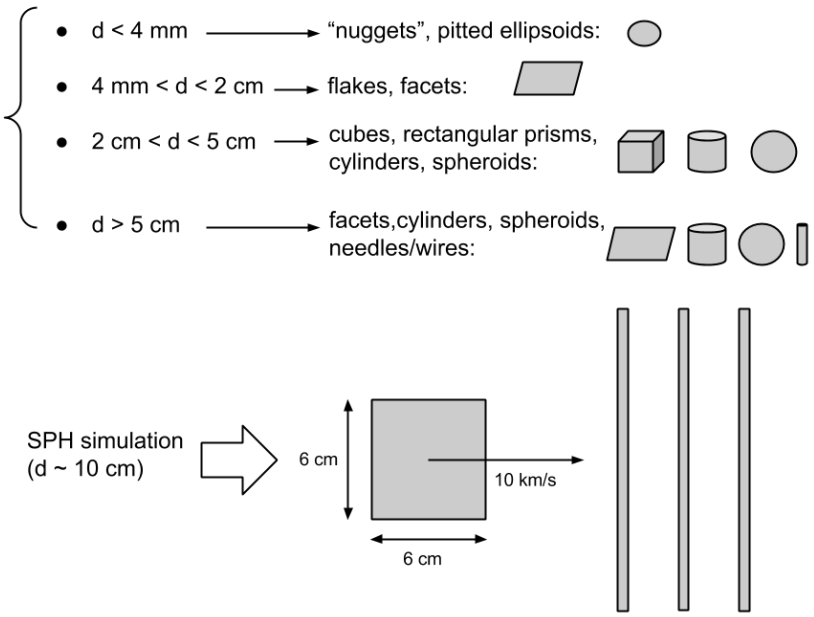

Figure 2-18. Projectile geometry and orientation used in the SPH simulations.

This geometry was selected because it was simple to implement while still being an adequate representation of the debris population in this size range, as was reviewed in 1.3.2.2. The size of the plate (8.5 cm in diagonal) was selected at a point between 5 and 10 cm, taking into consideration the current state of active protection techniques as was reviewed in 1.2.2. The plate was oriented perpendicular to the surface of the layers of shielding, as shown in figure 2-18; to guarantee the shield's effectiveness in the worst case scenario and it was given an initial velocity of 10 km/s.

2.3.3.3. MATERIAL MODEL

Since all the simulations consisted only of aluminum parts, the same material model was used for all for them. The material model used was the high strength AL 7039 aluminum alloy with a Shock equation of state (EOS) and Johnson Cook Strength equation from the available material library, with an added Johnson Cook failure criterion [50]. The properties of the AL 7039 material model that was used are summarized in Table VI.

TABLE VI. AL 7039 MATERIAL MODEL PROPERTIES [49], [50].

Name	AL7039
Reference Density [g/cm^3]	2.000

EOS	Shock
Gruneisen coefficient [-]	2.000
Parameter C1 [m/s]	5.328e3
Parameter S1 [-]	1.338
Reference Temp [K]	300
Specific Heat [J/kgK]	874.999

Strength	Johnson Cook
Shear Modulus [kPa]	2.76e7
Yield Stress [kPa]	5.328e3
Hardening constant [kPa]	3.43e5
Hardening exponent [-]	0.410
Strain Rate Constant [-]	0.010
Thermal softening exp [-]	1
Melting Temperature [K]	877
Ref. Strain Rate [/s]	1

Failure	Johnson Cook
Damage Const, D1 [-]	2.76e7
Damage Const, D2 [-]	5.328e3
Damage Const, D3 [-]	3.43e5
Damage Const, D4 [-]	0.410
Damage Const, D5 [-]	0.010
Melting Temperature [K]	877
Ref. Strain Rate [/s]	1

2.3.3.4. PROBLEM DISCRETIZATION AND INITIAL CONDITIONS

Finally, the last step in the simulations setup was to fill the impacting plate and the different layers of shielding with SPH particles. The projectile was filled with AL 7039 particles with an initial velocity of 10 km/s, while the various layers of shielding were filled with AL 7039 particles with an initial velocity of 0 km/s. For the initial 2D and 3D simulations to find the equivalent thickness to represent the aluminum mesh in the full simulation, the SPH particle size was set at 0.3 mm, larger than the particles used in the full simulation, in order to speed up the process, since this was not the main focus of the analyses. For the full simulation, however, the SPH particle size was reduced to 0.15 mm to improve the accuracy of the results.

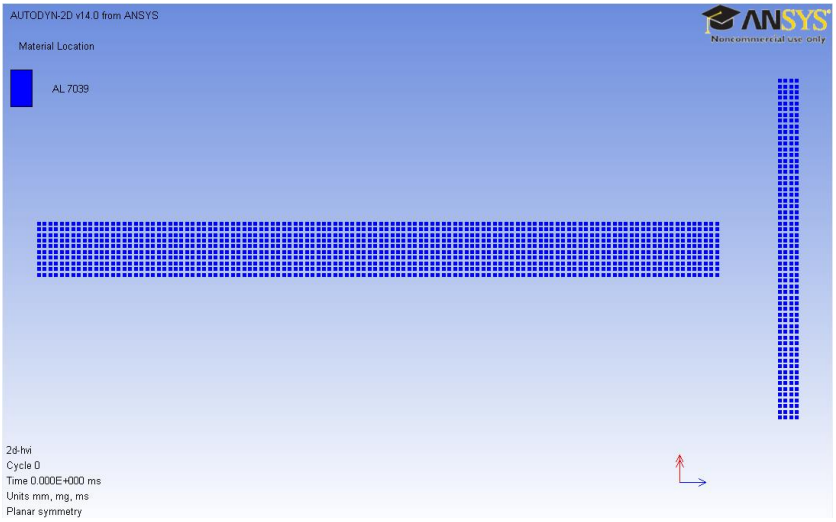

Figure 2-19. Discretized plate and first layer of shielding using 0.3 mm SPH particles.

2.3.3.5. RESULTS AND DISCUSSION

The first shield test that was simulated was the aluminum plate impacting a layer of mesh. This was done in 3D and then a number of 2D simulations with thicknesses for the layer of shielding ranging from 1 to 4 mm were done to compare the results and find the equivalent thickness. Each of the simulations took from 2000 to 3000 computational cycles and around 1 hour to complete.

It was found that the 2 mm aluminum plate produced the closest results to the aluminum mesh, as can be seen in figure 2-20, so this was used for the full simulation to represent the mesh layers. In addition, by looking at the debris cloud produced by the first layer of mesh and the portion of the projectile that remains intact, it was estimated that three layers of mesh would be enough to fully break up the projectile and sufficiently spread out the debris cloud.

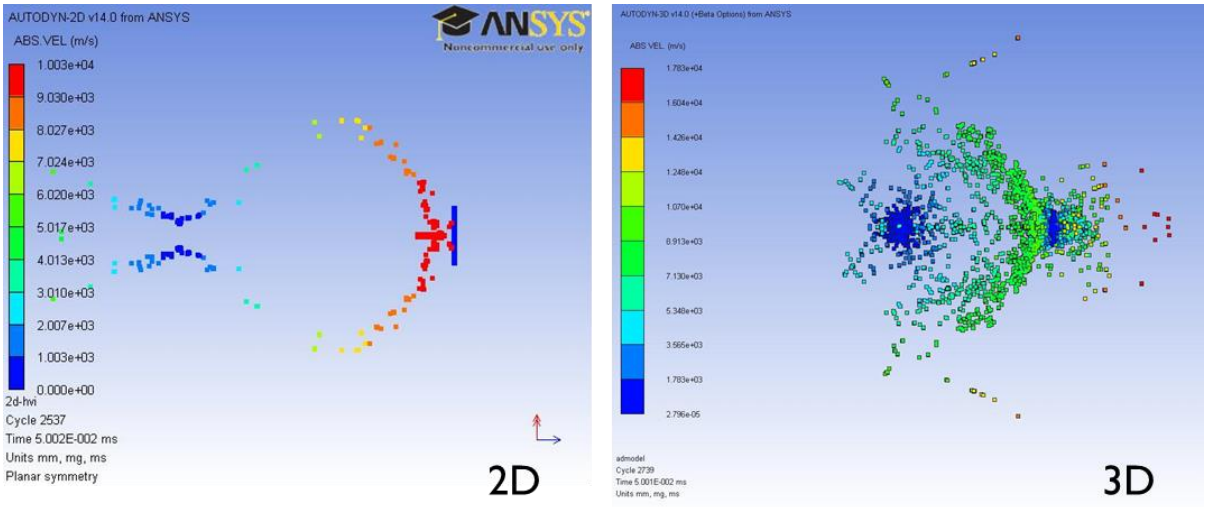

Figure 2-20. SPH simulation results of a 2mm solid plate in 2D (left) and the 3D aluminum mesh (right).

For this reason, in the full simulation the first three layers were made to represent layers of aluminum mesh and all the rest were solid aluminum plates. Coincidentally, both the layers representing the aluminum mesh and the layers of solid aluminum plate were both 2 mm thick.

Ten layers were used in total for the full simulation in the hope that no more than that number would be required. However, if in the simulation the projectile managed to perforate all ten layers, proving that this was not enough, this shield configuration would have to be considered inadequate and the simulation would be redone with thicker layers of shielding rather than have an excessive number of layers. The results from the full simulation are shown in figure 2-21.

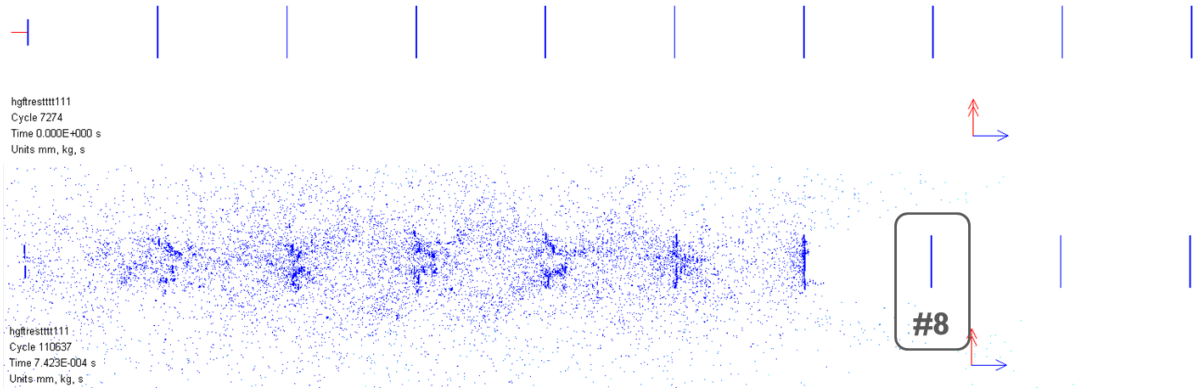

Figure 2-21. Final SPH simulation results.

The final simulation took 110637 cycles to complete and ran for approximately 80 hours. Once it was completed, the results showed that a total of eight layers were needed to fully defeat the 60x60 mm^2 plate. With 500 mm of standoff between layers this resulted in a total distance of 3.5 m from the first to the last layer. Although a lighter and more optimized shield could certainly be designed, this design was acceptable for the purpose of this project taking into account the available resources and, therefore, no further iterations on the design were necessary.

As for the bumpers to be used with the two-stage shield design, since the three mesh layers used in the multi-layer design proved successful at breaking up the projectile, this same configuration was used again.

2.4. FINAL DESIGN SELECTION

At this point there were two viable options for the shield to be used in the conceptual design of the spacecraft, which are summarized in table VII.

The first option, which consisted of two stages of shielding, had an initial bumper made of three layers with a standoff of 500 mm between each layer. These initial layers consisted of 2 mm diameter wire mesh in a square pattern with a wire every 5 mm. After the three layers of bumpers there was a standard multi-shock shield designed for a 3 cm projectile; this had four layers of Nextel ceramic fiber and an aluminum rear wall with a total standoff of 1000 mm. The overall areal density of this design was 3.27 g/cm^2 (three layers of 0.34 g/cm^2 mesh and a MS shield of 2.25 g/cm^2) with a total distance from the first to the last layer of shielding of 2.5 m.

The second option was the multi-layer shield that was tested using SPH. This design consisted of a total of eight layers with a space of 500 mm between every layer. The first three layers consisted of 2 mm diameter wire mesh in a square pattern with a wire every 5 mm, the same as the previous design. After these three layers the next five were solid 2 mm thick aluminum plate. The overall areal density of this design was 3.72 g/cm^2 (three layers of 0.34 g/cm^2 mesh and five layers of 0.54 g/cm^2 plate) with a total distance from the first to the last layer of shielding of 3.5 m.

TABLE VII. FINAL SHIELD DESIGN COMPARISON TABLE.

Properties	A) Two-stage shield	B) Multi-Layer shield
Areal density [g/cm^2]	3.27	3.72
Number of layers	7	8
Total standoff [m]	2.5	3.5

As can be seen in table VII, both shield designs had similar weights and dimensions, with the multi-layer concept being slightly heavier and longer. The multi-layer concept, however, had the advantage of having equally spaced layers throughout the whole shield, which could possibly simplify the deployment mechanism, and the advantage of having been fully tested in the SPH analysis. Ultimately, although both models had their advantages and disadvantages, the multi-layer design was selected because it had been more thoroughly tested. The selected final design is shown in figure 2-22.

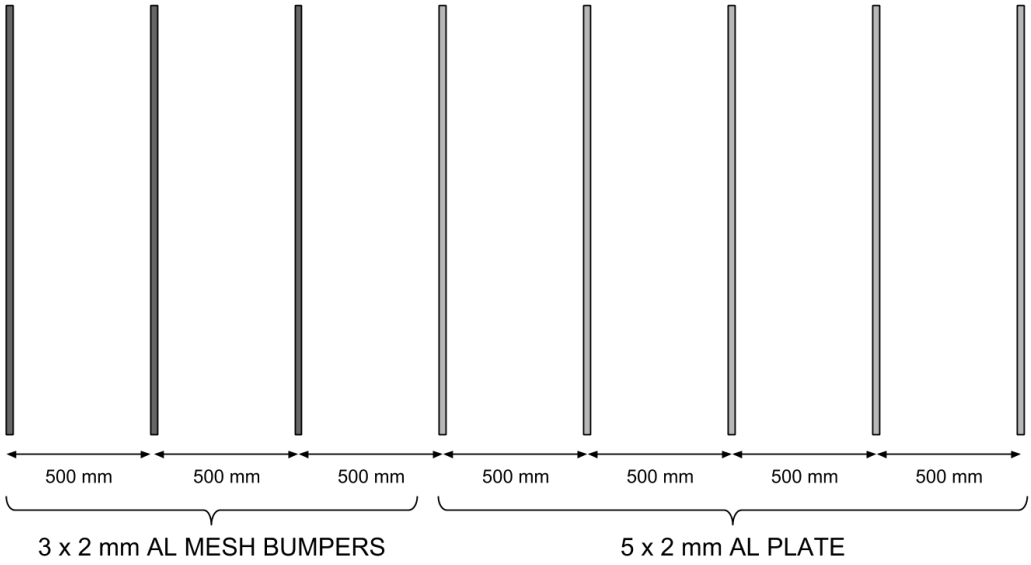

Figure 2-22. Final shield design dimensions.

Finally, it should be noted that, as has been mentioned, neither of the compared designs was optimized to minimize its weight, and if the design of this conceptual vehicle for OD protection were to be explored further, a lighter and more effective shield design could be made by considering other possible configurations and materials. For this reason, the design of the deployment mechanism in the next chapter bears in mind the possibility of accommodating different shield models.

3. SHIELD DEPLOYMENT MECHANISM DESIGN

For the design of the shield deployment mechanism three steps were followed: the first step was to investigate existing mechanisms with similar functions that could be adapted to this purpose; various mechanisms were found that fitted the requirements for this application, so the second step was to compare these mechanisms and selecting the most suitable; finally, the selected mechanism was modified for the specific needs of this project and a kinematic and dynamic analysis was made.

Before any of this could be done, however, it was necessary to define the requirements for the mechanism that was being designed; these are covered in the following chapter.

3.1. DESIGN REQUIREMENTS

There were two main requirements for the deployment mechanism:

- The deployed shield must cover a large area in order to protect a spacecraft behind it; therefore, the shield should be at least 10 m in diameter.
- The folded shield must be as compact as possible to facilitate its launch and placement into orbit; the dimensions of the payload bay from the now retired space shuttle orbiters (4.6 x 18 m) was used as a reference for reasonable dimensions of the whole spacecraft when the shield is folded [51].

As well as these two main requirements for the mechanism, there were also a few secondary requirements that, while not absolutely necessary, would help set apart the various initial design concepts:

- The mechanism would benefit from a simple design that would keep it light and easy to repair and maintain, if necessary.

- While at this point the mechanism is being designed for a shield composed of rigid (aluminum plate) layers, future optimizations of the shield could lead it to use flexible materials such as Nextel or Kevlar fabrics. Therefore, it would be useful for the mechanism to be compatible with both rigid and flexible layers.
- Finally, the mechanism should allow the possibility of covering areas of different shapes and sizes; in this way, shields could be designed specifically for the protection of different spacecraft.

3.2. INITIAL DESIGN

With these considerations in mind, a small number of existing mechanisms were found that could fit the defined requirements:

- **Umbrella mechanism**: This mechanism, shown in figure 3-1, is usually used with a flexible material, although it can also be used with rigid materials (e.g. paper umbrella).

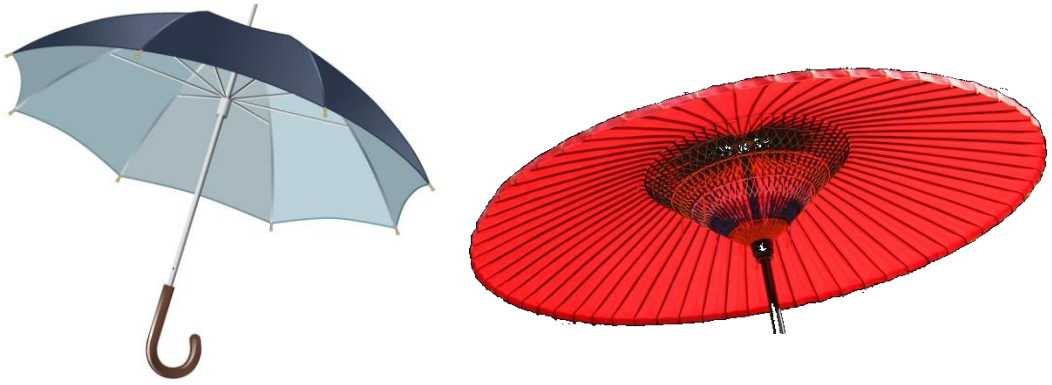

Figure 3-1. Foldable umbrella (left) and paper umbrella (right) [52], [53].

- **Hand fan**: This mechanism, shown in figure 3-2, is intended for rigid plates, although it can be used with fabrics if they are set on a frame.

Figure 3-2. Hand fan [54].

- **Outward sliding plates**: The same basic concept of plates sliding out from under one another used in the previous mechanism can be used with plates sliding outwards from the center instead so that the shield folds into a more compact circular form. A sketch of this idea is shown in figure 3-3.

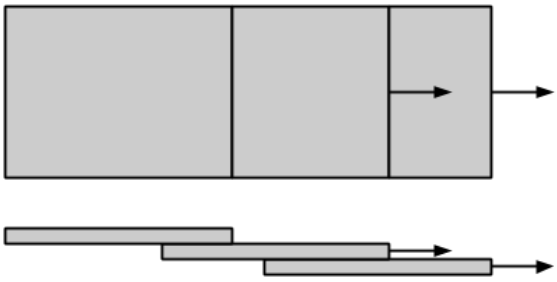

Figure 3-3. Outward sliding plates.

- **Ship in a bottle/cables**: The last option that was considered, shown in figure 3-4, was a simple mechanism using cables to pull and unfold the plates of shielding; in the same way as the masts and sails are unfolded from a ship in a bottle by pulling the strings attached to them once the ship is inside the bottle.

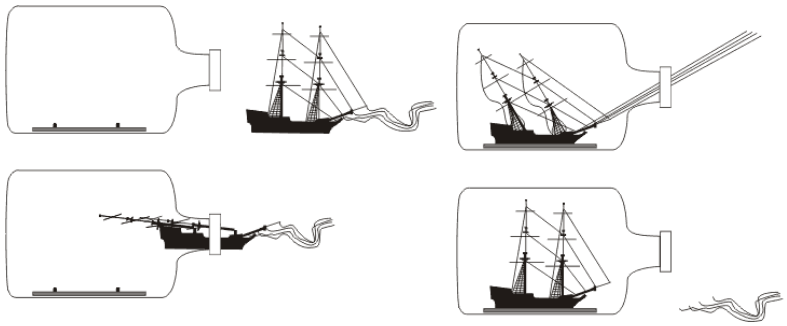

Figure 3-4. Ship in a bottle diagram [55].

3.2.1. COMPARISON AND SELECTION

Of the various possibilities that were considered, the foldable umbrella mechanism was selected for being the most versatile as well as being very compact. Because of its versatility, it fulfilled all of the established requirements: It is a simple mechanism that can easily be adapted to slightly different shapes (e.g. circular, square or rectangular depending on the number and length of branches in the umbrella) and sizes, an example is shown in figure 3-5; and the same type of mechanism can be used with flexible fabric-type materials as well as more rigid materials (e.g. paper umbrella).

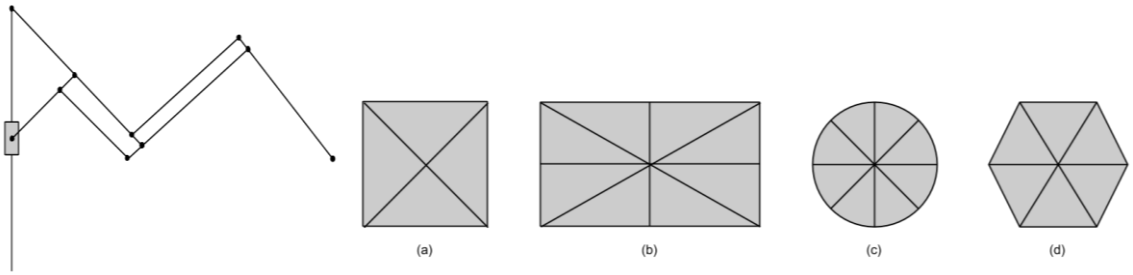

Figure 3-5. Single branch of a foldable umbrella mechanism next to different possible shapes made with different number and lengths of branches: square (a), rectangle (b), circle (c) and hexagon (d).

3.3. FINAL DESIGN

Having selected the foldable umbrella mechanism as a basis for the final design, some slight modifications were made to it to adapt it to the specific requirements of this project: An extra link was added to the end of the mechanism shown in figure 3-5 to extend its reach, the whole mechanism was scaled up to fit a 12 m diameter shield and the shield was made octagonal with 8 branches, one every 45^{o}, supporting each layer.

In this way, the study of the whole mechanism was simplified to the study of a single branch of the mechanism supporting 1/8 of the shield, as seen in figure 3-6. At the same time, since in this mechanism every additional layer of shielding followed the same motion as the bottom layer, it was sufficient to analyze only this first layer in the kinematic and dynamic analysis.

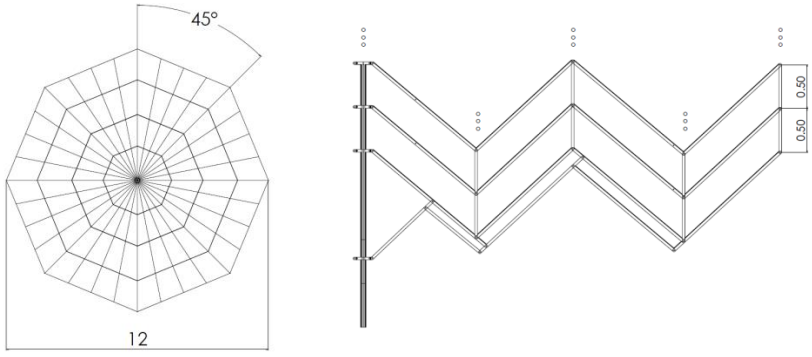

Figure 3-6. Shield deployment mechanism final design, dimensions in m.

Finally, a kinematic and dynamic analysis of the mechanism was made to determine its motion and the resulting forces acting on it as a function of the motion of the slider. This allowed the input motion to be defined in such a way as to minimize the accelerations and, therefore, the inertial forces acting on the mechanism. This analysis was carried out using the method described in the next chapter for the simplified mechanism shown in figure 3-7, below.

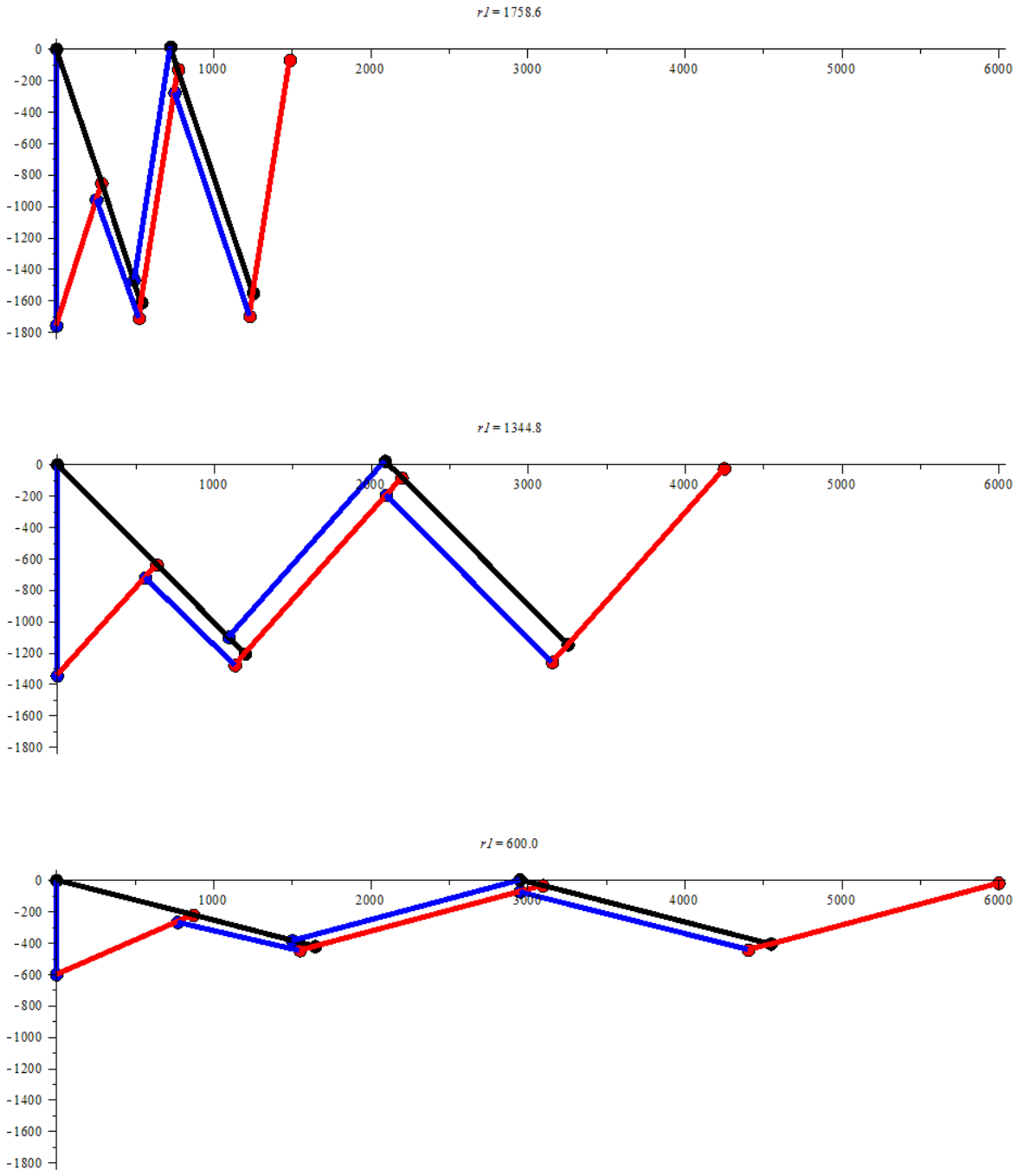

Figure 3-7. Representation of the final deployment mechanism in three different positions.

3.3.1. REVIEW OF KINEMATIC AND KINETIC ANALYSIS METHOD

The method used for the kinematic and kinetic analyses was derived from O. Vinogradov's *Kinematics and Dynamics of Machines and Mechanisms* and will be briefly reviewed in this chapter [56].

The kinematic analysis consists in determining the motion of the mechanism as a whole and each of its elements as a function of the input motion, which in this case, is the motion of the slider (R1). Assuming the position, velocity and acceleration of the input are known, these can then be found for the rest of the elements in the mechanism. The procedure adopted for the kinematic analysis is as follows:

- Skeletal representation of the mechanism
- Determination of the mechanism's mobility
- Selection of a coordinate system
- Identification and numeration of all links
- Identification of all angles characterizing link positions
- Determination of the loop-closure equation
- Identification of input and output variables
- Solution of the loop-closure equation
- Validation of the results by numerical analysis

The skeletal representation is a representation of the mechanism by a system of connected links which completely describes the kinematics of the mechanism and, therefore, allows the trajectory, velocity and acceleration of any point on the mechanism to be found. Figure 3-8 shows a schematic diagram of an internal combustion engine next to its skeletal and vector representations.

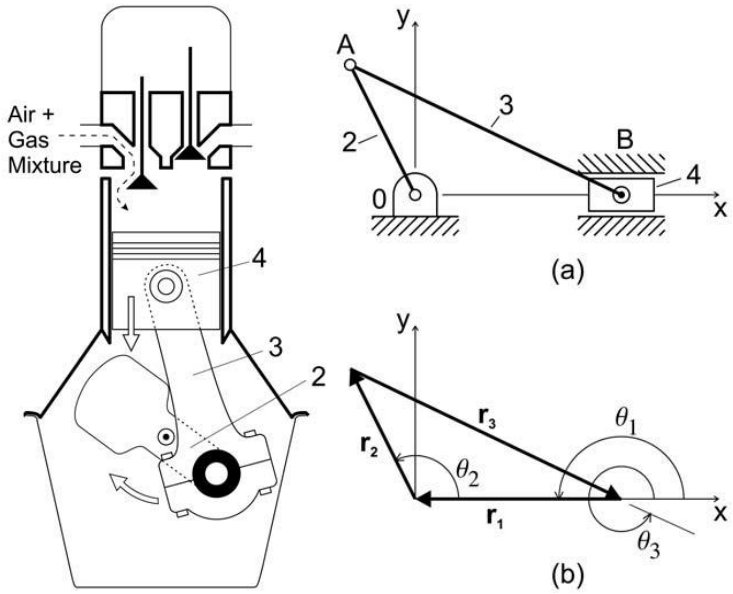

Figure 3-8. Schematic diagram of an internal combustion engine (left), and its skeletal (a) and vector (b) representations (right) [57] [58].

- **POSITION ANALYSIS**

Any simple planar mechanism can be described by a loop-closure equation: for compound mechanisms the mechanism is divided into a number of simple mechanisms which are solved independently. The loop-closure equation for a simple mechanism with N links has the following form:

$$\sum_{i=1}^{N} r_i(\cos\theta_i, \sin\theta_i)^T = 0 \qquad [3\text{-}1]$$

Various cases are possible, depending on the unknown variables in the loop-closure equation: for each of these cases a generic solution can be found. In the mechanism being studied for this project all simple loops into which the whole mechanism is decomposed belong to the same case, two unknown angles; therefore only the solution for this case will be derived in this review.

In this case there two unknown angles, θ_i and θ_j, which are transformed into two new variables, $\alpha - \theta_i$ and $\alpha - \theta_j$, by using the unit vector $u_b = (\cos\alpha, \sin\alpha)^T$. The general loop-closure equation is multiplied by the unit vector perpendicular to vector **b**, and then by a unit vector parallel to vector **b**, resulting in the following two equations:

$$r_i \sin(\alpha - \theta_i) + r_j \sin(\alpha - \theta_j) = 0 \quad [3\text{-}2]$$

$$r_i \cos(\alpha - \theta_i) + r_j \cos(\alpha - \theta_j) = b \quad [3\text{-}3]$$

Where **b** is the vector equal to the sum of all known vectors:

$$\mathbf{b} = (b_x, b_y)^T = -\sum_{i=1, i\neq j}^{N} r_i (cos\theta_i, sin\theta_i)^T \quad [3\text{-}4]$$

$$b_x = -\sum_{i=1, i\neq j}^{N} r_i cos\theta_i \quad [3\text{-}5]$$

$$b_y = -\sum_{i=1, i\neq j}^{N} r_i sin\theta_i \quad [3\text{-}6]$$

Therefore b, $\cos\alpha$ and $\sin\alpha$ are equal to:

$$b = |\mathbf{b}| = \sqrt{{b_x}^2 + {b_y}^2} > 0 \quad [3\text{-}7]$$

$$\cos\alpha = \frac{b_x}{b} \quad [3\text{-}8]$$

$$\sin\alpha = \frac{b_y}{b} \quad [3\text{-}9]$$

There are still two unknowns in the obtained equations, $\alpha - \theta_i$ and $\alpha - \theta_j$, however, now this system is solvable. $\sin(\alpha - \theta_i)$ can be found directly from the first equation and the second equation can be reduced to the following by using the trigonometric identity $\sin^2(\alpha - \theta_i) + \cos^2(\alpha - \theta_i) = 1$:

$$\cos(\alpha - \theta_j) = A = \frac{b^2 - {r_i}^2 + {r_j}^2}{2\, b\, r_j} \quad [3\text{-}10]$$

In the same way the variable $\alpha - \theta_i$ can also be found. The result for $\cos(\alpha - \theta_i)$ and $\sin(\alpha - \theta_i)$ is:

$$\cos(\alpha - \theta_i) = B = \frac{b - r_j A}{r_i} \quad [3\text{-}11]$$

$$\sin(\alpha - \theta_i) = C = \pm\frac{r_j}{r_i}\sqrt{1 - A^2} \quad [3\text{-}12]$$

At the same time, for any found θ_i, the angle θ_j can also be found solely from the loop-closure equations:

$$\cos(\alpha - \theta_j) = (b - r_i \cos(\alpha - \theta_i)/r_j \quad [3\text{-}13]$$

$$\sin(\alpha - \theta_j) = -r_i \sin(\alpha - \theta_i)/r_j \quad [3\text{-}14]$$

In the above equations C has two possible solutions, one positive and one negative one, and for each of the two a separate set of solution angles (θ_i, θ_j) can be found. Both sets are physically admissible since they are based on the solution of the loop-closure equation, which means that the mechanism allows two possible configurations. Therefore, the right value for C will have to be chosen in order to represent the mechanism in the right configuration.

- **VELOCITY ANALYSIS**

Once the position analysis has been done, the velocities of every link can also be determined by using the time derivative of each vector.

For a vector whose magnitude and direction are functions of time, its time derivative represents the velocity vector:

$$\mathbf{r}(t) = r(t)[cos\theta(t), sin\theta(t)]^T \quad [3\text{-}15]$$

$$\frac{d\mathbf{r}}{dt} = \dot{\mathbf{r}} = \dot{r}(t)[cos\theta(t), sin\theta(t)]^T + r(t)[-sin\theta(t), cos\theta(t)]^T\dot{\theta}(t) \quad [3\text{-}16]$$

The velocity vector has two components, the translational velocity and the rotational velocity. The first has the same direction as the original vector **r**(t) and its magnitude represents the rate of change of the vector length.

$$\mathbf{V}_t = \dot{r}(t)[cos\theta(t), sin\theta(t)]^T \quad [3\text{-}17]$$

The second component is perpendicular to the direction of **r**(t) and it is rotated by π/2 in a counterclockwise direction. This component represents change of the vector direction.

$$\mathbf{V}_r = r(t)[-sin\theta(t), cos\theta(t)]^T\dot{\theta}(t) \quad [3\text{-}18]$$

In the kinematic analysis of a mechanism the equations for velocities follow from the loop-closure equation for positions. If $r_i = r_i(t)$ and $\theta_i = \theta_i(t)$, then, by differentiating the position vector with respect to t, the following vector equation is obtained:

$$\sum_{i=1}^{N} \dot{r}_i(t)[cos\theta_i(t), sin\theta_i(t)]^T + r_i(t)[-sin\theta_i(t), cos\theta_i(t)]^T\omega_i(t) = 0 \quad [3\text{-}19]$$

Where $\omega_i(t) = \dot{\theta}_i(t)$ is the angular velocity.

In this equation, as in the loop-closure equation, the unknowns can be any two velocity components: two translational, two rotational, or a combination of rotational and translational. The solution will be derived for the case of two unknown angular velocities, which is the case for all the loops in the studied mechanism.

In this case the two unknown angular velocities $\theta_i(t)$ and $\theta_j(t)$ can be easily found from the previous equation:

$$\omega_i r_i \sin(\theta_j - \theta_i) = -\dot{r}_i cos(\theta_j - \theta_i) - \dot{r}_j + \dot{b_x} cos\theta_j + \dot{b_y} sin\theta_j \quad [3\text{-}20]$$

$$\omega_j r_j \sin(\theta_i - \theta_j) = -\dot{r}_j cos(\theta_i - \theta_j) - \dot{r}_i + \dot{b_x} cos\theta_i + \dot{b_y} sin\theta_i \quad [3\text{-}21]$$

- **ACCELERATION ANALYSIS**

In the same way as the velocity vector was obtained from the position vector, the acceleration vector is the time derivative of the velocity vector:

$$\frac{d^2\mathbf{r}}{dt^2} = \ddot{\mathbf{r}} = \ddot{r}[cos\theta, sin\theta]^T + 2\dot{r}[-sin\theta, cos\theta]^T \frac{d\theta}{dt} - r[cos\theta, sin\theta]^T \left(\frac{d\theta}{dt}\right)^2 + r[-sin\theta, cos\theta]^T \frac{d^2\theta}{dt^2} \quad [3\text{-}22]$$

Using the notation $\omega = d\theta/dt$ for the angular velocity and $\alpha = d^2\theta/dt^2$ for the angular acceleration the equation has the form:

$$\ddot{\mathbf{r}} = \ddot{r}[cos\theta, sin\theta]^T + 2\dot{r}[-sin\theta, cos\theta]^T \omega - r[cos\theta, sin\theta]^T \omega^2 + r[-sin\theta, cos\theta]^T \alpha \quad [3\text{-}23]$$

This equation can be rewritten so that the directions of all vectors are referenced with respect to the direction of vector r:

$$\ddot{\mathbf{r}} = \ddot{r}[cos\theta, sin\theta]^T + 2\dot{r}\left[\cos(\theta + \tfrac{\pi}{2}), \sin(\theta + \tfrac{\pi}{2})\right]^T \omega + r[\cos(\theta + \pi), \sin(\theta + \pi)]^T \omega^2 + r[\cos(\theta + \tfrac{\pi}{2}), \sin(\theta + \tfrac{\pi}{2})]^T \alpha \quad [3\text{-}24]$$

These four vectors and their directions are shown in figure 3-9. The first vector ($\ddot{r}$) is the translational component of acceleration, the second ($2\dot{r}\omega$) is called the Coriolis component of acceleration, the third ($r\omega^2$) is the centripetal component of acceleration and the fourth ($r\alpha$) is the angular component of acceleration.

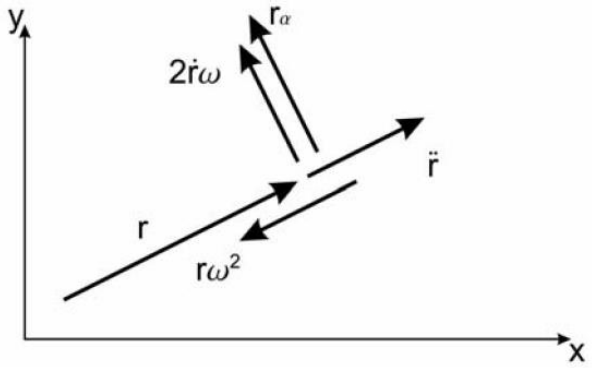

Figure 3-9. Components of acceleration vector [59].

The centripetal and the Coriolis accelerations can be found from the velocity analysis, the first is caused by the rotation of the vector, whereas the Coriolis acceleration is caused by the rotation of a translationary moving vector. The other two components of acceleration, translational and angular, are found as a result of the acceleration analysis.

The equations for obtaining accelerations come from the second differentiation of the loop-closure equation for positions of the equation with respect to time. As a result, the loop-closure equation for accelerations assuming all variables are time-dependent is:

$$\sum_{i=1}^{N} \ddot{r}_i[cos\theta_i, sin\theta_i]^T + 2\dot{r}_i[-sin\theta_i, cos\theta_i]^T\omega_i - r_i[cos\theta_i, sin\theta_i]^T{\omega_i}^2 + r_i[-sin\theta_i, cos\theta_i]^T\alpha_i = 0$$

[3-25]

In this equation the unknowns are $\ddot{r}_i$ and α_i, therefore, there are five possible combinations of these unknowns and the solutions for each can be found from the solutions for the velocities. In the case of two unknown angular accelerations the solutions are:

$$\alpha_i = \frac{1}{r_i \sin(\theta_j - \theta_i)}[(-\omega_i r_i(\omega_j - \omega_i) - \ddot{r}_i)\cos(\theta_j - \theta_i) + \dot{r}_i(\omega_j - 2\omega_i)\sin(\theta_j - \theta_i) - \ddot{r}_j +$$

$$(\ddot{b_x} + \dot{b_y}\omega_i)cos\theta_j + (\ddot{b_y} + \dot{b_x}\omega_j)sin\theta_j] \qquad [3\text{-}26]$$

$$\alpha_j = \frac{1}{r_j \sin(\theta_i - \theta_j)}[(-\omega_j r_j(\omega_i - \omega_j) - \ddot{r}_j)\cos(\theta_i - \theta_j) + \dot{r}_j(\omega_i - 2\omega_j)\sin(\theta_i - \theta_j) - \ddot{r}_i +$$

$$(\ddot{b_x} + \dot{b_y}\omega_j)cos\theta_i + (\ddot{b_y} + \dot{b_x}\omega_i)sin\theta_i] \quad [3\text{-}27]$$

- **KINETIC ANALYSIS – INERTIAL FORCES**

In any mechanism with a mass associated to its links, inertial forces are generated by translational and angular accelerations. Knowing the center of mass of every link j, the motion equations for this link are found:

$$m_j \ddot{\mathbf{r}}_{cj} = \sum \mathrm{F_{ext}} \quad [3\text{-}28]$$

$$I_j \ddot{\theta}_j = \sum \mathrm{M_{ext}} \quad [3\text{-}29]$$

Where:

$\mathbf{r}_{cj}$ is the position vector of the mass center of link j in the global coordinate system

θ_j is the angular coordinate of the link

m_j is the mass of the link

I_j is the moment of inertia of the link

F_{ext} and M_{ext} are the external forces and moments

If the accelerations are known from the kinematic analysis, the inertial forces can be treated as known external forces so that the motion equations can be written in the following form:

$$\sum \mathrm{F_{ext}} + \mathrm{F_{inert}} = 0 \quad [3\text{-}30]$$

$$\sum \mathrm{M_{ext}} + \mathrm{M_{inert}} = 0 \quad [3\text{-}31]$$

$$\mathrm{F_{inert}} = -m_j \ddot{\mathbf{r}}_{cj} \quad \text{and} \quad \mathrm{M_{inert}} = -I_j \ddot{\theta}_j \quad [3\text{-}32]$$

In this way, the problem of solving a moving mechanism with unknown constraint forces is simplified to a problem of static equilibrium with the additional inertial treated as known external forces. This is known as D'Alembert's principle.

3.3.2. KINEMATIC AND DYNAMIC ANALYSIS

Following this method, a Maple code was written that would find the positions, velocities, accelerations and inertial forces for every element in the mechanism as a function of the position of the slider (r1) and as a function of time, when the slider's position was made as a function of time (r1(t)).

First the mechanism was split into four simple closed loop mechanisms with two unknown angles using the outputs obtained for the first loop as inputs for the second, and so on. In this way, the whole compound mechanism was solved as a function of r1 by solving the four simple mechanisms shown in figure 3-10:

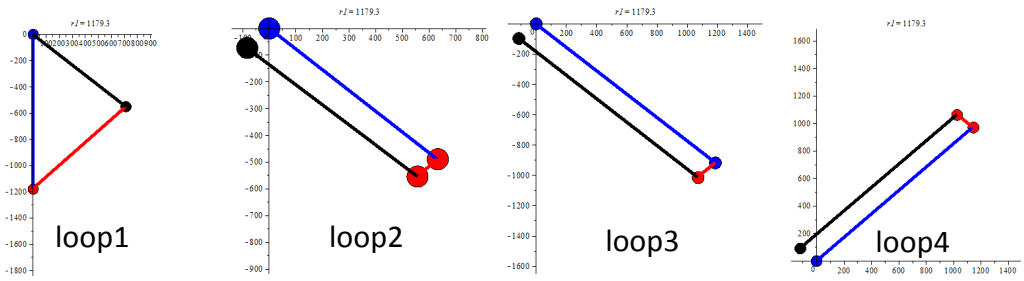

Figure 3-10. Separation of the compound umbrella mechanism into four simple loops.

- **Position analysis – Loop 1**

The first loop consisted of a slider, R1, and two articulated links, R2 and R3, depicted in figure 3-11. The input variables were the angle and the length of R1 and the two unknowns the

angles of the two articulated links, R2 and R3; since the angle of R1, θ1, was fixed at 270°, the output variables were found as a function of the length of R1 (r1).

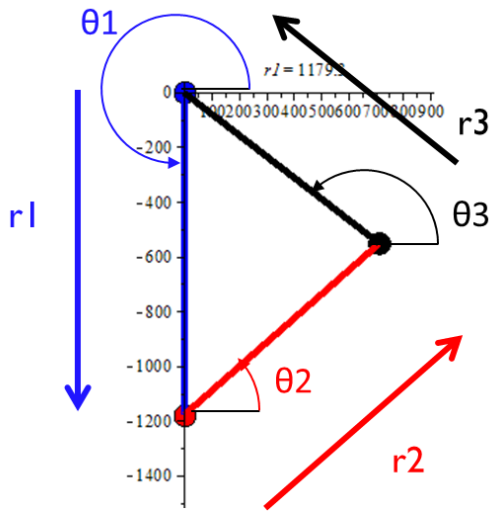

Figure 3-11. Variables in loop 1 of the shield deployment mechanism.

This simple loop is easily solvable using the method described in the previous chapter. In this case, however, it was not necessary to transform the variables θ2 and θ3 since bvec1[x] = R1[x] was already zero and the system was easily solvable without any transformation. Figure 3-12 shows the procedure used to calculate the two unknowns.

Loop-closure equation

$R1 := r1 \cdot \langle \cos(\theta 1), \sin(\theta 1) \rangle :$
$R2 := r2 \cdot \langle \cos(\theta 2), \sin(\theta 2) \rangle :$
$R3 := r3 \cdot \langle \cos(\theta 3), \sin(\theta 3) \rangle :$

$loop1 := R1 + R2 + R3 = 0 :$
Given: *r1, r2, r3, θ1*
Unknown: *θ2, θ3*

Calculation of vector bvec1

$bvec1 := -(R1) :$
$bvec1X := bvec1[1] :$
$bvec1Y := bvec1[2] :$
$b := \sqrt{bvec1X^2 + bvec1Y^2} :$

$\cos\alpha := \frac{bvec1X}{b} :$

$\sin\alpha := \frac{bvec1Y}{b} :$

$\alpha := \arctan(\sin\alpha, \cos\alpha) :$

Calculation of unknown θ2, θ3

$ri := r2 :$
$rj := r3 :$
$\theta j := \theta 3 :$

$Sin\theta j := \frac{\left(b^2 - ri^2 + rj^2\right)}{2\, b \cdot rj} :$

$Sin\theta i := \frac{(b - rj \cdot Sinj)}{ri} :$

$Cos\theta i := \frac{rj}{ri}\sqrt{1 - Sinj^2} :$

$Cos\theta j := -\frac{ri}{rj}\sqrt{1 - Sini^2} :$

Figure 3-12. Calculation of unknowns θ2 and θ3.

- **Position analysis – Loop 2**

The second loop was a four-bar mechanism where the two input angles, θ4 and θ7, were known from the solution of loop 1; θ4 = θ3 +180° and θ7 = θ2. Figure 3-13 depicts the variables in the loop closure equation for the second loop. This second loop also had two unknown angles, θ5 and θ6, and was solved in the same way as the previous loop, this time using the variable transformation to simplify the resolution.

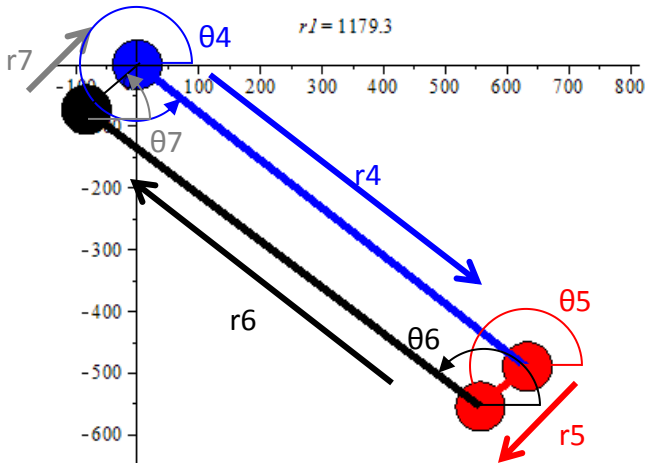

Figure 3-13. Variables in loop 2 of the shield deployment mechanism.

- **Position analysis – Loops 3 and 4**

The two last loops were two four-bar mechanisms where the bars on opposite sides were of equal lengths. Therefore, the bars opposite to each other were parallel and all angles were known. In these two cases all angles were already known as a function of r1 without the need of solving the loop closure equations.

- **Velocity and acceleration analysis**

With the motion of every link in the mechanism defined as a function of the slider's position, r1, the next step was to find their velocities and accelerations. r1 was made a sinusoidal function of time, shown in figure 3-14, and the angular velocities and accelerations of every link were found by differentiating their angular position.

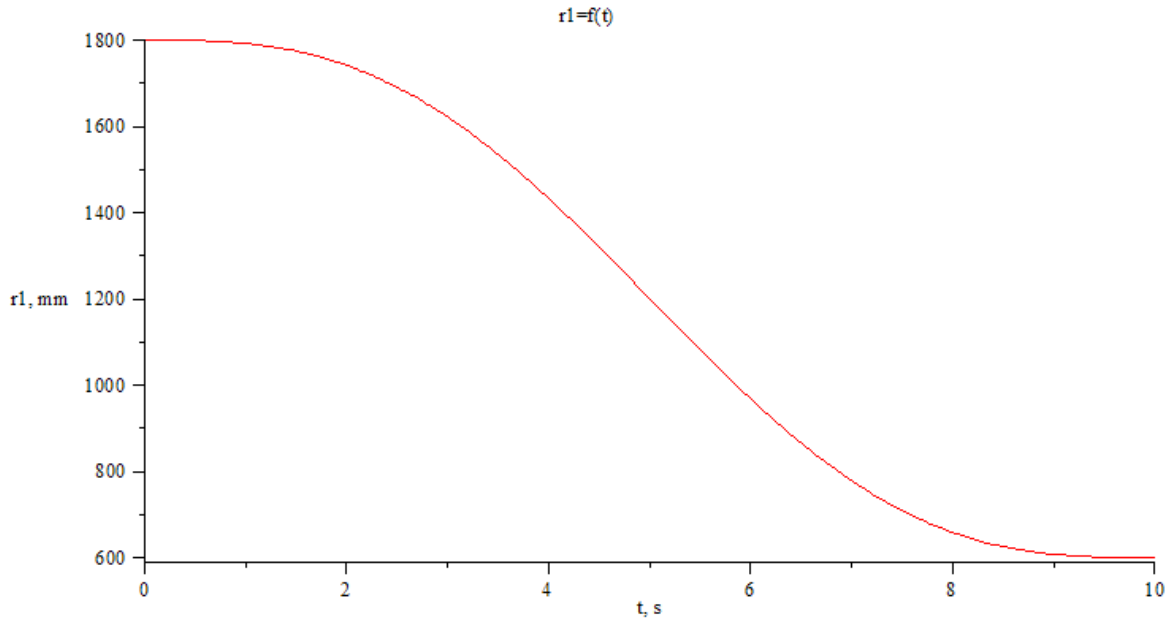

$$r1 := r1MAX + \frac{(r1min - r1MAX)}{tf} \cdot t - \frac{(r1min - r1MAX)}{2 \cdot evalf(\mathrm{Pi})} \cdot \sin\left(\frac{t}{tf} \cdot 2 \cdot evalf(\mathrm{Pi})\right) :$$

Figure 3-14. r1(t).

By making r1(t) sinusoidal, all angular velocities and accelerations were kept smooth and finite. Figure 3-15 shows the angular velocity and acceleration of link R3 as a function of time; the full code with plots of angular velocities and accelerations of all links can be found in Appendix B.

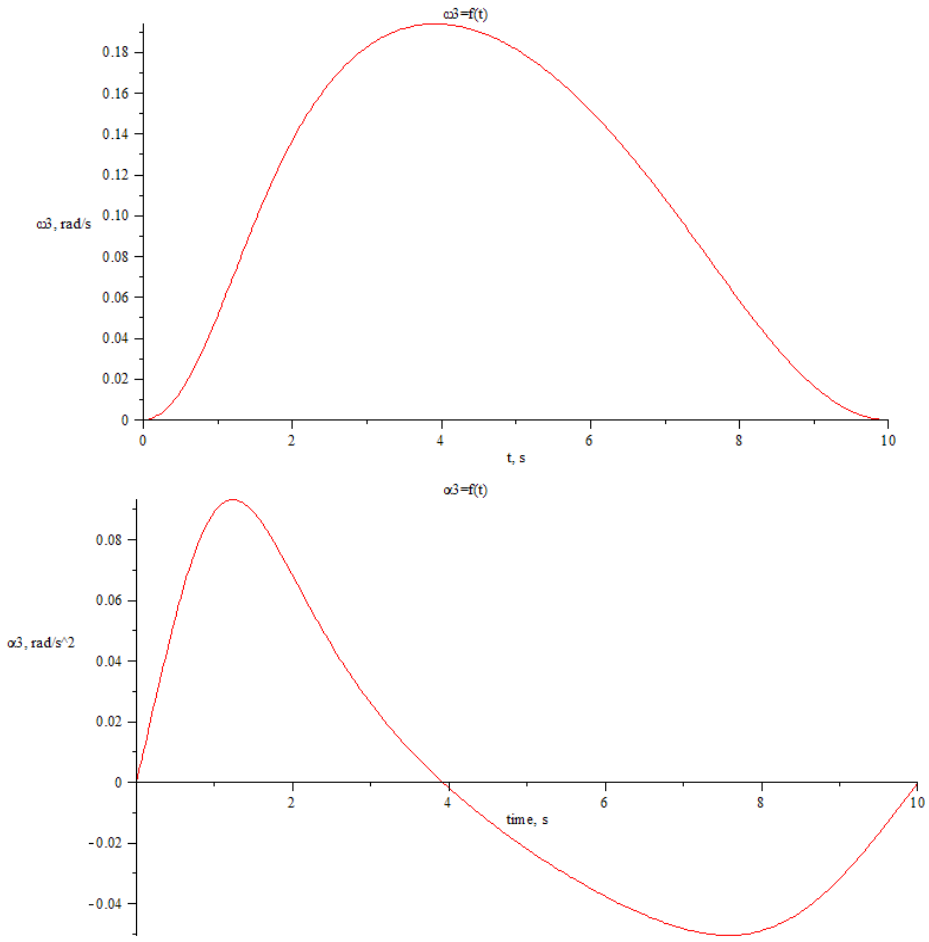

Figure 3-15. Angular velocity (top) and acceleration (bottom) of link R3 as a function of time.

- **Inertial force analysis**

For the calculation of the inertial forces it was assumed that the mass of the links in the mechanism was negligible in comparison to the mass of the shielding carried by them. By doing this, the problem is simplified and only the four top bars carrying the layer of shielding generate inertial forces.

First, the position of the center of mass on each of the four supporting bars was calculated and their trajectories were found, as shown in figure 3-16.

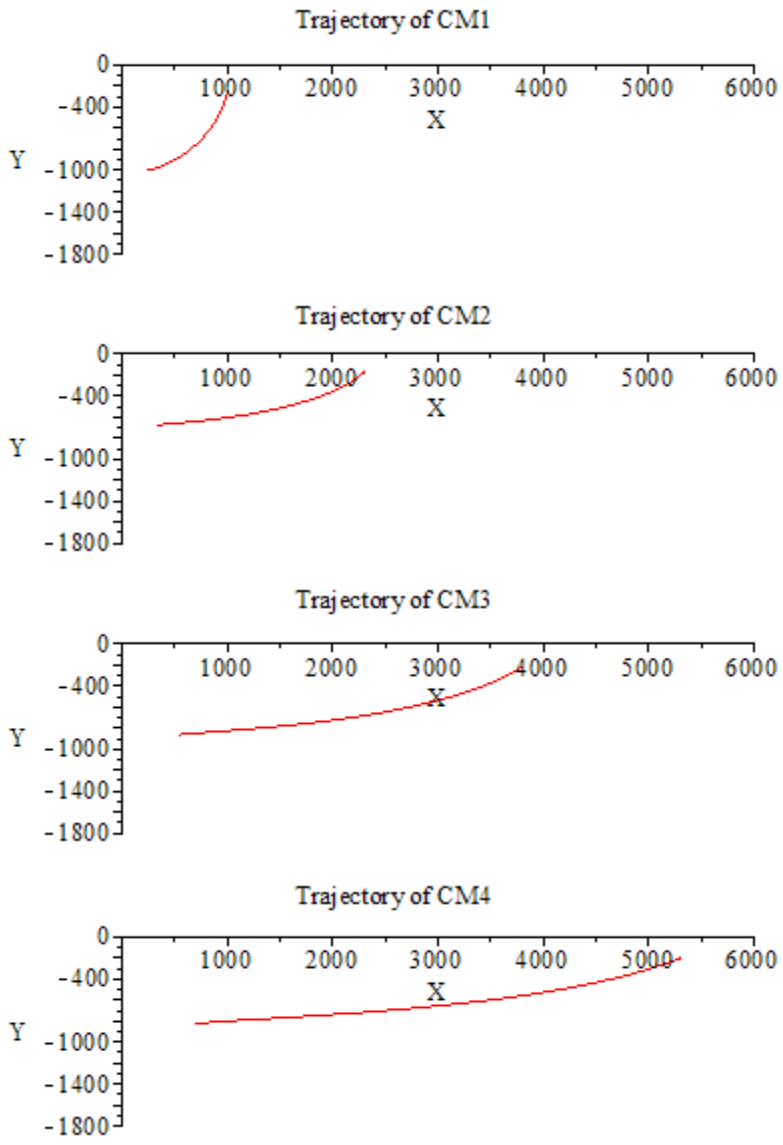

Figure 3-16. Trajectories of centers of mass of the four segments of shielding.

Each of these four vectors representing the position of the centers of mass consisted of a horizontal and a vertical component, which were differentiated twice to obtain the horizontal and vertical components of their accelerations. By multiplying these values by the mass associated with each segment of shielding the two components of the inertial forces acting on each of the centers of mass were obtained. Figure 3-17 shows the two components of the inertial force acting on the fourth segment of shielding: this was the segment that underwent the greatest

acceleration and, therefore, felt the greatest force; the rest of the plots can be found in Appendix B.

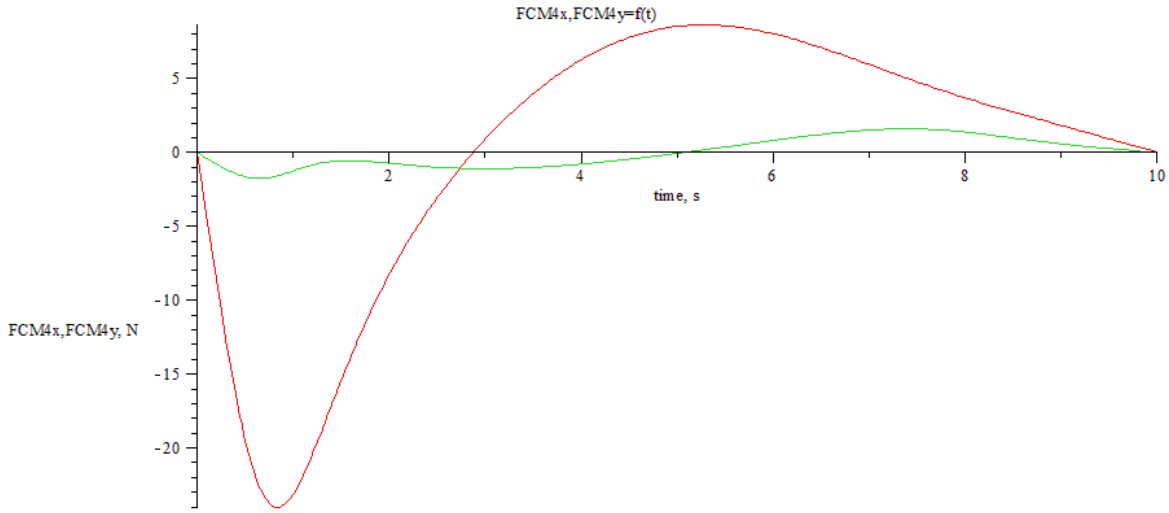

Figure 3-17. $F_{CM4}[x]$ (red) and $F_{CM4}[y]$ (green) as a function of time.

3.3.3. FINAL DEPLOYMENT MECHANISM DISCUSSION

After going through the kinematic and dynamic analysis of the mechanism, it was concluded that the modified umbrella mechanism used for the shield deployment was adequate. Since the mechanism was designed to be opened in orbit, the only forces acting on it were the inertial forces associated with the acceleration of the segments of shielding. With a sinusoidal motion of the slider (r1) lasting 10 seconds, the greatest of the 4 inertial forces acting on each branch of the deployment mechanism was of 25 N. These results showed that the implementation of such a mechanism for the shield deployment was feasible. Furthermore, by slowing down the motion of the slider (r1), the resulting accelerations and inertial forces could be decreased even further.

Finally, to complete the design of the deployment mechanism, the sections of each bar and the type and dimensions of the joints should be optimized. By solving the static equilibrium problem using the values of the inertial forces and moments as the external forces, the loads

acting on each bar and articulation can be found and this, in turn, will allow the minimum dimensions of each element to be determined.

4. SERVICE MODULE DESIGN

To conclude the conceptual design, once the shield and the deployment mechanism had been completed, a general design of the rest of the spacecraft that would carry them was made. Since this spacecraft was not intended to carry any payload other than the shield and its deployment mechanism, this stage in the design focused on selecting the components for the service module. The focus of this project was to explore the feasibility of shielding from larger projectiles along with the mechanism for its deployment. However, it was considered important to have, at least, a general design of the service module to demonstrate the feasibility of the spacecraft as a whole.

4.1. REVIEW OF SERVICE MODULE REQUIREMENTS

For the selection of the service module's components, the basic elements necessary for a satellite to function were reviewed [60], [61]. These are outlined below:

- **Bus/structural subsystem**: The bus is the structure or frame on which the other elements are mounted. It must bear the stresses of launch, so it must be resilient, and to limit the solar heat it absorbs, it can be covered with a reflective coating.

- **Thermal regulation subsystem:** On a satellite, heat is generated by active components such as the computer or receiver as well as by incident sunlight and for the active parts of the satellite to work properly they must be kept cool. Since there is no atmosphere, conduction and convection cannot be used and all the heat must be extracted through radiation. Generally the thermal regulation system consists of radiators and thermally conducting pathways but in some cases cryogenic cooling may be used.

- **Power source:** The power required by the satellite's active components is usually generated by solar cells, although other sources such as fuel cells or nuclear reactors may also be used, and stored in rechargeable batteries to ensure power supply at all times.

- **Computer control system:** The on-board computer monitors and processes data from all the satellite's subsystems and controls their actions.

- **Communications system:** This system, which usually consists of a receiver, a transmitter and at least one antenna, forms the link between the satellite and its ground stations or other satellites.

- **Attitude control system:** This system controls the orientation of the satellite while in orbit and may include gyroscopes, accelerometers and visual guidance systems.

- **Propulsion subsystem:** The satellite's propulsion subsystem can include a main engine to deliver it to its desired orbit after launch as well as small thrusters for stationkeeping and attitude control once it is in orbit.

4.2. SPACECRAFT DESIGN

With the previous requirements in mind, to simplify the design, the service module was modelled after that of an existing satellite. The ESA's Gaia satellite, launched on 19 December 2013, was chosen as the model for the design of the service module because it was launched recently, so its components were up to date, and its shape and dimensions were suitable for this spacecraft as well. A diagram of Gaia's service module is shown in figure 4-1 below.

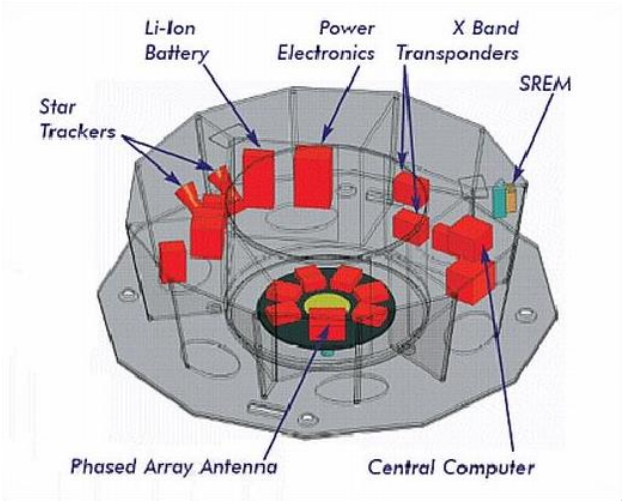

Figure 4-1. Diagram of the Gaia satellite's service module [62].

With the Gaia satellite as a reference the following components were selected for the spacecraft's service module [63], [64]:

- **Micro propulsion system**: 12 cold gas thrusters for attitude control on the service module, an additional 12 thrusters on the shield because of its additional mass with respect to the Gaia satellite and an estimate of 100 kg of propellant.

- **Chemical propulsion system**: The Gaia satellite required a chemical propulsion system to place it into its Lissajous-type orbit around L2 (Lagrangian Point 2), about 1.5 million km from Earth. In the case at hand no propulsion of this sort was necessary, since the spacecraft is to be placed directly into its desired orbit in LEO. This allowed for a significant reduction in size and mass, by removing the main propulsion system and its propellant.

- **Navigation and control**: Three gyroscopes, star trackers, three fine sun sensors for attitude control.

- **Power**: Although the shield will generally not be oriented towards the sun, its large area makes it a reasonable location to place solar cells. Alternatively, solar cells could be placed

on the side of the spacecraft and shielding, which might provide a higher efficiency. The same six solar cells with a total 12.8 m^2 and 1910 W of capability and 72 Amp-hour battery used in the Gaia satellite should be enough, taking into account the lower power requirement due to the lack of a payload module and the lower efficiency due to non-optimal orientation of the cells. An estimate of the power requirements is shown in Table VIII.

Since the spacecraft is intended to travel alongside the satellite it is protecting (e.g. ISS or other large structures), there is the possibility of linking the two together to share their power. For example, at times when the solar cells of the shield generate excess power, this could be transferred to the spacecraft behind it.

TABLE VIII. ESTIMATED POWER REQUIREMENTS.

Component	Power
RF Communications	326 W
Data Management and AOCS	103 W
Electrical power & solar array	117 W
Propulsion	24 W
TOTAL	**570 W**

- **Communication system**: Three Low Gain Antennas: the medium gain Phased Array Antenna used in the Gaia satellite for science data and telemetry downlink is not required in this case.

- **Thermal tent**: CFRP sandwich panels covered in MLI and a thermal radiator. The thermal tent also protects the electronics from radiation and contamination.

With all the basic components selected, a general layout and estimation of the overall weight of the service module were made. Following the model of the Gaia satellite in Figure 4-, the

service module was housed in a cylindrical structure with a smaller cylinder inside, in which the propellant is stored. The inner cylinder was also made to accommodate the actuator for the shield deployment mechanism. The rest of the components, excepting the thrusters, were located around the inner cylinder. Figure 4-2 shows a cross section of the service module with a diagram showing a possible layout for its components; the module is 2 m in diameter and 1.5 m in height and its estimated mass, 900 kg, is based on the previous component selection.

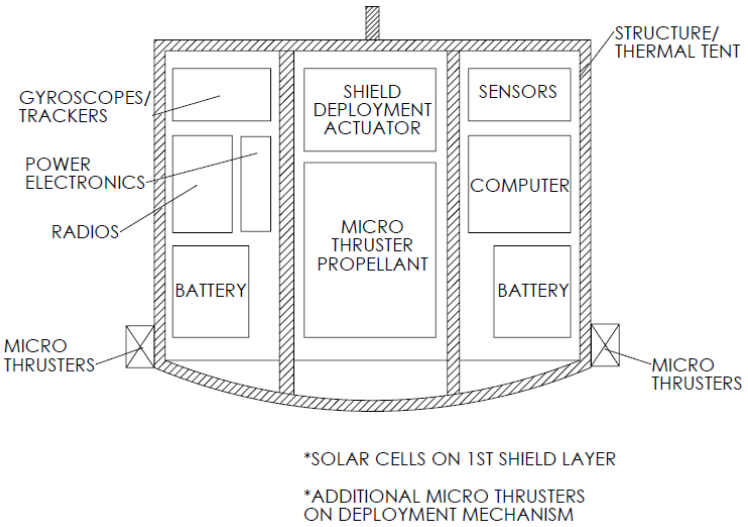

Component	Estimated mass
Service module	800 kg
Micro propulsion propellant	100 kg
TOTAL	**900 KG**

Figure 4-2. Possible layout for the service module (top) and an estimate of its overall mass (bottom).

5. FINAL DESIGN SUMMARY, CONCLUSIONS AND RECOMMENDATIONS

With all three design stages complete, the final design for the spacecraft was put together. This final design is shown in figure 5-1 and is summarized below.

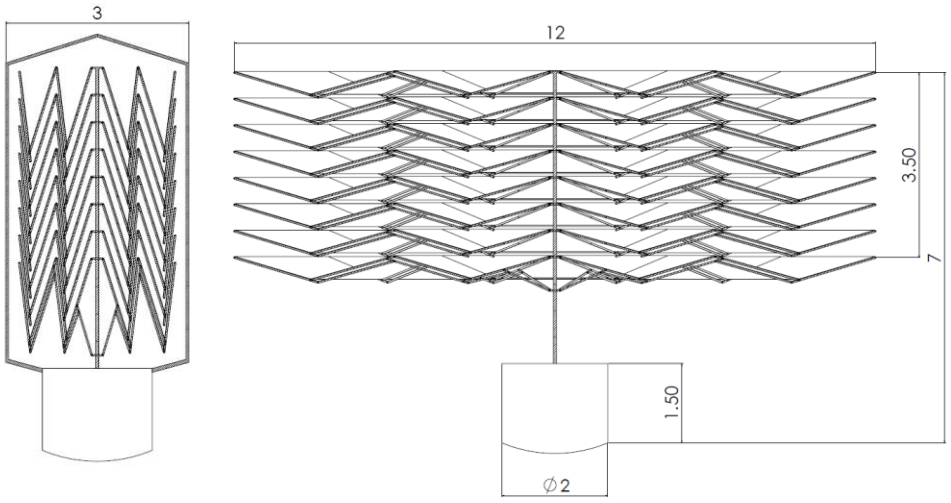

Figure 5-1. Final design of the "Defender" spacecraft for OD protection, dimensions in m.

- **Orbital debris shield**: The orbital debris shield consists of 8 layers of shielding with a 500 mm standoff between each layer; the first three are 2 mm diameter Al 7039 wire mesh in a square pattern with a wire every 5 mm and the next five are 2 mm thick Al 7039 plate. It has an overall areal density of 3.72 g/cm^2 and covers an octagonal area with an outside diameter of 12 m, resulting in a total mass of 4200 kg.

- **Deployment mechanism**: The deployment mechanism is based on a foldable umbrella and folds the shield from a 12 m diameter octagonal shape down to a 2.8 m diameter fitted into a 3 m diameter cover. Its final dimensions are shown in figure 5-2. The only loads on the mechanism as it opens in orbit are the inertial forces and, therefore, the mechanism can be very lightweight.

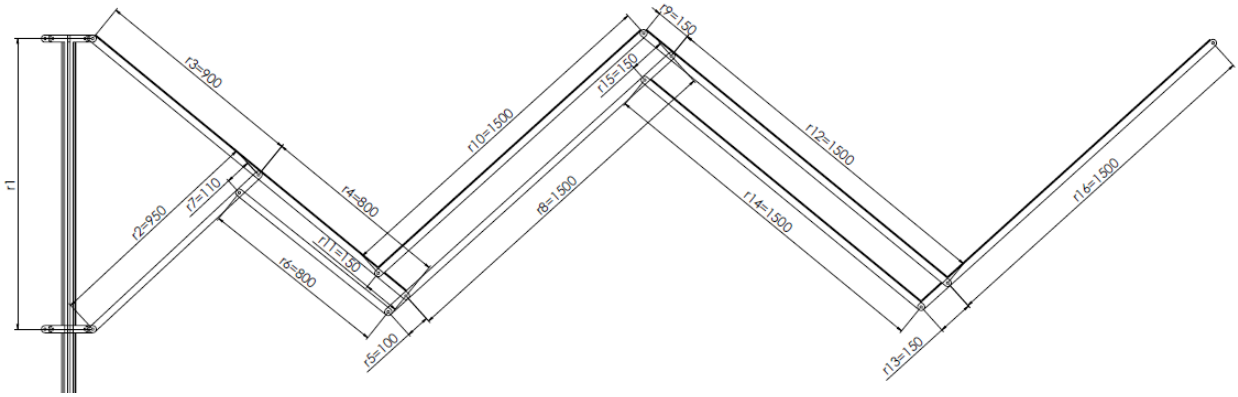

Figure 5-2. Final deployment mechanism dimensions in mm.

It's worth mentioning that, although the spacecraft was designed with a 12 m diameter shield, the deployment mechanism can easily be extended to cover a greater area by adding bars, as can be seen in figure 5-3.

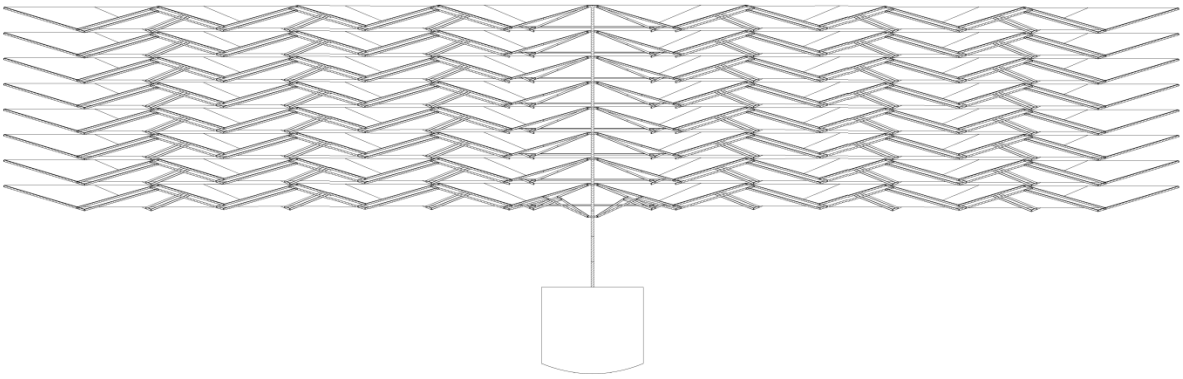

Figure 5-3. "Defender" spacecraft with an extended shield for the protection of larger spacecraft.

- **Service module**: The service module, based on that of the Gaia satellite's one, has a 2 m diameter cylindrical structure with a height of 1.5 m and an estimated mass of 900 kg.

Overall, the spacecraft has a 2.8 m diameter and 7 m length when the shield is folded and a 12 m diameter and 7 m length when the shield is deployed. The total mass at launch is estimated at 5100 kg. Figure 5-4 is a 3D render of what the spacecraft could look like in operation.

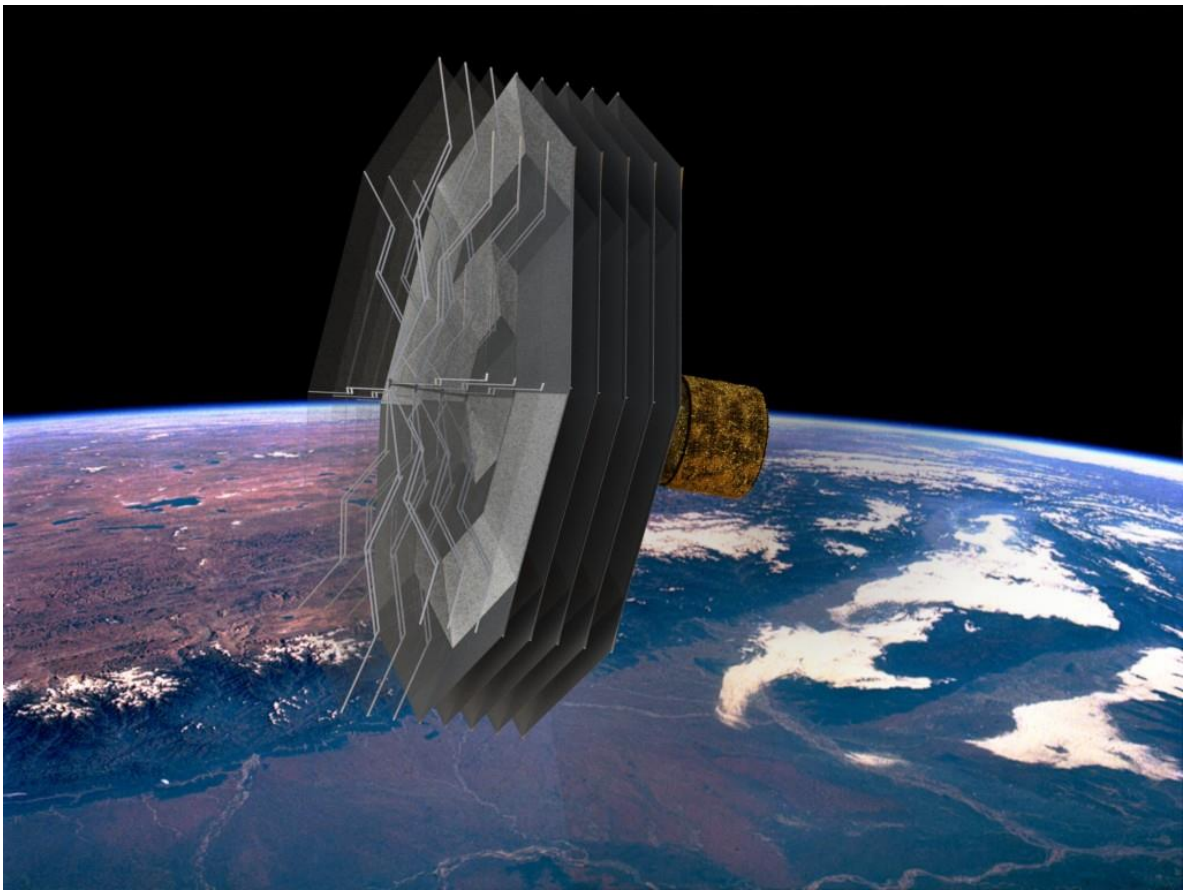

Figure 5-4. 3D render of the final spacecraft design.

After completing the conceptual design it can be concluded that the use of a "defender" spacecraft of this type for the OD protection of larger structures in orbit is a feasible option that could successfully protect such structures from unforeseeable collisions.

Although a thorough cost analysis would have to be done in each case, the spacecraft's mass and dimensions are within what can be considered reasonable for a satellite in LEO and, therefore, the cost associated with this method of protection should be justifiable for large, high-value spacecraft such as the ISS or missions where the life of astronauts could be at risk. Taking into consideration the growing orbital debris population and the growing probability of impact from objects large enough to cause serious damage to spacecraft but small enough to go

undetected, the cost of using a spacecraft of this type for protection would be relatively low compared to the cost of the potential damage from a single collision.

Since this is an initial conceptual design, however, much work remains to be done before this measure could successfully be employed for OD protection. Therefore, recommendations for the further development of this spacecraft are given below.

First, the shield used in the conceptual design was merely the first that was found that fit the requirements; with a more in-depth study, considering alternative materials and layer configurations, the mass of the shield could be greatly reduced. At the same time, the use of fabric based materials, such as Nextel and Kevlar, instead of rigid materials would simplify the deployment mechanism.

As for the deployment mechanism, it was seen that the inertial forces involved were relatively low. Nevertheless, a more in-depth analysis should be made to determine the loads on every bar and joint in the mechanism and optimize their dimensions. Furthermore, the effect on the mechanism of the acceleration at launch and of an impact by a projectile should also be studied.

Finally, since the main focus in this project was the design of the shield and its deployment mechanism, only a general component selection for the service module was made and a more complete design of the service module should be undertaken.

As a final conclusion, even though this is a conceptual design and there is still a lot of work to be done, the project has achieved its objective of showing that the use of a spacecraft of this type for orbital debris protection is a feasible option with great potential benefit for the safety of future missions in LEO as well as for the orbital debris environment as a whole.

BIBLIOGRAPHY / REFERENCES

[1] ESA. (2013, April 20) *Space Debris FAQ: Frequently Asked Questions* [Online]. Available: http://www.esa.int/Our_Activities/Operations/Space_Debris/FAQ_Frequently_asked_questions. [Oct. 13, 2013].

[2] J. Schefter. (1982, July) "The growing peril of space debris," Popular Science, vol. 221 (1), p. 48.

[3] NASA. (2012). *Orbital Debris Management & Risk Mitigation* [Online]. Available: http://www.nasa.gov/pdf/692076main_Orbital_Debris_Management_and_Risk_Mitigation.pdf [Oct. 13, 2013].

[4] "Fifty years ago," (2013, July), *Orbital Debris Quarterly News* [Online], vol. 17 (3), pp. 2-3. Available: http://orbitaldebris.jsc.nasa.gov/newsletter/pdfs/ODQNv17i3.pdf [Oct. 13, 2013].

[5] European Space Agency. (2008, Oct. 4). "Trackable_objects_in_orbit_around_Earth_node_full_image.jpg" in *ESA* [Online]. Available: http://spaceinimages.esa.int/Images/2008/03/Trackable_objects_in_orbit_around_Earth [Oct. 13, 2013].

[6] European Space Agency. (2008, Oct. 4). "Debris_objects_-_mostly_debris_-_in_low_Earth_orbit_LEO_-_view_over_the_equator_node_full_image.jpg" in ESA [Online]. Available: http://spaceinimages.esa.int/Images/2008/03/Debris_objects_-_mostly_debris_-_in_low_Earth_orbit_LEO_-_view_over_the_equator [Oct. 13, 2013].

[7] ESA. (2013, Apr. 20). *Scanning & Observing* [Online]. Available: http://www.esa.int/Our_Activities/Operations/Space_Debris/Scanning_observing [Oct. 13, 2013].

[8] "An update of the FY-1C, Iridium 33, and Cosmos 2251 fragments," (2013, Jan.), *Orbital Debris Quarterly News* [Online], vol. 17 (1), pp. 4-5. Available: http://orbitaldebris.jsc.nasa.gov/newsletter/pdfs/ODQNv17i1.pdf [Oct. 13, 2013].

[9] "Monthly number of objects in earth orbit by object type," (2013, Jan.), *Orbital Debris Quarterly News* [Online], vol. 17 (1), p. 8. Available: http://orbitaldebris.jsc.nasa.gov/newsletter/pdfs/ODQNv17i1.pdf [Oct. 13, 2013].

[10] Committee on Space Debris, Aeronautics and Space Engineering Board, Commission on Engineering and Technical Systems and National Research Council. "Hazards to space operations from debris," in *Orbital Debris: A Technical Assessment*, Washington, D.C.: National Academy Press, 1995, pp. 79 – 100.

[11] IADC. (2007). *IADC Space Debris Mitigation Guidelines* [Online]. Available: http://www.iadc-online.org/Documents/IADC-2002-01,%20IADC%20Space%20Debris%20Guidelines,%20Revision%201.pdf [Oct. 13, 2013].

[12] IADC. (2013, Feb.). *Stability of the Future LEO Environment* [Online]. Available: http://www.iadc-online.org/Documents/IADC-2012-08,%20Rev%201,%20Stability%20of%20Future%20LEO%20Environment.pdf [Oct. 13, 2013].

[13] European Space Agency. (2013, Sept. 9). "Why_Space_Debris_Mitigation_is_needed_node_full_image.gif" in *ESA* [Online]. Available: http://spaceinimages.esa.int/Images/2013/04/Why_Space_Debris_Mitigation_is_needed [Oct. 13, 2013].

[14] "Monthly number of objects in earth orbit by object type," (2013, Jan.), *Orbital Debris Quarterly News* [Online], vol. 17 (1), p. 8. Available: http://orbitaldebris.jsc.nasa.gov/newsletter/pdfs/ODQNv17i1.pdf [Oct. 13, 2013].

[15] J. Mason, J. Stupl, W. Marshall and C. Levit. (2011, July). *Orbital Debris-Debris Collision Avoidance*, [Online] Available: http://arxiv.org/pdf/1103.1690v3.pdf [Nov. 20, 2013].

[16] R. A. Williamson. (2012, Dec.). *Orbital Debris Removal: Technical, Policy, and Legal Issues* [Online]. Available: http://swfound.org/media/98096/debrisremoval-raywilliamson-dec2012.pdf [Nov. 20, 2013].

[17] Committee on Space Debris, Aeronautics and Space Engineering Board, Commission on Engineering and Technical Systems and National Research Council. "Damage protection techniques," in *Orbital Debris: A Technical Assessment*, Washington, D.C.: National Academy Press, 1995, pp. 122-129.

[18] NASA. (2013, Sept. 27). *Space Debris and Human Spacecraft* [Online]. Available: http://www.nasa.gov/mission_pages/station/news/orbital_debris.html#.Uxor5_mwIRo [Oct. 13, 2013].

[19] Committee on International Space Station Meteoroid/Debris Risk Management, Aeronautics and Space Engineering Board, Commission on Engineering and Technical Systems and National Research Council. (1997). "Shielding the International Space Station," in *Protecting the Space Station from Meteoroids and Orbital Debris* [Online], Washington, D.C.: National Academy Press, pp. 27-38. Available: http://www.nap.edu/catalog.php?record_id=5532 [Oct. 13, 2013].

[20] BBC. (2013, May 24). "Ecuador Pegasus satellite fears over space debris crash" *BBC News*. [Online]. Available: http://www.bbc.co.uk/news/world-latin-america-22635671 [Oct. 13, 2013].

[21] P. Blau. (2013, Mar. 9). "Russian BLITS satellite hit by space debris" *Spaceflight101*. [Online]. Available: http://www.spaceflight101.com/blits-satellite-collision-january-2013.html [Oct. 13, 2013].

[22] A.V. Kudjakov. Concept of the "bodyguard" spacecraft. Personal communication.

[23] E.L.Christiansen (1990) "Advanced Meteoroid and Debris Shielding Concepts", AIAA/NASA/DOD Orbital Debris Conference, Technical Issues & Future Directions, Baltimore, MD, pp 1-14.

[24] Hypervelocity Impact Shield, by J.L.Crews and B.G.Cour-Palais. (1991). US Patent 5067388 [Online]. Available: http://www.google.com/patents/US5067388.pdf [March 15, 2014].

[25] Enhanced Whipple Shield, by J.L.Crews, E.L.Christiansen, J.E.Williamsen, J.R.Robinson and A.N.Nolen. (1997). US Patent 5610363 [Online]. Available: https://docs.google.com/viewer?url=patentimages.storage.googleapis.com/pdfs/US5610363.pdf [March 15, 2014].

[26] I. Telitchev and A. Prokhorov. (1997). ”Damage parameters analysis of shielded pressure vessels under space debris impact,” *Space Debris: Proceedings Of The Second European Conference, ESOC, Darmstadt, Germany, 17-19 March 1997* [Online], vol. 393, pp. 549-552. Available: http://adsabs.harvard.edu/full/1997ESASP.393..549T [March 15, 2014].

[27] Committee on Space Debris, Aeronautics and Space Engineering Board, Commission on Engineering and Technical Systems and National Research Council. "Methods for characterization," in *Orbital Debris: A Technical Assessment*, Washington, D.C.: National Academy Press, 1995, pp. 31 – 62.

[28] NASA. (2012). "Tracking and Avoiding Collisions with Orbital Debris," in *Orbital Debris Management & Risk Mitigation* [Online]. pp. 12 – 20. Available: http://www.nasa.gov/pdf/692076main_Orbital_Debris_Management_and_Risk_Mitigation.pdf [Oct. 13, 2013].

[29] M.D. Hejduk, H.M. Cowardin, and E.G. Stansbery. (2012). "4. Shape information," in *Satellite Material Type and Phase Function Determination in Support of Orbital Debris Size Estimation* [Online]. p.7. Available: http://ntrs.nasa.gov/archive/nasa/casi.ntrs.nasa.gov/20120015337_2012015216.pdf [Dec. 27, 2013].

[30] E. L. Christiansen. (2009). "2.6.2 Orbital debris environment model," in *Handbook for Designing MMOD Protection* [Online]. p. 15. Available: http://ntrs.nasa.gov/archive/nasa/casi.ntrs.nasa.gov/20090010053_2009007425.pdf [Nov. 20, 2013].

[31] ESA. (2013, Apr. 20). *Operations* [Online]. Available: http://www.esa.int/Our_Activities/Operations/What_are_hypervelocity_impacts [Oct. 13, 2013].

[32] R. Kinslow. (1970). *High-velocity impact phenomena* [Online]. New York, NY: Academic Press. Available: http://www.sciencedirect.com/science/book/9780124089501 [Nov. 20, 2013].

[33] E. L. Christiansen. (2009). “4.2.1 impact physics,” in *Handbook for Designing MMOD Protection* [Online]. pp. 43-46. Available: http://ntrs.nasa.gov/archive/nasa/casi.ntrs.nasa.gov/20090010053_2009007425.pdf [Nov. 20, 2013].

[34] European Space Agency. (2013, April 20). "Hypervelocity_Impact_node_full_image" in *ESA* [Online]. Available: http://www.esa.int/spaceinimages/Images/2013/04/Hypervelocity_Impact [Nov. 20, 2013].

[35] E. L. Christiansen. (2009). “1.1 MMOD Shielding Background,” in *Handbook for Designing MMOD Protection* [Online]. p. 2. Available: http://ntrs.nasa.gov/archive/nasa/casi.ntrs.nasa.gov/20090010053_2009007425.pdf [Nov. 20, 2013].

[36] E. L. Christiansen. (2003). “Section 3 shielding development and material selection,” in *Meteoroid/Debris Shielding* [Online]. pp. 21-41. Available: http://ston.jsc.nasa.gov/collections/trs/_techrep/TP-2003-210788.pdf [Nov. 22, 2013].

[37] E. L. Christiansen. (2003). “Section 4 ballistic limit equations for spacecraft meteoroid/debris shielding,” in *Meteoroid/Debris Shielding* [Online]. pp. 42-56. Available: http://ston.jsc.nasa.gov/collections/trs/_techrep/TP-2003-210788.pdf [Nov. 22, 2013].

[38] IADC. (2012). “3.1.2 Multiple wall structures,” in *Protection Manual* [Online]. pp. 81-103 Available: http://www.iadc-online.org/Documents/IADC-2004-03,%20IADC%20Protection%20Manual,%20Version%205.pdf [Oct. 13, 2013].

[39] E. L. Christiansen. (2009). “Equations for Designing MMOD Shields,” in *Handbook for Designing MMOD Protection* [Online]. pp. 33-80. Available: http://ntrs.nasa.gov/archive/nasa/casi.ntrs.nasa.gov/20090010053_2009007425.pdf [Nov. 20, 2013].

[40] NASA. (23 Oct. 2013). *Hypervelocity Impact Testing* [Online]. Available: http://www.nasa.gov/centers/wstf/laboratories/hypervelocity/#.UsbO3PRDvz4. [Nov. 20, 2013].

[41] Committee on International Space Station Meteoroid/Debris Risk Management, Aeronautics and Space Engineering Board, Commission on Engineering and Technical Systems and National Research Council. (1997). "Shielding the International Space Station," in *Protecting the Space Station from Meteoroids and Orbital Debris* [Online]. Washington, D.C.: National Academy Press, pp. 27-38. Available: http://www.nap.edu/catalog.php?record_id=5532 [Oct. 13, 2013].

[42] E. L. Christiansen. (2009). “4.7 Mesh Double-Bumper Shield,” in *Handbook for Designing MMOD Protection* [Online]. p. 76. Available: http://ntrs.nasa.gov/archive/nasa/casi.ntrs.nasa.gov/20090010053_2009007425.pdf [Nov. 20, 2013].

[43] G. R. Liu and M. B. Liu. “Introduction,” in *Smoothed Particle Hydrodynamics A Mesh Free Method*, Singapore: World Scientific Publishing Co. Pte. Ltd., 2003, pp. 1-32.

[44] R. A. Gingold and J. J. Monaghan. “Smoothed particle hydrodynamics - theory and application to non-spherical stars,” *Monthly Notices of the Royal Astronomical Society*, vol. 181, pp. 375-389, Nov., 1977.

[45] C. J. Hayhurst, R. A. Clegg, I. H. Livingstone, and N. J. Francis, *The Application of SPH Techniques in Autodyn-2D™ to ballistic impact problems*, [Online]. Available: http://hsrlab.gatech.edu/AUTODYN/papers/paper038.pdf [Dec. 27, 2013].

[46] P. Omidavar. "Wave Loading on Bodies in the Free Surface Using Smoothed Particle Hydrodynamics (SPH)" [Online], Ph.D., Faculty of Eng. and Phys. Sci., University of Manchester, Manchester, UK, 2010. Available: http://cfd.mace.manchester.ac.uk/sph/SPH_PhDs/2010/OMIDVAR_Pourya_PhD_Thesis_2010.pdf [March 15, 2014].

[47] ANSYS Inc. "Density calculation," *Introduction to ANSYS AUTODYN,* ch. 9-5. 2011.

[48] S. Beissel and T. Belytschko. (1996). "Nodal integration of the element-free Galerkin method," *Computer Methods in Applied Mechanics and Engineering* [Online], vol. 139 (1-4), pp. 49-74. Available: http://www.sciencedirect.com/science/article/pii/S0045782596010791 [March 15, 2014].

[49] *ANSYS Autodyn v. 14.0*. Computer software. ANSYS, Inc. Windows-PC, 2011.

[50] B.M. Corbett. (2006). "Numerical simulations of target hole diameters for hypervelocity impacts into elevated and room temperature bumpers," *International Journal of Impact Engineering*, [Online]. vol. 33 (1-12), pp. 431-440. Available: http://www.sciencedirect.com/science/article/pii/S0734743X06002028 [March 15, 2014].

[51] D.R. Jenkins. *Space Shuttle: The History of the National Space Transportation System*, 3rd ed. Michigan, : Voyageur Press, 2001.

[52] Wikipedia. "Umbrella_opened.svg" [Online]. Available: http://upload.wikimedia.org/wikipedia/commons/e/e9/Umbrella_opened.svg [March 15, 2014].

[53] Wikipedia. "Umbrella-C7068.jpg" [Online]. Available: http://upload.wikimedia.org/wikipedia/commons/f/f7/Umbrella-C7068.jpg [March 15, 2014].

[54] Wikipedia. "Brise_Fan_LACMA_33.32.jpg" [Online]. Available: http://upload.wikimedia.org/wikipedia/commons/7/71/Brise_Fan_LACMA_33.32.jpg [March 15, 2014].

[55] Wikipedia. "How_to_put_the_ship_in_bottle.gif" [Online]. Available: http://upload.wikimedia.org/wikipedia/commons/0/06/How_to_put_the_ship_in_bottle.gif [March 15, 2014].

[56] O. Vinogradov. *Fundamentals of Kinematics and Dynamics of Machines and Mechanisms* [Online]. New York: CRC Press, 2000. Available: http://dx.doi.org.proxy2.lib.umanitoba.ca/10.1201/9781420042337 [March 20, 2014].

[57] O. Vinogradov. (2000). “Figure 2.4 schematic diagram of an internal combustion engine” in *Fundamentals of Kinematics and Dynamics of Machines and Mechanisms*, [Online]. New York: CRC Press. p. 20. Available: http://dx.doi.org.proxy2.lib.umanitoba.ca/10.1201/9781420042337 [March 20, 2014].

[58] O. Vinogradov. (2000). “Figure 2.5 skeleton of slider-crank mechanism (a) and its vector representation (b)” in *Fundamentals of Kinematics and Dynamics of Machines and Mechanisms*, [Online]. New York: CRC Press. p. 21. Available:

http://dx.doi.org.proxy2.lib.umanitoba.ca/10.1201/9781420042337 [March 20, 2014].

[59] O. Vinogradov. (2000). “Figure 2.40 components of acceleration vector” in *Fundamentals of Kinematics and Dynamics of Machines and Mechanisms*, [Online]. New York: CRC Press. p. 52. Available: http://dx.doi.org.proxy2.lib.umanitoba.ca/10.1201/9781420042337 [March 20, 2014].

[60] D. Wright, L. Grego and L. Gronlund. (2005). “Elements of a satellite system,” in *The Physics of Space Security A Reference Manual*. [Online]. Cambridge, MA: American Academy of Arts and Sciences, ch. 10. pp. 109-116. Available: https://www.amacad.org/publications/Physics_of_Space_Security.pdf [March 20, 2014].

[61] V. Labrador. (2013, Dec. 26). “Satellite communication” *Encyclopædia Britannica*. [Online]. Available: http://www.britannica.com/EBchecked/topic/524891/satellite-communication/288217/How-satellites-work [March 20, 2014].

[62] EADS Astrium. " GAIA_Auto19" [Online]. Available: https://directory.eoportal.org/web/eoportal/satellite-missions/g/gaia [March 20, 2014].

[63] ESA. (2013, March 17). *Gaia* [Online]. Available: http://sci.esa.int/gaia/40128-overview/ [March 20, 2014].

[64] P. Blau. (2013). "Gaia spacecraft overview " *Spaceflight101*. [Online]. Available: http://www.spaceflight101.com/gaia-spacecraft-overview.html [March 20, 2014].

APPENDIX A: MMOD SHIELD DESIGN AND PERFORMANCE EQUATIONS

In this appendix, the equations for designing MMOD shields as a function of the projectile's characteristics (diameter, velocity and density) and the equations for determining a shield's performance (critical projectile diameter vs. relative velocity) are given for each of the four types of shields: the Whipple shield, the stuffed Whipple shield, the meshed double-bumper shield and the multi-shock shield.

All given design and performance equations for each type of shield have been taken from Dr. E. L. Christiansen's "Handbook for Designing MMOD Protection" and "Meteoroid/Debris Shielding" [1], [2].

LIST OF FIGURES

A.1. WHIPPLE SHIELD

The original double wall shield, Figure A-1, designed by Fred Whipple in the 1940's consists of a solid aluminum bumper and rear wall. The bumper breaks up the projectile and the rear wall absorbs the impact over a larger surface. The effectiveness of this type of shield depends on the state of the debris cloud formed after the bumper; whether it contains solid, liquid or vaporized pieces of the projectile and bumper [1].

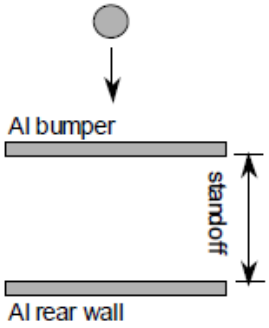

Figure A-1. Whipple shield schematic [1].

- **Design equations**

Sizing equations for simple Whipple shields valid assuming $V_n \geq 7$ km/s [1]:

$$t_b = c_b\, m_p/\rho_b = c_b d\, \rho_p/\rho_b \qquad \text{[A-1]}$$

$$t_w = c_w d^{0.5}\left(\rho_p \rho_b\right)^{1/6} {M_p}^{1/3} V_n / S^{0.5} (70/\sigma)^{0.5} \qquad \text{[A-2]}$$

Where:

$c_w = 0.16$
$d =$ projectile diameter [cm]
$M_p =$ projectile mass [g]
$\rho_b =$ outer bumper density [g/cm^3]
$\rho_p =$ projectile density [g/cm^3]
$S =$ standoff between the bumper and the rear wall [cm]
$\sigma =$ yield strength of the rear wall [ksi]
$t_b =$ outer bumper thickness [cm]
$t_w =$ thickness of the rear wall [cm]

$V_n =$ normal component of the projectile's relative velocity [km/s]

- **Performance equations**

The equations are divided into 3 velocity regions [1]:

- Low-velocity region: $V \leq 3\ km/s$
- Intermediate-velocity region: $3\ km/s < V < 7\ km/s$
- High-velocity region: $V \geq 7\ km/s$

Ballistic-limit equations for impacts in the low-velocity region [1]:

$$d_c = \left[(t_w(\sigma/40)^{0.5} + t_b)/\left(0.6\left(\cos^{5/3}\theta\right){\rho_p}^{0.5}V^{2/3}\right)\right]^{(18/19)} \quad \text{[A-3]}$$

Where:

$d_c =$ critical projectile diameter [cm]
$\theta =$ impact angle from the normal direction [deg]
$V =$ projectile's relative velocity [km/s]

Ballistic-limit equations for impacts in the high-velocity region [1]:

$$d_c = 3.918{t_w}^{2/3}{\rho_p}^{-1/3}{\rho_b}^{-1/9}(V\cos\theta)^{-2/3}S^{1/3}(\sigma/70)^{1/3} \quad \text{[A-4]}$$

Ballistic-limit equations for impacts in the intermediate-velocity region [1]:

$$d_c = \left[(t_w(\sigma/40)^{0.5} + t_b)/\left(1.248{\rho_p}^{0.5}\cos\theta\right)\right]^{(18/19)}[1.75 - (V_n/4)] \quad \text{[A-5]}$$

$$+\left[1.071{t_w}^{2/3}{\rho_p}^{-1/3}{\rho_b}^{-1/9}S^{1/3}(\sigma/70)^{1/3}\right][(V_n/4) - 0.75]$$

A.2. KEVLAR/NEXTEL STUFFED WHIPPLE SHIELD

The Kevlar/Nextel stuffed Whipple shield, Figure A-2, more effective than the simple Whipple shield, adds an intermediate layer of advanced materials such as Nextel ceramic cloth reinforced with a layer of high strength fabric such as Kevlar. This intermediate layer slows down the debris cloud and can defeat some of the particles in it, but also reduces the cloud's expansion rate [1].

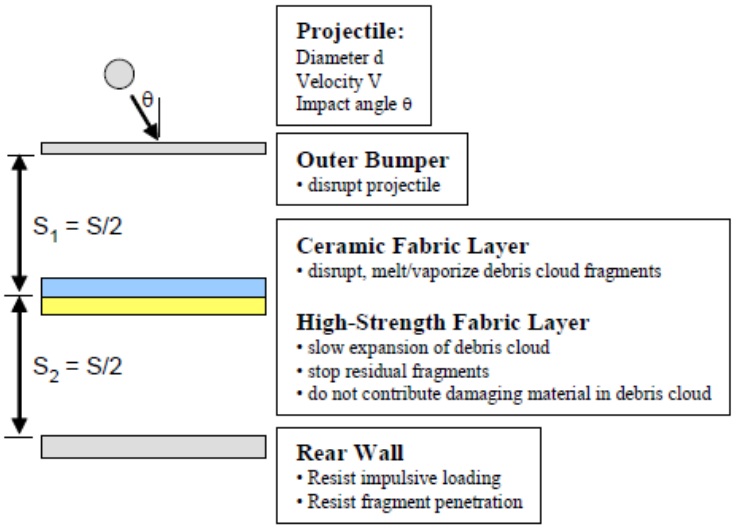

Figure A-2. Stuffed Whipple shield schematic [1].

- **Design equations**

Sizing equations for Nextel/Kevlar stuffed Whipple shields; the Nextel/Kevlar layer should go halfway between the bumper and the rear wall, and the Nextel areal density is 75% and Kevlar is 25% of the Nextel/Kevlar areal density (m_{N-K}) [1], [2]:

$$t_b = c_b d\, \rho_p / \rho_b \qquad \text{[A-6]}$$

$$m_{N-K} = c_{N-K} d \rho_p \qquad \text{[A-7]}$$

$$t_w = c_w \left[\frac{c_0 d \rho_p}{(t_b \rho_p + m_{N-K})}\right]^{1.1} \frac{M_p V_n (\cos^{0.5}\theta)}{\rho_w{}^1 S^2 (\sigma/40)^{0.5}} \qquad \text{[A-8]}$$

Where:

$c_0 = 0.38$
$c_b = 0.15$
$c_{N-K} = 0.23$
$c_w = 8.8$
$d =$ projectile diameter [cm]
$m_{N-K} =$ Nextel/Kevlar areal density [g/cm^2]
$M_p =$ projectile mass [g]
$\rho_b =$ outer bumper density [g/cm^3]
$\rho_p =$ projectile density [g/cm^3]
$\rho_w =$ rear wall density [g/cm^3]
$S =$ standoff between the bumper and the rear wall [cm]
$\sigma =$ yield strength of the rear wall [ksi]
$t_b =$ outer bumper thickness [cm]
$t_w =$ thickness of the rear wall [cm]
$\theta =$ impact angle from the normal direction [deg]
$V =$ projectile's relative velocity [km/s]
$V_n =$ normal component of the projectile's relative velocity [km/s]

- **Performance equations**

The equations are divided into 3 velocity regions [1]:

- Low-velocity region: $V \leq 2.6(\cos\theta)^{-0.5}$
- Intermediate-velocity region: $2.6(\cos\theta)^{-0.5} < V < 6.5(\cos\theta)^{-0.75}$
- High-velocity region: $V \geq 6.5(\cos\theta)^{-0.75}$

Ballistic-limit equations for impacts in the low-velocity region [1]:

$$d_c = K_{L-SW} V^{-2/3} (\cos\theta)^{-4/3} \rho_p{}^{-0.5} [t_w (\sigma/40)^{0.5} + C_L m_{b-total}] \qquad \text{[A-9]}$$

Where:

$C_L = 0.37$
$d_c =$ critical projectile diameter [cm]
$K_{L-SW} = 2.35$
$m_{b-total} = m_{bumper} + m_{Nextel} + m_{Kevlar} + m_{MLI}$

Ballistic-limit equations for impacts in the high-velocity region [39]:

$$d_c = K_{H-SW}(t_w\rho_w)^{1/3}{\rho_p}^{-1/3}(\sigma/40)^{1/6}V^{-1/3}(\cos\theta)^{-0.5}S^{2/3} \quad \text{[A-10]}$$

Where:

$$\begin{cases} K_{H-SW} = 0.6 \text{ if } m_{N-K} = 0.25m_{shield} \text{ to } 0.35m_{shield} \\ K_{H-SW} = 0.45 \text{ if } m_{N-K} = 0.1m_{shield} \text{ to } 0.15m_{shield} \end{cases}$$

$m_{shield} = m_{bumper} + m_{N-K} + m_{rear\ wall}$ [g/cm^2]

Ballistic-limit equations for impacts in the intermediate-velocity region [39]:

$$d_c = \left[\frac{K_{Li-SW}\left[t_w\left(\frac{\sigma}{40}\right)^{0.5} + C_L m_{b-total}\right]}{(\cos\theta){\rho_p}^{0.5}}\right]\left[\frac{6.5\cos^{-0.75}\theta - V}{6.5\cos^{-0.75}\theta - 2.6\cos^{-0.5}\theta}\right] \quad \text{[A-11]}$$

$$+\left[K_{Hi-SW}(t_w\rho_w)^{1/3}{\rho_p}^{-1/3}(\cos\theta)^{-0.25}S^{2/3}(\sigma/40)^{1/6}\right]\left[\frac{V - 2.6\cos^{-0.5}\theta}{6.5\cos^{-0.75}\theta - 2.6\cos^{-0.5}\theta}\right]$$

Where:

$$\begin{cases} K_{Hi-SW} = 0.321 \text{ if } m_{N-K} = 0.25m_{shield} \text{ to } 0.35m_{shield} \\ K_{Hi-SW} = 0.241 \text{ if } m_{N-K} = 0.1m_{shield} \text{ to } 0.15m_{shield} \end{cases}$$

$K_{Li-SW} = 1.243$

A.3. MESHED DOUBLE-BUMPER SHIELD

The mesh double-bumper (MDB), Figure A-3, shield adds a first aluminum mesh bumper to the concept of the stuffed Whipple shield. The aluminum mesh bumper is more effective at breaking up the projectile by creating multiple shocks; this also produces a wider angle of spread of the resulting debris cloud. Another advantage over the solid bumper is that it creates smaller and less damaging bumper fragments [1].

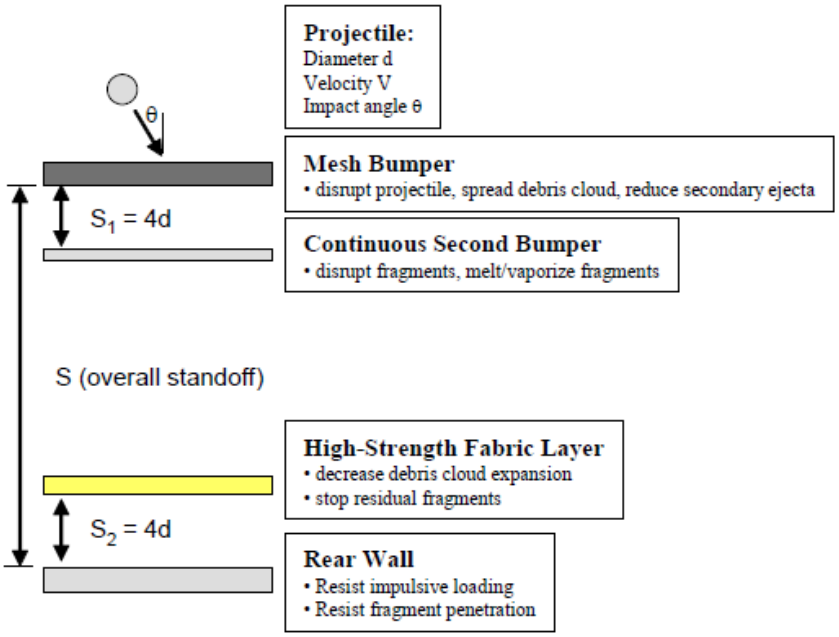

Figure A-3. Mesh double-bumper shield schematic [1].

- **Design equations**

Sizing equations for mesh double-bumper shields applicable for impacts with the following velocities [1]:

$$V \cos^{1/3} \theta > 6.4 \text{ [km/s]} \qquad \text{[A-12]}$$

The areal density of the mesh is given by the following equation and the mesh is formed by wires with a diameter from 0.07 to 0.10 times the diameter of the projectile in a square pattern:

$$m_{mesh} = 0.04 d \rho_p \quad \text{[A-13]}$$

The areal density of the solid aluminum bumper is given by the following equation and it is separated from the first bumper by a distance of $S_1 = 4d$:

$$m_{Al\_bumper} = 0.093 d \rho_p \quad \text{[A-14]}$$

The intermediate Kevlar/Nextel[2] layer is placed at a separation of $S_2 = 4d$ from the rear wall and its areal densities are determined by:

$$m_{Kevlar} = 0.064 d \rho_p \quad \text{[A-15]}$$

$$m_{Nextel} = 0.095 d \rho_p \quad \text{[A-16]}$$

The rear wall areal density is given by:

$$m_w = C_w M V_n S^{-2/3} \sigma'^{-0.5} \quad \text{[A-17]}$$

Where:

$C_w = 9$
$d =$ projectile diameter [cm]
$m_{mesh} =$ Aluminum mesh bumper areal density [g/cm^2]
$m_{Al\_bumper} =$ Aluminum bumper areal density [g/cm^2]
$m_{Kevlar} =$ intermediate Kevlar bumper areal density [g/cm^2]
$m_{Nextel} =$ intermediate Nextel bumper areal density [g/cm^2]
$m_w =$ rear wall areal density [g/cm^2]
$M =$ projectile mass [g]
$\rho_p =$ projectile density [g/cm^3]
$S =$ standoff between the bumper and the rear wall [cm]
$\sigma' =$ normalized rear wall yield stress $= \sigma/40$ [nondimensional]
$\sigma =$ yield strength of the rear wall [ksi]
$t_w =$ Aluminum rear wall thickness [cm]

[2] Nextel is optional, if it is used in the intermediate layer its areal density is determined by the given equation.

θ = impact angle from the normal direction [deg]
V = projectile's relative velocity [km/s]
V_n = normal component of the projectile's relative velocity [km/s]

- **Performance equations**

The equations are divided into 3 velocity regions [1]:

- Low-velocity region: $V \leq 2.8(\cos\theta)^{-0.5}$
- Intermediate-velocity region: $2.8(\cos\theta)^{-0.5} < V < 6.4(\cos\theta)^{-1/3}$
- High-velocity region: $V \geq 6.4(\cos\theta)^{-1/3}$

Ballistic-limit equations for impacts in the low-velocity region [1]:

$$d_c = 2.2V^{-2/3}(\cos\theta)^{-5/3}\rho_p{}^{-0.5}[t_w(\sigma/40)^{0.5} + C_L(m_b + m_{Kevlar})] \quad \text{[A-18]}$$

Where:

$C_L = 0.37$
d_c = critical projectile diameter [cm]
$m_b = m_{mesh} + m_{Al\_bumper}$ [g/cm^2]

Ballistic-limit equations for impacts in the high-velocity region [1]:

$$d_c = 0.6(t_w\rho_w)^{1/3}\rho_p{}^{-1/3}(\sigma/40)^{1/6}V^{-1/3}(\cos\theta)^{-1/3}S^{1/2} \quad \text{[A-19]}$$

Ballistic-limit equations for impacts in the intermediate-velocity region [39]:

$$d_c = \left[\frac{1.11\left[t_w\left(\frac{\sigma}{40}\right)^{0.5} + C_L(m_b + m_{Kevlar})\right]}{(\cos\theta)^{4/3}\rho_p{}^{0.5}}\right]\left[\frac{6.4\cos^{-1/3}\theta - V}{6.4\cos^{-1/3}\theta - 2.8\cos^{-0.5}\theta}\right] \quad \text{[A-20]}$$

$$+\left[0.323(t_w\rho_w)^{1/3}\rho_p{}^{-1/3}(\cos\theta)^{-2/9}S^{1/2}(\sigma/40)^{1/6}\right]\left[\frac{V - 2.8\cos^{-0.5}\theta}{6.4\cos^{-1/3}\theta - 2.8\cos^{-0.5}\theta}\right]$$

A.4. MULTI-SHOCK SHIELD

The multi-shock shield, Figure A-4, consists of 4 ceramic cloth layers with either a solid aluminum or a Kevlar rear wall. The four Nextel ceramic layers break up the projectile more effectively than a solid aluminum bumper because they produce higher shock pressures, and for the same level of protection a multi-shock shield will weigh less than a Whipple shield. The ceramic fabric bumpers also have the advantage of producing close to no secondary ejecta, or bumper fragments [1].

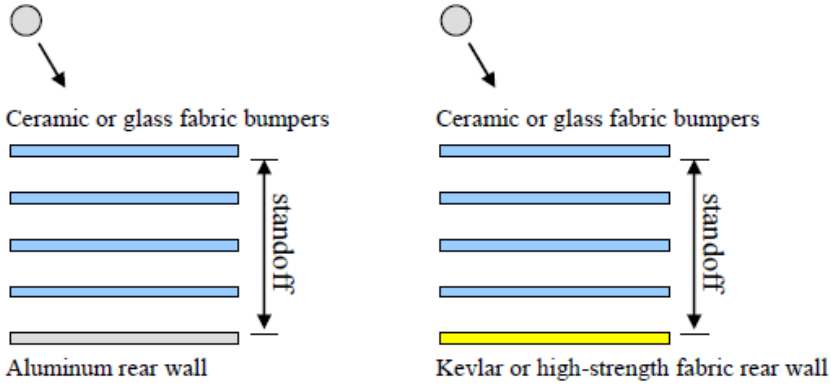

Figure A-4. Multi-shock shield schematic [1].

- **Design equations**

Sizing equations for multi-shock shields valid for impacts with the following conditions [1]:

$$\begin{cases} V > 6.4\cos^{-0.25}\theta \ \ [\mathrm{km/s}] & \text{[A-21]} \\ S/d > 15 & \text{[A-22]} \end{cases}$$

The combined areal density of the 4 Nextel bumpers is given by:

$$m_b = 0.185 d \rho_p \qquad \text{[A-23]}$$

If the rear wall is aluminum, its thickness is given by:

$$t_w = kMV_n{\rho_w}^{-1}S^{-2}\sigma'^{-0.5} \quad \text{[A-24]}$$

If the rear wall is Kevlar, its areal density is given by:

$$m_w = KMV_nS^{-2} \quad \text{[A-25]}$$

Where:

$d =$ projectile diameter [cm]
$k = 41.6$
$K = 29$
$m_b =$ combined bumper areal density [g/cm^2]
$m_w =$ Kevlar rear wall areal density [g/cm^2]
$M =$ projectile mass [g]
$\rho_p =$ projectile density [g/cm^3]
$\rho_w =$ rear wall density [g/cm^3]
$S =$ standoff between the bumper and the rear wall [cm]
$\sigma' =$ normalized rear wall yield stress $= \sigma/40$ [nondimensional]
$\sigma =$ yield strength of the rear wall [ksi]
$t_w =$ Aluminum rear wall thickness [cm]
$\theta =$ impact angle from the normal direction [deg]
$V =$ projectile's relative velocity [km/s]
$V_n =$ normal component of the projectile's relative velocity [km/s]

- **Performance equations**

The equations are divided into 3 velocity regions [1]:

- Low-velocity region: $V \leq 2.4(\cos\theta)^{-0.5}$
- Intermediate-velocity region: $2.4(\cos\theta)^{-0.5} < V < 6.4(\cos\theta)^{-0.25}$
- High-velocity region: $V \geq 6.4(\cos\theta)^{-0.25}$

– Aluminum rear wall

Ballistic-limit equations for impacts in the low-velocity region [1]:

$$d_c = K_{L-MS}V^{-2/3}(\cos\theta)^{-4/3}{\rho_p}^{-0.5}[t_w(\sigma/40)^{0.5} + C_Lm_b] \quad \text{[A-26]}$$

Where:

$C_L = 0.37$

d_c = critical projectile diameter [cm]
$K_{L-MS} = 2.0$

Ballistic-limit equations for impacts in the high-velocity region [1]:

$$d_c = K_{H-MS}(t_w\rho_w)^{1/3}{\rho_p}^{-1/3}(\sigma/40)^{1/6}V^{-1/3}(\cos\theta)^{-1/3}S^{2/3} \quad \text{[A-27]}$$

Where:

$K_{H-MS} = 0.358$

Ballistic-limit equations for impacts in the intermediate-velocity region [1]:

$$d_c = \left[\frac{K_{Li-MS}\left[t_w\left(\frac{\sigma}{40}\right)^{0.5} + C_L m_b\right]}{(\cos\theta){\rho_p}^{0.5}}\right]\left[\frac{6.4\cos^{-0.25}\theta - V}{6.4\cos^{-0.25}\theta - 2.4\cos^{-0.5}\theta}\right] \quad \text{[A-28]}$$

$$+\left[K_{Hi-MS}(t_w\rho_w)^{1/3}{\rho_p}^{-1/3}(\cos\theta)^{-0.25}S^{2/3}(\sigma/40)^{1/6}\right]\left[\frac{V - 2.4\cos^{-0.5}\theta}{6.4\cos^{-0.25}\theta - 2.4\cos^{-0.5}\theta}\right]$$

Where:

$K_{Hi-MS} = 0.193$
$K_{Li-MS} = 1.12$

– Kevlar rear wall

Ballistic-limit equations for impacts in the low-velocity region [1]:

$$d_c = K_{L-MS}V^{-2/3}(\cos\theta)^{-4/3}{\rho_p}^{-0.5}[C_w m_w + C_L m_b] \quad \text{[A-29]}$$

Where:

$C_L = 0.37$
$C_w = 0.5$
d_c = critical projectile diameter [cm]
$K_{L-MS} = 2.7$

Ballistic-limit equations for impacts in the high-velocity region [1]:

$$d_c = K_{H-MS}{m_w}^{1/3}{\rho_p}^{-1/3}V^{-1/3}(\cos\theta)^{-1/3}S^{2/3} \quad \text{[A-30]}$$

Where:

$$K_{H-MS} = 0.41$$

Ballistic-limit equations for impacts in the intermediate-velocity region [1]:

$$d_c = \left[\frac{K_{Li-MS}[C_w m_w + C_L m_b]}{(\cos\theta)\rho_p{}^{0.5}}\right]\left[\frac{6.4\cos^{-0.25}\theta - V}{6.4\cos^{-0.25}\theta - 2.4\cos^{-0.5}\theta}\right] \quad \text{[A-31]}$$

$$+\left[K_{Hi-MS} m_w{}^{1/3}\rho_p{}^{-1/3}(\cos\theta)^{-0.25}S^{2/3}\right]\left[\frac{V - 2.4\cos^{-0.5}\theta}{6.4\cos^{-0.25}\theta - 2.4\cos^{-0.5}\theta}\right]$$

Where:

$K_{Hi-MS} = 0.221$
$K_{Li-MS} = 1.506$

REFERENCES

[1] E. L. Christiansen. (2009). “Equations for Designing MMOD Shields,” in *Handbook for Designing MMOD Protection* [Online]. pp. 33-80. Available: http://ntrs.nasa.gov/archive/nasa/casi.ntrs.nasa.gov/20090010053_2009007425.pdf [Nov. 20, 2013].

[2] E. L. Christiansen. (2003). “Section 4 ballistic limit equations for spacecraft meteoroid/debris shielding,” in Meteoroid/Debris Shielding [Online] pp. 42-56. Available: http://ston.jsc.nasa.gov/collections/trs/_techrep/TP-2003-210788.pdf [Nov. 22, 2013].

APPENDIX B: MAPLE CODE FOR KINEMATIC AND DYNAMIC ANALYSIS OF THE SHIELD DEPLOYMENT MECHANISM

This appendix includes the entire Maple code used for the kinematic and dynamic analysis of the umbrella-inspired shield deployment mechanism, along with all the graphs of the variables that were determined.

The code starts on the following page.

Shield Deployment Mechanism

UMBRELLA MECHANISM

$r1 = 1137.9$

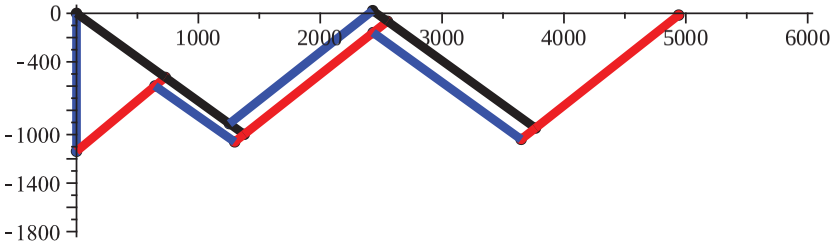

Kinematic Analysis

Position Analysis

restart

Initial Data

Accuracy and approximation: five significant numbers

$Digits := 5$:

$r1MAX := 1800.$:
$r1min := 600.$:

$r2 := 950$:
$r3 := 900.$:
$r4 := 800.$:
$r5 := 100.$:
$r6 := 800.$:
$r7 := 110.$:
$r8 := 1500.$:
$r9 := 150.$:
$r10 := 1500.$:
$r11 := 150.$:
$r12 := 1500.$:
$r13 := 150.$:
$r14 := 1500.$:
$r15 := 150.$:
$r16 := 1500.$:

$\theta 1 := evalf\left(\frac{3 \cdot \pi}{2}\right)$:
$\theta 4 := evalf(\theta 3 + \mathrm{Pi})$:
$\theta 7 := \theta 2$:
$\theta 8 := evalf(\theta 5 - \mathrm{Pi})$:
$\theta 9 := evalf(\theta 11 + \mathrm{Pi})$:
$\theta 10 := evalf(\theta 8 + \mathrm{Pi})$:
$\theta 11 := \theta 4$:
$\theta 12 := evalf(\theta 9 + \mathrm{Pi})$:
$\theta 13 := evalf(\theta 8 + \mathrm{Pi})$:
$\theta 14 := \theta 9$:
$\theta 15 := \theta 8$:
$\theta 16 := \theta 8$:

Loop1

Loop-closure equation

$R1 := r1 \cdot \langle \cos(\theta 1), \sin(\theta 1) \rangle$:
$R2 := r2 \cdot \langle \cos(\theta 2), \sin(\theta 2) \rangle$:
$R3 := r3 \cdot \langle \cos(\theta 3), \sin(\theta 3) \rangle$:

$loop1 := R1 + R2 + R3 = 0$:
Given: $r1, r2, r3, \theta 1$
Unknown: $\theta 2, \theta 3$

Calculation of vector bvec1

$bvec1 := -(R1)$:
$bvec1X := bvec1[1]$:
$bvec1Y := bvec1[2]$:
$b := \sqrt{bvec1X^2 + bvec1Y^2}$:

$\cos\alpha := \frac{bvec1X}{b}$:

$sin\alpha := \frac{bvec1Y}{b}$:

$\alpha := \arctan(sin\alpha, cos\alpha)$:

Calculation of unknown θ2, θ3

$ri := r2$:
$rj := r3$:
$\theta j := \theta 3$:

$Sinj := \frac{\left(b^2 - ri^2 + rj^2\right)}{2\,b \cdot rj}$:

$Sini := \frac{(b - rj \cdot Sinj)}{ri}$:

$Cosi := \frac{rj}{ri}\sqrt{1 - Sinj^2}$:

$Cosj := -\frac{ri}{rj}\sqrt{1 - Sini^2}$:

$\theta i := \arctan(Sini, Cosi)$:
$evalf(\theta i)$:
$\theta 2 := \theta i$:
$evalf\left(\frac{\theta 2 \cdot 180}{\pi}\right)$:

$\theta j := \arctan(Sinj, Cosj)$:
$evalf(\theta j)$:
$\theta 3 := \theta j$:
$evalf\left(\frac{\theta 3 \cdot 180}{\pi}\right)$:

Plots

plot(θ2, r1 = r1MAX..*r1min*, *labels* = ["r1, mm", "θ2, rad"], *title* = "θ2=f(r1)")

θ2=f(r1)

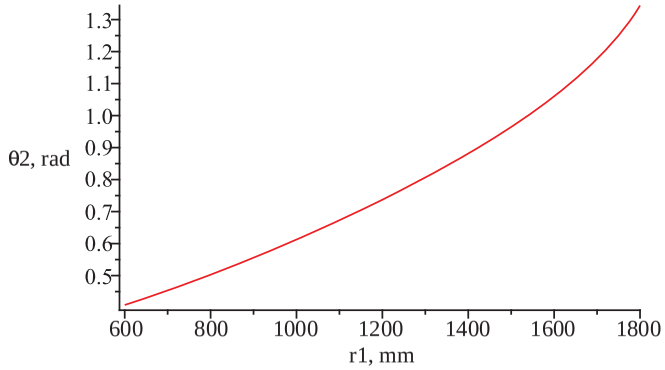

plot(θ3, r1 = r1MAX..*r1min*, *labels* = ["r1, mm", "θ3, rad"], *title* = "θ3=f(r1)")

θ3=f(r1)

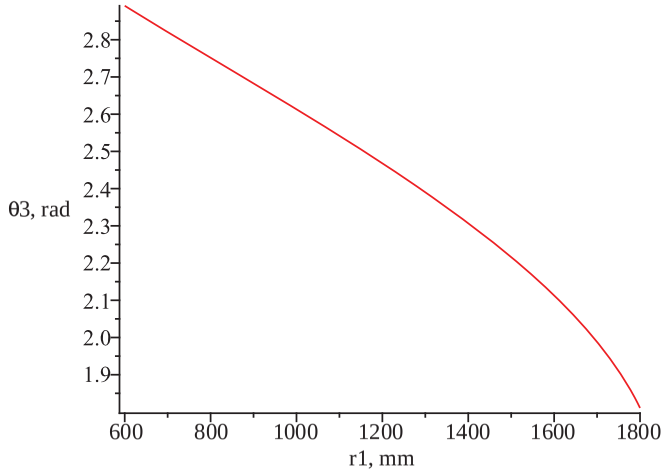

Animation

point0 := ⟨0, 0⟩ :
point1 := R1 :
point2 := -*R3* :

(1.1.1.2.5.1)

```
with(plots) :
with(geometry) :
with(plottools) :

MechAnimation :=proc(inputLength)
 global r1;
 local x0, y0, x1, y1, x2, y2, L1, L2, L3, P0, P1, P2 ;
r1 := inputLength;
x0 := point0[1];
y0 := point0[2];
x1 := point1[1];
y1 := point1[2];
x2 := point2[1];
y2 := point2[2];
 L1 := plottools[line]([x0, y0], [x1, y1], color=blue, thickness=5);
 L2 := plottools[line]([x1, y1], [x2, y2], color=red, thickness=5);
 L3 := plottools[line]([x2, y2], [x0, y0], color=black, thickness=5);
 P0 := plottools[disk]([x0, y0], 40, color=blue);
 P1 := plottools[disk]([x1, y1], 40, color=red);
 P2 := plottools[disk]([x2, y2], 40, color=black);

 plots[display](L1, L2, L3, P0, P1, P2);
 end proc:
```

(1.1.1.2.5.2)

```
animate(MechAnimation, [r1], r1=r1MAX..r1min, frames=30, trace=0, scaling
      =constrained, ); r1 :='r1':
```

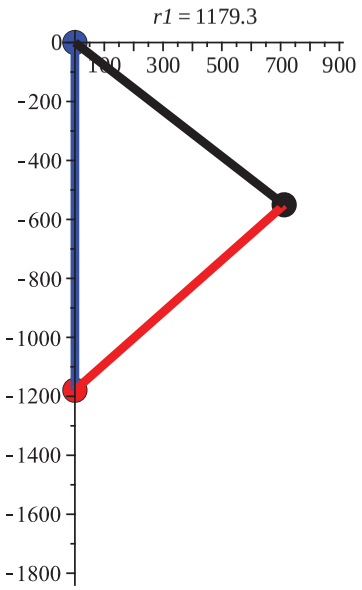

Loop2

Loop-closure equation

```
R4 := r4·⟨cos(θ4), sin(θ4)⟩ :
R5 := r5·⟨cos(θ5), sin(θ5)⟩ :
R6 := r6·⟨cos(θ6), sin(θ6)⟩ :
R7 := r7·⟨cos(θ7), sin(θ7)⟩ :


loop1 := R4 + R5 + R6 + R7 = 0 :
```

Given: r4, r5, r6, r7, θ4, θ7

Unknown: θ5, θ6

Calculation of vector bvec2

```
bvec2 := -(R4 + R7) :
bvec2X := bvec2[1] :
bvec2Y := bvec2[2] :
b2 := √(bvec2X^2 + bvec2Y^2) :
```

$cos\alpha 2 := \frac{bvec2X}{b2}$:

$sin\alpha 2 := \frac{bvec2Y}{b2}$:

$\alpha 2 := \arctan(sin\alpha 2, cos\alpha 2)$:

Calculation of unknown θ5, θ6

$ri := r5$:
$rj := r6$:
$\theta j := \theta 6$:

$A := \frac{\left(b2^2 - ri^2 + rj^2\right)}{2 \cdot b2 \cdot rj}$:

$B := \frac{(b2 - rj \cdot A)}{ri}$:

$C1 := \frac{rj}{ri}\sqrt{1 - A^2}$:

$C2 := -\frac{rj}{ri}\sqrt{1 - A^2}$:

$\theta i := \alpha 2 - \arctan(C1, B)$:
$evalf(\theta i)$:
$\theta i := \alpha 2 - \arctan(C2, B)$:
$evalf(\theta i)$:
$\theta 5 := \theta i$:
$evalf\left(\frac{\theta 5 \cdot 180}{\pi}\right)$:

$cos\alpha\theta j := \frac{(b2 - ri \cdot \cos(\alpha 2 - \theta i))}{rj}$:

$sin\alpha\theta j := -\frac{ri \cdot \sin(\alpha 2 - \theta i)}{rj}$:

(1.1.1.3.3.1)

$\theta j := \alpha 2 - \arctan(sin\alpha\theta j, cos\alpha\theta j)$:
$evalf(\theta j)$:
$\theta 6 := \theta j$:
$evalf\left(\frac{\theta 6 \cdot 180}{\pi}\right)$:

Plots

plot(θ5, r1 = r1MAX..*r1min*, *labels* = ["r1, mm", "θ5, rad"], *title* = "θ5=f(r1)")

θ5=f(r1)

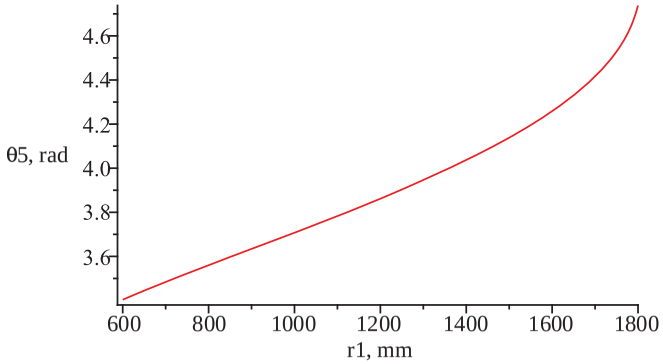

plot(θ6, r1 = r1MAX..*r1min*, *labels* = ["r1, mm", "θ6, rad"], *title* = "θ6=f(r1)")

θ6=f(r1)

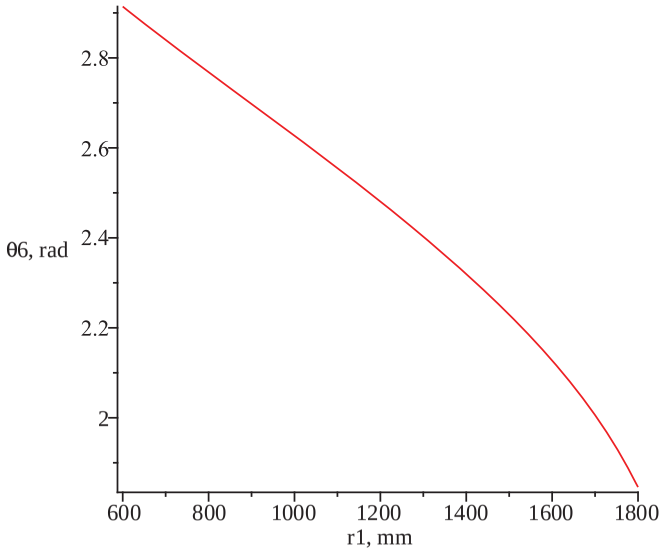

Animation

$point2 := \langle 0, 0 \rangle$:
$point3 := R4$:

```
point4 := R4 + R5 :
point5 := -R7 :

with(plots) :
with(geometry) :
with(plottools) :


MechAnimation :=proc(inputLength)
 global r1;
 local x1, y1, x2, y2, x3, y3, x4, y4, L4, L5, L6, P2, P3, P4, P5;
r1 := inputLength;
x1 := point2[1];
y1 := point2[2];
x2 := point3[1];
y2 := point3[2];
x3 := point4[1];
y3 := point4[2];
x4 := point5[1];
y4 := point5[2];
 L4 := plottools[line]([x1, y1], [x2, y2], color=blue, thickness=5);
 L5 := plottools[line]([x2, y2], [x3, y3], color=red, thickness=5);
 L6 := plottools[line]([x3, y3], [x4, y4], color=black, thickness=5);
 P2 := plottools[disk]([x1, y1], 40, color=blue);
 P3 := plottools[disk]([x4, y4], 40, color=black);
 P4 := plottools[disk]([x2, y2], 40, color=red);
 P5 := plottools[disk]([x3, y3], 40, color=red);

 plots[display](L4, L5, L6, P2, P3, P4, P5);
  end proc:


animate(MechAnimation, [r1], r1=r1MAX..r1min, frames=30, trace=0, scaling
      =constrained, ); r1 :='r1':
```

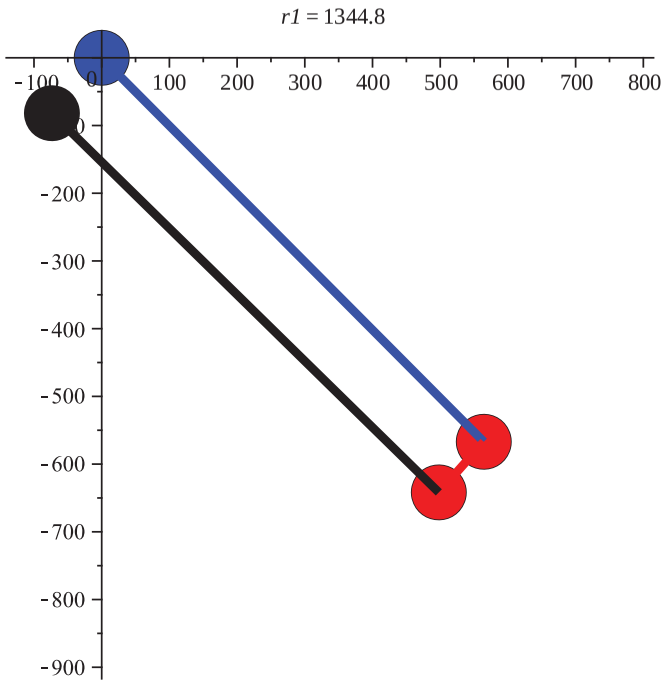

Loop3

Loop-closure equation

$R8 := r8 \cdot \langle \cos(\theta 8), \sin(\theta 8) \rangle$:
$R9 := r9 \cdot \langle \cos(\theta 9), \sin(\theta 9) \rangle$:
$R10 := r10 \cdot \langle \cos(\theta 10), \sin(\theta 10) \rangle$:
$R11 := r11 \cdot \langle \cos(\theta 11), \sin(\theta 11) \rangle$:

4 bar mechanism with oppsite sides parallel and equal length --> all angles known already

Plots

plot(θ9, r1 = r1MAX..*r1min*, *labels* = ["r1, mm", "θ9, rad"], *title* = "θ9=f(r1)")

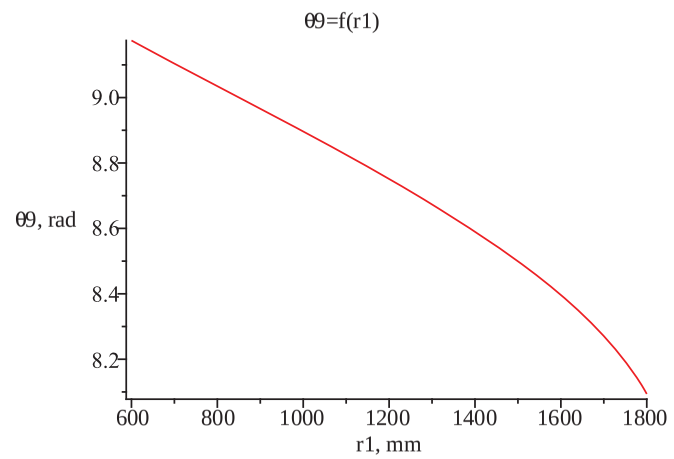

plot(θ10, r1 = r1MAX..*r1min*, *labels* = ["r1, mm", "θ10, rad"], *title* = "θ10=f(r1)")

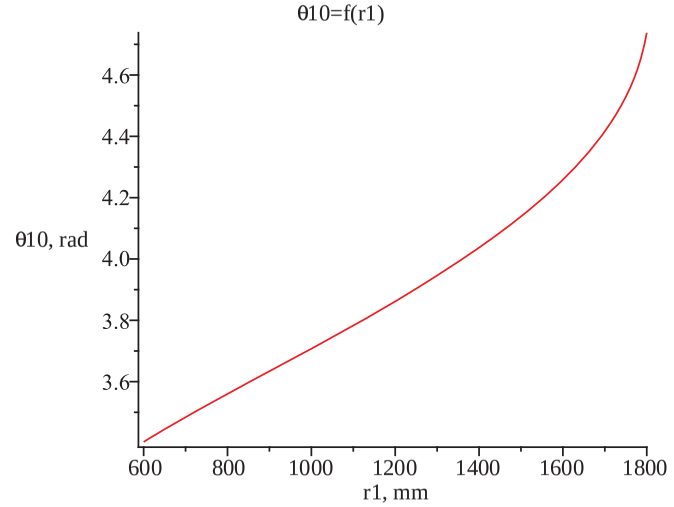

Animation

point3 := ⟨0, 0⟩ :
point6 := *R8* :
point7 := *R8* + *R9* :
point8 := -*R11* :

with(*plots*) :
with(*geometry*) :
with(*plottools*) :

MechAnimation := **proc**(*inputLength*)
global *r1*;
local *x1*, *y1*, *x2*, *y2*, *x3*, *y3*, *x4*, *y4*, *L8*, *L9*, *L10*, *P3*, *P6*, *P7*, *P8*;
r1 := *inputLength*;
x1 := *point3*[1];
y1 := *point3*[2];
x2 := *point6*[1];
y2 := *point6*[2];
x3 := *point7*[1];
y3 := *point7*[2];
x4 := *point8*[1];
y4 := *point8*[2];
L8 := *plottools*[*line*]([*x1*, *y1*], [*x2*, *y2*], *color* = *blue*, *thickness* = 5);
L9 := *plottools*[*line*]([*x2*, *y2*], [*x3*, *y3*], *color* = *red*, *thickness* = 5);
L10 := *plottools*[*line*]([*x3*, *y3*], [*x4*, *y4*], *color* = *black*, *thickness* = 5);
P3 := *plottools*[*disk*]([*x1*, *y1*], 40, *color* = *blue*);
P6 := *plottools*[*disk*]([*x4*, *y4*], 40, *color* = *black*);
P7 := *plottools*[*disk*]([*x2*, *y2*], 40, *color* = *red*);
P8 := *plottools*[*disk*]([*x3*, *y3*], 40, *color* = *red*);

plots[*display*](*L8*, *L9*, *L10*, *P3*, *P6*, *P7*, *P8*);
end proc:

animate(*MechAnimation*, [*r1*], *r1* = r1MAX..*r1min*, *frames* = 30, *trace* = 0, *scaling* = *constrained*,); *r1* := '*r1*':

r1 = 1344.8

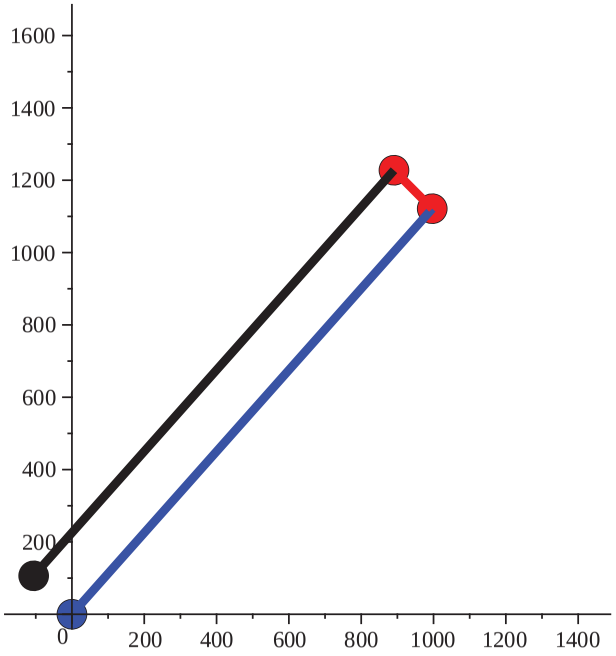

Loop4

Loop-closure equation

$R12 := r12 \cdot \langle \cos(\theta 12), \sin(\theta 12) \rangle$:
$R13 := r13 \cdot \langle \cos(\theta 13), \sin(\theta 13) \rangle$:
$R14 := r14 \cdot \langle \cos(\theta 14), \sin(\theta 14) \rangle$:
$R15 := r15 \cdot \langle \cos(\theta 15), \sin(\theta 15) \rangle$:

4 bar mechanism with oppsite sides parallel and equal length --> all angles known already

Plots

plot(θ13, r1 = r1MAX..*r1min*, *labels* = ["r1, mm", "θ13, rad"], *title* = "θ13=f(r1)")

θ13=f(r1)

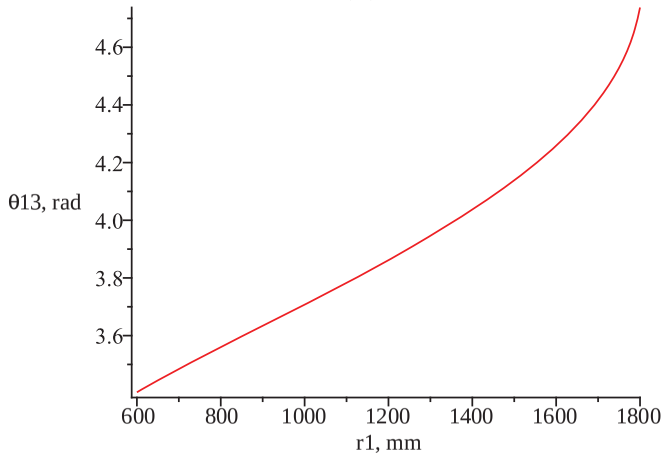

plot(θ14, r1 = r1MAX..*r1min*, *labels* = ["r1, mm", "θ14, rad"], *title* = "θ14=f(r1)")

θ14=f(r1)

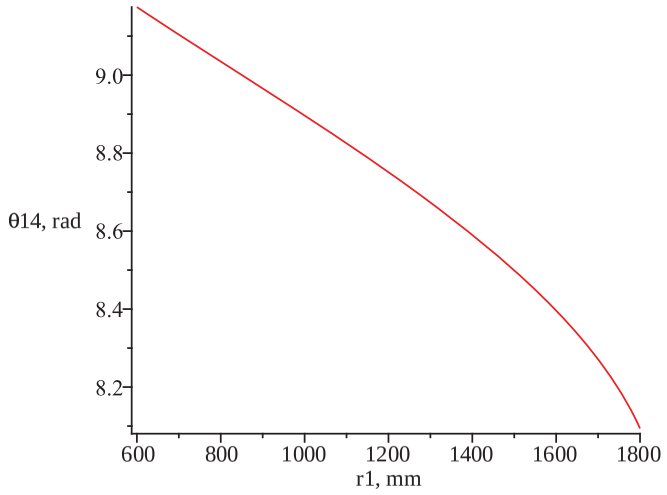

Animation

```
point6 := ⟨0, 0⟩ :
point9 := R12 :
point10 := R12 + R13 :
point11 := -R15 :

with(plots) :
with(geometry) :
with(plottools) :


MechAnimation :=proc(inputLength)
 global r1;
 local x1, y1, x2, y2, x3, y3, x4, y4, x5, y5, L12, L13, L14, P6, P9, P10, P11;
r1 := inputLength;
x1 := point6[1];
y1 := point6[2];
x2 := point9[1];
y2 := point9[2];
x3 := point10[1];
y3 := point10[2];
x4 := point11[1];
y4 := point11[2];

 L12 := plottools[line]([x1, y1], [x2, y2], color=blue, thickness=5);
 L13 := plottools[line]([x2, y2], [x3, y3], color=red, thickness=5);
 L14 := plottools[line]([x3, y3], [x4, y4], color=black, thickness=5);

 P6 := plottools[disk]([x1, y1], 40, color=blue);
 P9 := plottools[disk]([x2, y2], 40, color=blue);
 P10 := plottools[disk]([x3, y3], 40, color=red);
 P11 := plottools[disk]([x4, y4], 40, color=black);


 plots[display](L12, L13, L14, P6, P9, P10, P11);
  end proc:


animate(MechAnimation, [r1], r1=r1MAX..r1min, frames=30, trace=0, scaling
      =constrained, ); r1 :='r1':
```

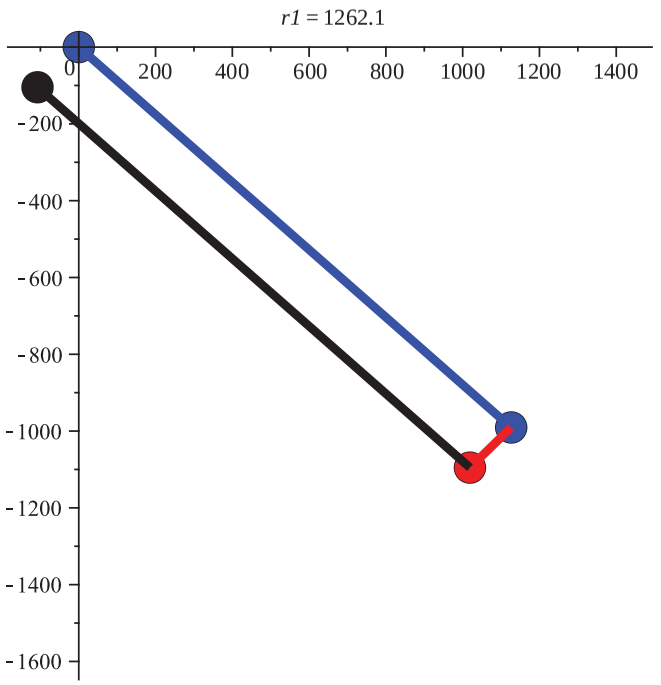

▼ *Whole Mechanism*

▼ *Loop-closure equation*

```
R16 := r16·⟨cos(θ16), sin(θ16)⟩ :
```

▼ *Plots*

```
plot(θ16, r1=r1MAX..r1min, labels=["r1, mm", "θ16, rad"], title="θ16=f(r1)")
```

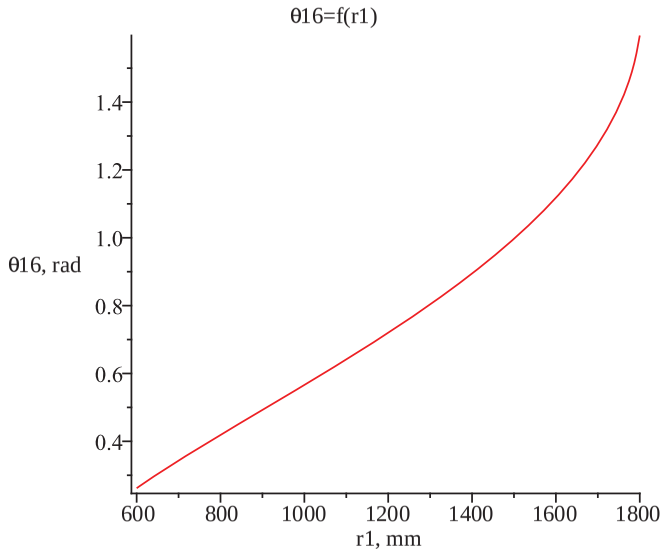

Animation

```
point0 := ⟨0, 0⟩ :
point1 := R1 :
point2 := -R3 :

point3 := point2 + R4 :
point4 := point2 + R4 + R5 :
point5 := point2 − R7 :

point6 := point3 + R8 :
point7 := point3 + R8 + R9 :
point8 := point3 − R11 :

point9 := point6 + R12 :
point10 := point6 + R12 + R13 :
point11 := point6 − R15 :

point12 := point9 + R16 :

with(plots) :
with(geometry) :
with(plottools) :
```

```
MechAnimation := proc(inputLength)
 global r1;
 local x0, y0, x1, y1, x2, y2, x3, y3, x4, y4, x5, y5, x6, y6, x7, y7, x8, y8, x9, y9, x10, y10,
      x11, y11, x12, y12, L1, L2, L3, L4, L5, L6, L7, L8, L9, L10, L12, L13, L14, L16, P0,
      P1, P2, P3, P4, P5, P6, P7, P8, P9, P10, P11, P12 ;

r1 := inputLength;
x0 := point0[1];
y0 := point0[2];
x1 := point1[1];
y1 := point1[2];
x2 := point2[1];
y2 := point2[2];

x3 := point3[1];
y3 := point3[2];
x4 := point4[1];
y4 := point4[2];
x5 := point5[1];
y5 := point5[2];

x6 := point6[1];
y6 := point6[2];
x7 := point7[1];
y7 := point7[2];
x8 := point8[1];
y8 := point8[2];

 x9 := point9[1];
y9 := point9[2];
 x10 := point10[1];
y10 := point10[2];
x11 := point11[1];
y11 := point11[2];

 x12 := point12[1];
y12 := point12[2];


 L1 := plottools[line]([x0, y0], [x1, y1], color = blue, thickness = 5);
 L2 := plottools[line]([x1, y1], [x2, y2], color = red, thickness = 5);
 L3 := plottools[line]([x2, y2], [x0, y0], color = black, thickness = 5);

 L4 := plottools[line]([x2, y2], [x3, y3], color = black, thickness = 5);
 L5 := plottools[line]([x3, y3], [x4, y4], color = red, thickness = 5);
 L6 := plottools[line]([x4, y4], [x5, y5], color = blue, thickness = 5);

  L8 := plottools[line]([x3, y3], [x6, y6], color = red, thickness = 5);
 L9 := plottools[line]([x6, y6], [x7, y7], color = black, thickness = 5);
 L10 := plottools[line]([x7, y7], [x8, y8], color = blue, thickness = 5);

 L12 := plottools[line]([x6, y6], [x9, y9], color = black, thickness = 5);
```

```
L13 := plottools[line]([x9, y9], [x10, y10], color = red, thickness = 5);
L14 := plottools[line]([x10, y10], [x11, y11], color = blue, thickness = 5);

L16 := plottools[line]([x9, y9], [x12, y12], color = red, thickness = 5);


P0 := plottools[disk]([x0, y0], 40, color = black);
P1 := plottools[disk]([x1, y1], 40, color = blue);
P2 := plottools[disk]([x2, y2], 40, color = red);

P3 := plottools[disk]([x3, y3], 40, color = black);
P4 := plottools[disk]([x4, y4], 40, color = red);
P5 := plottools[disk]([x5, y5], 40, color = blue);

P6 := plottools[disk]([x6, y6], 40, color = red);
P7 := plottools[disk]([x7, y7], 40, color = black);
P8 := plottools[disk]([x8, y8], 40, color = blue);

P9 := plottools[disk]([x9, y9], 40, color = black);
P10 := plottools[disk]([x10, y10], 40, color = red);
P11 := plottools[disk]([x11, y11], 40, color = blue);

P12 := plottools[disk]([x12, y12], 40, color = red);


plots[display](L1, L2, L3, L4, L5, L6, L8, L9, L10, L12, L13, L14, L16, P0, P1, P2, P3,
    P4, P5, P6, P7, P8, P9, P10, P11, P12);
 end proc:
```

(1.1.1.6.3.1)

```
animate(MechAnimation, [r1], r1 = r1MAX..r1min, frames = 30, trace = 0, scaling
    = constrained, ); r1 :='r1':
```


$r1 = 1262.1$

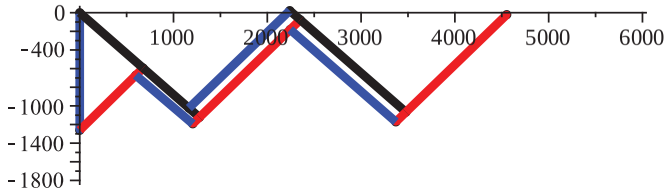

Velocity and Acceleration Analysis

Initial Data

$tf := 10.$:

$$r1 := r1MAX + \frac{(r1min - r1MAX)}{tf} \cdot t - \frac{(r1min - r1MAX)}{2 \cdot evalf(\mathrm{Pi})} \cdot \sin\left(\frac{t}{tf} \cdot 2 \cdot evalf(\mathrm{Pi})\right) :$$

$$v1 := \frac{\mathrm{d}}{\mathrm{d}\,t} r1 :$$

$$a1 := \frac{\mathrm{d}}{\mathrm{d}\,t} v1 :$$

(1.1.2.1.1)

```
plot(r1, t = 0 ..tf, labels = ["t, s", "r1, mm"], title = "r1=f(t)")
```

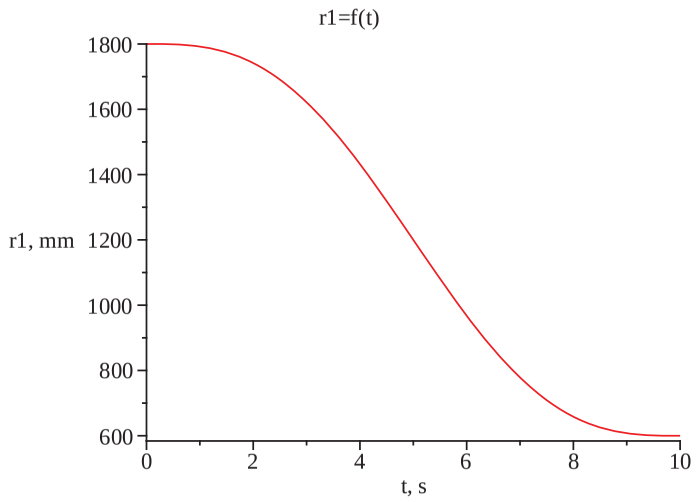

plot(v1, t = 0 ..*tf*, *labels* = ["t, s", "v1, mm/s"], *title* = "v1=f(t)")

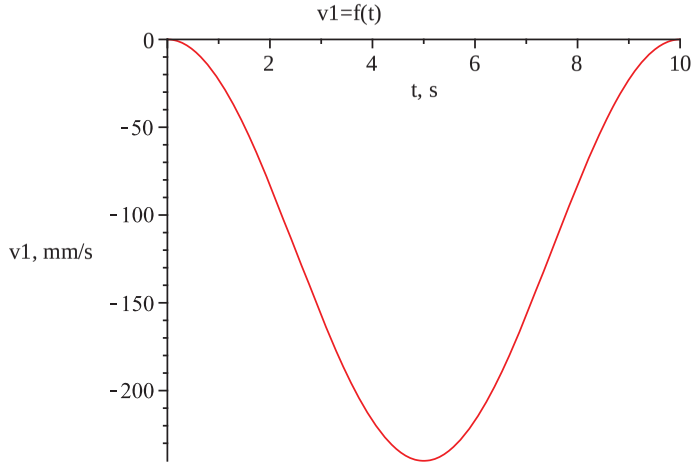

plot(a1, t = 0 ..*tf*, *labels* = ["t, s", "a1, mm/s^2"], *title* = "a1=f(t)")

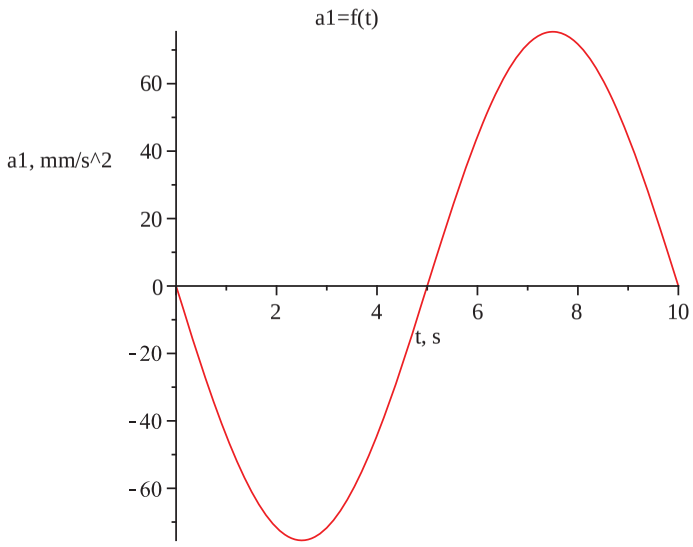

Velocity Analysis

General formula, case #4

Method

Apply the equations (2.84) and (2.85) from the textbook:

$$\omega_i r_i \sin(\theta_j - \theta_i) = -\dot{r}_i \cos(\theta_j - \theta_i) - \dot{r}_j + \dot{b}_x \cos\theta_j + \dot{b}_y \sin\theta_j \qquad (2.84)$$

$$\omega_j r_j \sin(\theta_i - \theta_j) = -\dot{r}_j \cos(\theta_i - \theta_j) - \dot{r}_i + \dot{b}_x \cos\theta_i + \dot{b}_y \sin\theta_i \qquad (2.85)$$

i=2, j=3

\# $\omega_2 r_2 \sin(\theta_3 - \theta_2) = -\dot{r}_2 \cos(\theta_3 - \theta_2) - \dot{r}_3 + \dot{b}_x \cos(\theta_3) + \dot{b}_y \sin(\theta_3)$

\# $\dot{r}_2 = 0, \quad \dot{r}_3 = 0$

\# $\omega_2 = \dfrac{\dot{b}_x \cos(\theta_3) + \dot{b}_y \sin(\theta_3)}{r_2 \sin(\theta_3 - \theta_2)}$

\# $\omega_3 = \dfrac{\dot{b}_x \cos(\theta_2) + \dot{b}_y \sin(\theta_2)}{r_3 \sin(\theta_2 - \theta_3)}$

\# $\dot{b}_x = \dfrac{d}{dt} b_x$

\# $\dot{b}_y = \dfrac{d}{dt} b_y$

Calculation

Loop1

Link 2

$bdotX := \frac{d}{dt}(bvec1X)$:

$bdotY := \frac{d}{dt}(bvec1Y)$:

$\omega 2 := \frac{bdotX \cdot \cos(\theta 3) + bdotY \cdot \sin(\theta 3)}{r2 \cdot \sin(\theta 3 - \theta 2)}$:

$plot([r1, \omega 2, t = 0..tf], labels = ["r1, mm", "\omega 2, rad/s"], title = "\omega 2=f(r1)")$

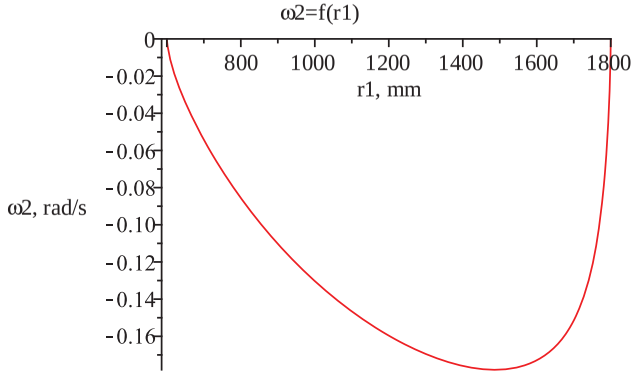

Link 3

$\omega 3 := \frac{bdotX \cdot \cos(\theta 2) + bdotY \cdot \sin(\theta 2)}{r3 \cdot \sin(\theta 2 - \theta 3)}$:

$plot([r1, \omega 3, t = 0..tf], labels = ["r1, mm", "\omega 3, rad/s"], title = "\omega 3=f(r1)")$

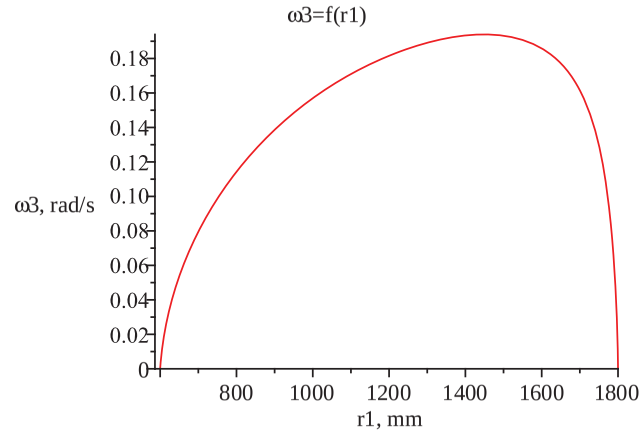

$plot(\omega 3, t = 0..tf, labels = ["t, s", "\omega 3, rad/s"], title = "\omega 3=f(t)")$

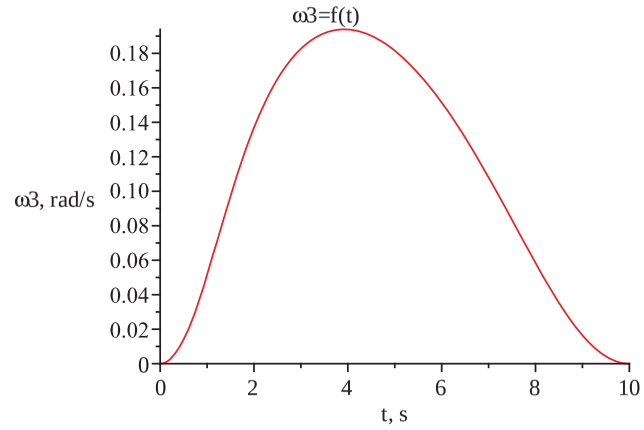

Loop3

$bvec3 := -(R8 + R11)$:
$bvec3X := bvec3[1]$:
$bvec3Y := bvec3[2]$:

Link 9

$b3dotX := \frac{d}{dt}(bvec3X)$:

$b3dotY := \frac{d}{dt}(bvec3Y)$:

$\omega 9 := \frac{b3dotX \cdot \cos(\theta 10) + b3dotY \cdot \sin(\theta 10)}{r9 \cdot \sin(\theta 10 - \theta 9)}$:

$plot([r1, \omega 9, t = 0..tf], labels = ["r1, mm", "\omega 9, rad/s"], title = "\omega 9=f(r1)")$

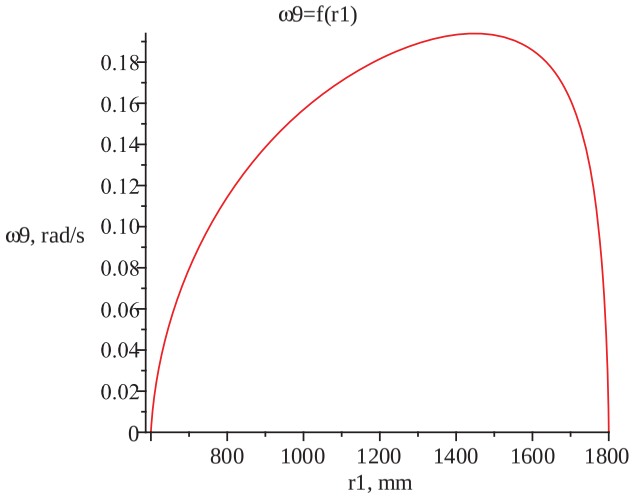

Link 10

$\omega 10 := \frac{b3dotX \cdot \cos(\theta 9) + b3dotY \cdot \sin(\theta 9)}{r10 \cdot \sin(\theta 9 - \theta 10)}$:

$plot([r1, \omega 10, t = 0..tf], labels = ["r1, mm", "\omega 10, rad/s"], title = "\omega 10=f(r1)")$

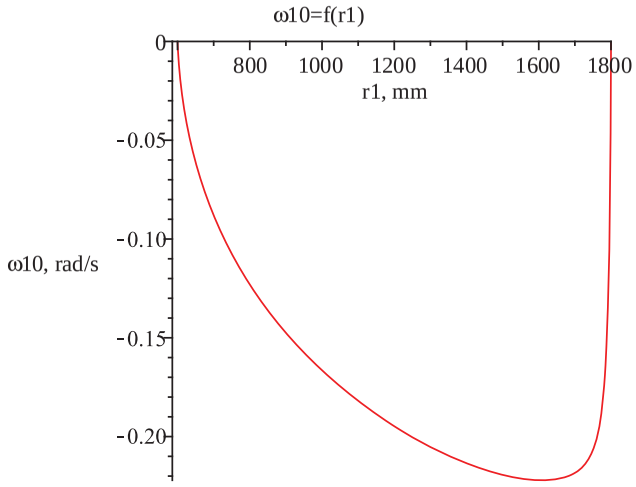

Loop4

$bvec4 := -(R12 + R15)$:
$bvec4X := bvec4[1]$:
$bvec4Y := bvec4[2]$:

Link 13

$b4dotX := \frac{d}{dt}(bvec4X)$:

$b4dotY := \frac{d}{dt}(bvec4Y)$:

$\omega 13 := \frac{b4dotX \cdot \cos(\theta 14) + b4dotY \cdot \sin(\theta 14)}{r13 \cdot \sin(\theta 14 - \theta 13)}$:

$plot([r1, \omega 13, t = 0..tf], labels = ["r1, mm", "\omega 13, rad/s"], title = "\omega 13=f(r1)")$

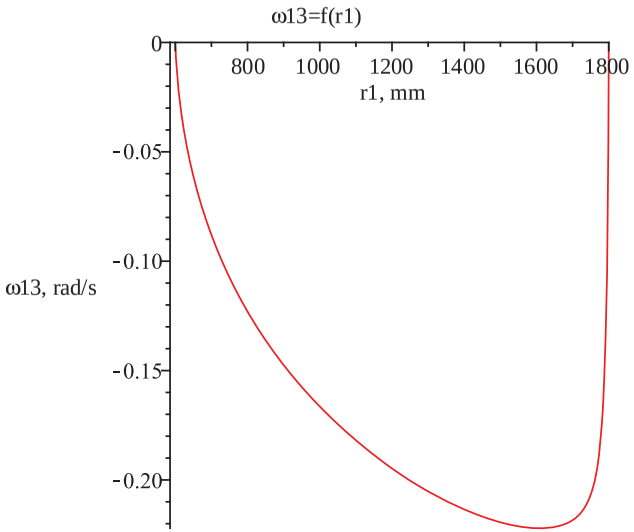

Link 14

$$\omega 14 := \frac{b4dotX\cdot\cos(\theta 13) + b4dotY\cdot\sin(\theta 13)}{r14\cdot\sin(\theta 13 - \theta 14)} :$$

$$plot([r1, \omega 14, t = 0..tf], labels = ["r1, mm", "\omega 14, rad/s"], title = "\omega 14=f(r1)")$$

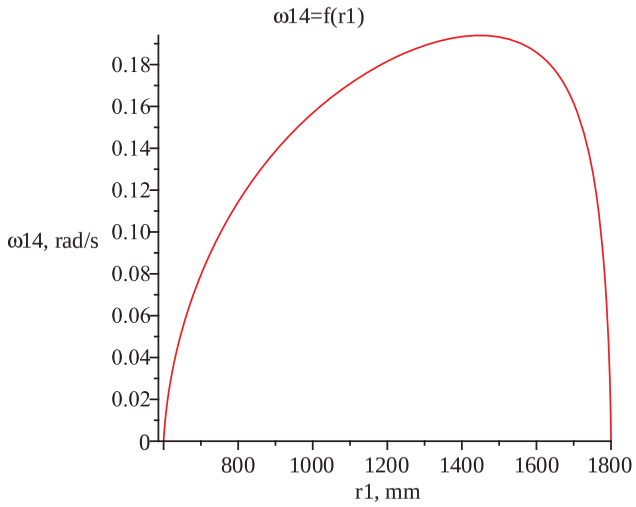

Acceleration Analysis

General formula, case #4

Method

Apply the equations (2.121) and (2.122) from the textbook:

$$\alpha_i = \frac{1}{r_i \sin(\theta_j - \theta_i)} \begin{matrix}[(-\omega_i r_i(\omega_j - \omega_i) - \ddot{r}_i)\cos(\theta_j - \theta_i) + \dot{r}_i(\omega_j - 2\omega_i)\sin(\theta_j - \theta_i) \\ -\ddot{r}_j + (\ddot{b}_x + \dot{b}_y\omega_j)\cos\theta_j + (\ddot{b}_y - \dot{b}_x\omega_j)\sin\theta_j]\end{matrix} \quad (2.121)$$

$$\alpha_j = \frac{1}{r_j \sin(\theta_i - \theta_j)} \begin{matrix}[(-\omega_j r_j(\omega_i - \omega_j) - \ddot{r}_j)\cos(\theta_i - \theta_j) + \dot{r}_j(\omega_i - 2\omega_j)\sin(\theta_i - \theta_j) \\ -\ddot{r}_i + (\ddot{b}_x + \dot{b}_y\omega_j)\cos\theta_i + (\ddot{b}_y - \dot{b}_x\omega_i)\sin\theta_i]\end{matrix} \quad (2.122)$$

i=2, j=3

$\#\ \omega_2 r_2 \sin(\theta_3 - \theta_2) = -\dot{r}_2\cos(\theta_3 - \theta_2) - \dot{r}_3 + \dot{b}_x\cos(\theta_3) + \dot{b}_y\sin(\theta_3)$

$\#\ \dot{r}_2 = 0, \quad \dot{r}_3 = 0, \quad \ddot{r}_2 = 0, \quad \ddot{r}_3 = 0$

$$\#\ \alpha_2 = \frac{-\omega_2 r_2(\omega_3 - \omega_2)\cos(\theta_3 - \theta_2) + (\ddot{b}_x + \dot{b}_y\omega_3)\cos(\theta_3) + (\ddot{b}_y - \dot{b}_x\omega_3)\sin(\theta_3)}{r_2\sin(\theta_3 - \theta_2)}$$

$$\#\ \alpha_3 = \frac{-\omega_3 r_3(\omega_2 - \omega_3)\cos(\theta_2 - \theta_3) + (\ddot{b}_x + \dot{b}_y\omega_2)\cos(\theta_2) + (\ddot{b}_y - \dot{b}_x\omega_2)\sin(\theta_2)}{r_3\sin(\theta_2 - \theta_3)}$$

where

$$\#\ \dot{b}_x = \frac{d}{dt} b_x$$

$\dot{b}_y = \frac{d}{d\,t}\,b_y$

$\ddot{b}_x = \frac{d}{d\,t}\,\dot{b}_x$

$\ddot{b}_y = \frac{d}{d\,t}\,\dot{b}_y$

Calculation

Loop1

Link 2

$$bddotX := \frac{\mathrm{d}}{\mathrm{d}\,t}(bdotX):$$

$$bddotY := \frac{\mathrm{d}}{\mathrm{d}\,t}(bdotY):$$

$$\alpha 2 := \left(\frac{1}{r2\cdot\sin(\theta 3-\theta 2)}\left(-r2\cdot\omega 2\cdot(\omega 3-\omega 2)\cdot\cos(\theta 3-\theta 2)+(bddotX+bdotY\cdot\omega 3)\cos(\theta 3)+(bddotY-bdotX\cdot\omega 3)\sin(\theta 3)\right)\right):$$

$$plot(\alpha 2,\ t=0..tf,\ labels=["time,\ s",\ "\alpha 2,\ rad/s^2"],\ title="\alpha 2=f(t)")$$

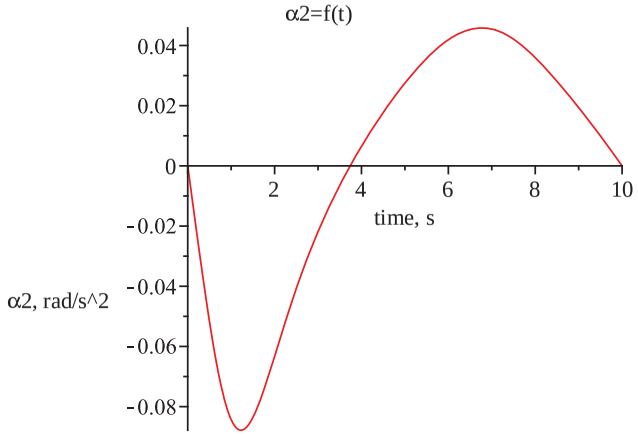

$$plot([r1,\ \alpha 2,\ t=0..tf],\ labels=["r1,\ mm",\ "\alpha 2,\ rad/s^2"],\ title="\alpha 2=f(r1)")$$

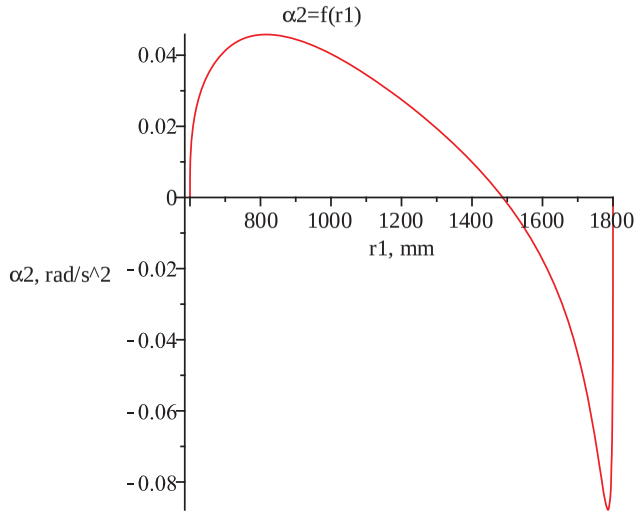

Link 3

$$\alpha 3 := \left(\frac{1}{r3\cdot\sin(\theta 2-\theta 3)}\left(-r3\cdot\omega 3\cdot(\omega 2-\omega 3)\cdot\cos(\theta 2-\theta 3)+(bddotX+bdotY\cdot\omega 2)\cos(\theta 2)+(bddotY-bdotX\cdot\omega 2)\sin(\theta 2)\right)\right):$$

$$plot(\alpha 3,\ t=0..tf,\ labels=["time,\ s",\ "\alpha 3,\ rad/s^2"],\ title="\alpha 3=f(t)")$$

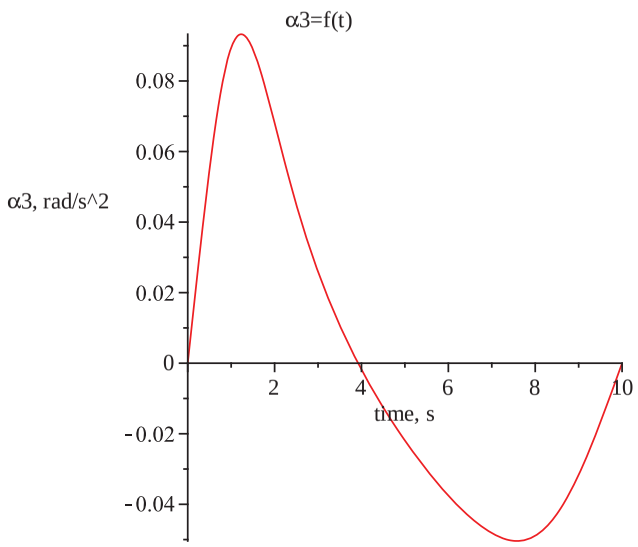

plot([*r1*, *α3*, *t* = 0 ..*tf*], *labels* = ["r1, mm", "α3, rad/s^2"], *title* = "α3=f(r1)")

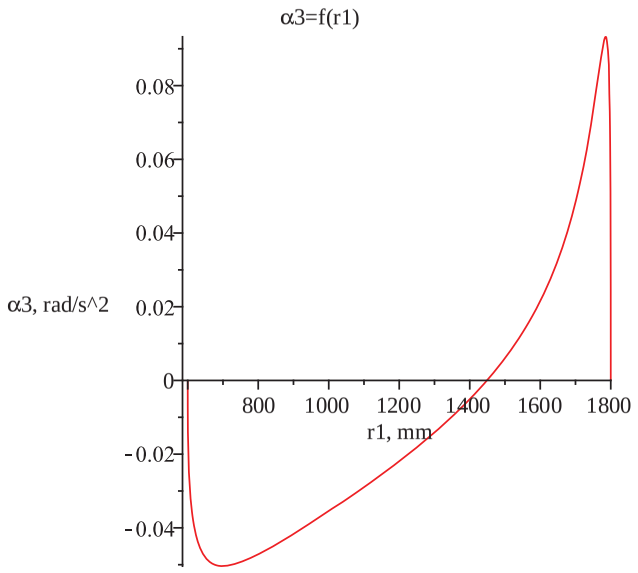

Loop3

Link 9

$$b3ddotX := \frac{d}{dt}(b3dotX):$$

$$b3ddotY := \frac{d}{dt}(b3dotY):$$

$$\alpha 9 := \left(\frac{1}{r9 \cdot \sin(\theta 10 - \theta 9)} \left(-r9 \cdot \omega 9 \cdot (\omega 10 - \omega 9) \cdot \cos(\theta 10 - \theta 9) + (b3ddotX + b3dotY \cdot \omega 10) cos(\theta 10) + (b3ddotY - b3dotX \cdot \omega 10) sin(\theta 10) \right) \right):$$

plot(*α9*, *t* = 0 ..*tf*, *labels* = ["time, s", "α9, rad/s^2"], *title* = "α9=f(t)")

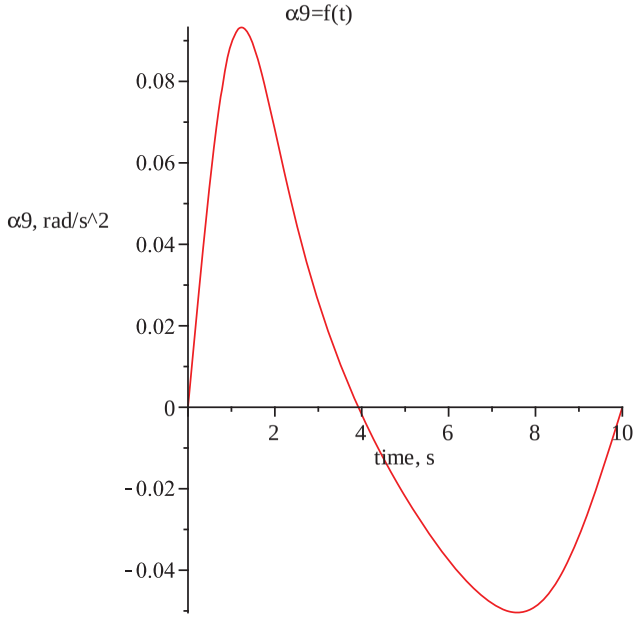

plot([*r1*, *α9*, *t* = 0 ..*tf*], *labels* = ["r1, mm", "α9, rad/s^2"], *title* = "α9=f(r1)")

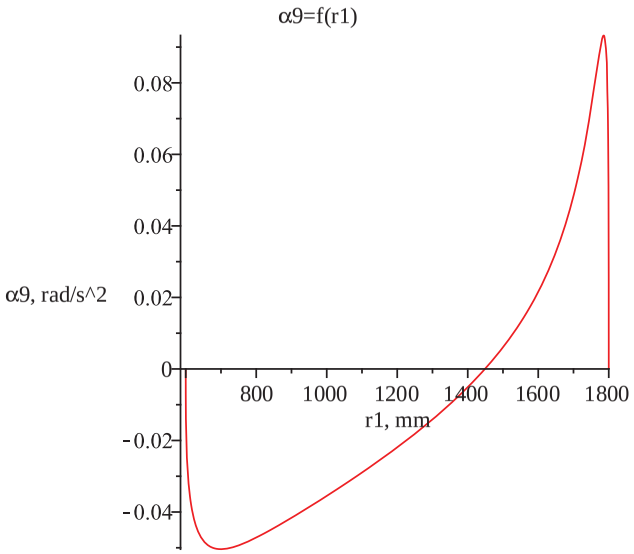

Link 10

$$\alpha 10 := \left(\frac{1}{r10 \cdot \sin(\theta 9 - \theta 10)} \left(-r10 \cdot \omega 10 \cdot (\omega 9 - \omega 10) \cdot \cos(\theta 9 - \theta 10) + (b3ddotX + b3dotY \cdot \omega 9)\cos(\theta 9) + (b3ddotY - b3dotX \cdot \omega 9)\sin(\theta 9) \right) \right) :$$

$plot(\alpha 10,\ t = 0\ ..tf,\ labels = [\text{"time, s"}, \text{"α10, rad/s^2"}],\ title = \text{"α10=f(t)"})$

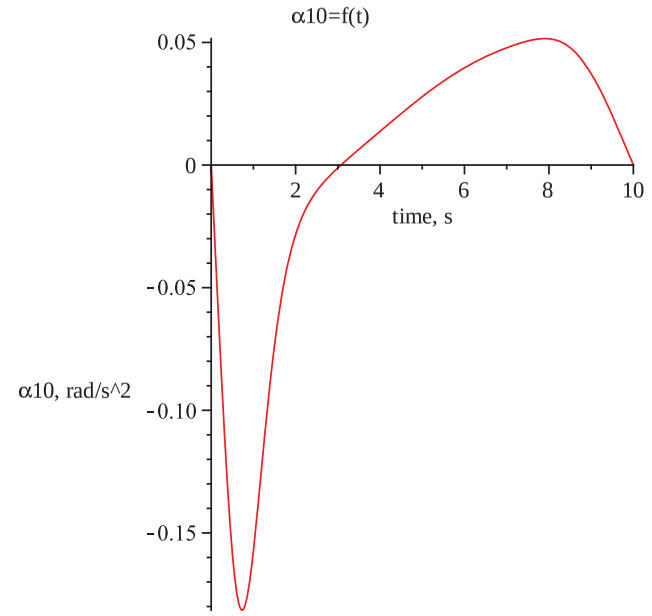

$plot([r1, \alpha 10, t = 0\ ..tf], labels = [\text{"r1, mm"}, \text{"α10, rad/s^2"}], title = \text{"α10=f(r1)"})$

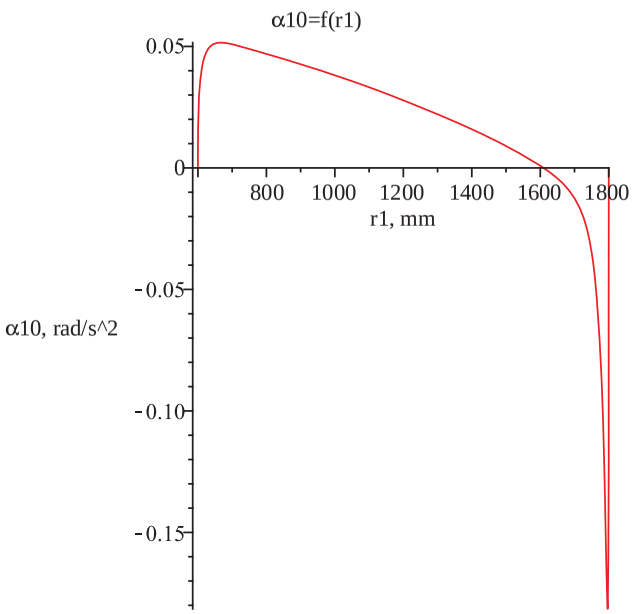

Loop4

Link 13

$$b4ddotX := \frac{d}{dt}(b4dotX):$$

$$b4ddotY := \frac{d}{dt}(b4dotY):$$

$$\alpha 13 := \left(\frac{1}{r13 \cdot \sin(\theta 14 - \theta 13)} \left(-r13 \cdot \omega 13 \cdot (\omega 14 - \omega 13) \cdot \cos(\theta 14 - \theta 13) + (b4ddotX + b4dotY \cdot \omega 14) cos(\theta 14) + (b4ddotY - b4dotX \cdot \omega 14) sin(\theta 14) \right) \right):$$

$$plot(\alpha 13, t = 0..tf, labels = ["time, s", "\alpha 13, rad/s^2"], title = "\alpha 13=f(t)")$$

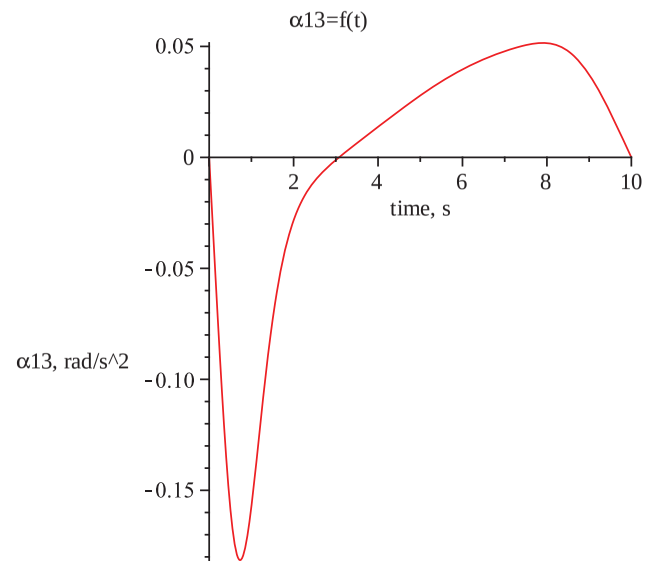

$$plot([r1, \alpha 13, t = 0..tf], labels = ["r1, mm", "\alpha 13, rad/s^2"], title = "\alpha 13=f(r1)")$$

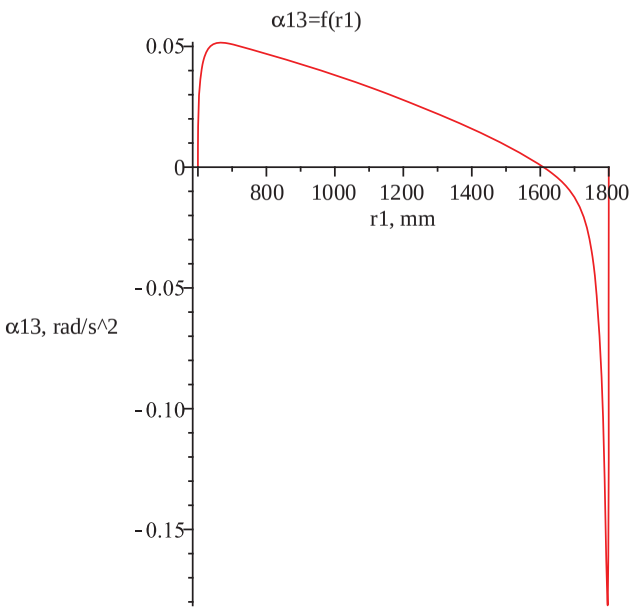

Link 14

$$\alpha 14 := \left(\frac{1}{r14 \cdot \sin(\theta 13 - \theta 14)} \left(-r14 \cdot \omega 14 \cdot (\omega 13 - \omega 14) \cdot \cos(\theta 13 - \theta 14) + (b4ddotX + b4dotY \cdot \omega 13)\cos(\theta 13) + (b4ddotY - b4dotX \cdot \omega 13)\sin(\theta 13) \right) \right) :$$

$$plot(\alpha 14,\ t = 0..tf,\ labels = [\text{"time, s"}, \text{"α14, rad/s^2"}],\ title = \text{"α14=f(t)"})$$

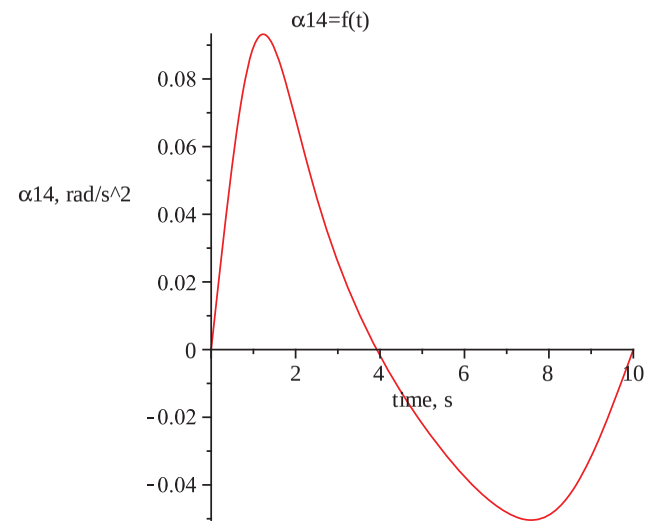

$$plot([r1, \alpha 14, t = 0..tf], labels = [\text{"r1, mm"}, \text{"α14, rad/s^2"}], title = \text{"α14=f(r1)"})$$

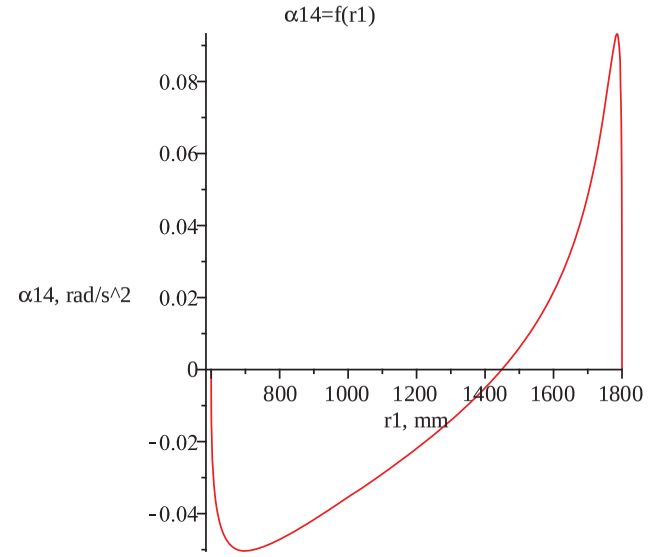

Kinetic Analysis

Initial Data

Centers of Mass (CMi), Masses (Mi) and Moments of Inertia (Ii) calculated assuming the mechanism carries 1/6 of the layer of shield in the form of a triangular plate

The triangular plate is split into 4 pieces which are carries by the top 4 links in the mechanism

$$CM1 := \frac{(r3+r4-r11)\cdot 2}{3} :$$

$$CM2 := (r10)\cdot\frac{\left(\frac{1}{2}\cdot 2\cdot(r3+r4-r11)\cdot\tan\left(\frac{\mathrm{Pi}}{8}\right)\cdot r10+\frac{2}{3}\cdot r10\cdot r10\cdot\tan\left(\frac{\mathrm{Pi}}{8}\right)\right)}{2\cdot(r3+r4-r11)\cdot\tan\left(\frac{\mathrm{Pi}}{8}\right)\cdot r10+r10\cdot r10\cdot\tan\left(\frac{\mathrm{Pi}}{8}\right)} :$$

$$CM3 := (r9+r12)\cdot\left((r9+r12)\cdot(r9+r12)\cdot\tan\left(\frac{\mathrm{Pi}}{8}\right)\cdot\frac{2}{3}+2\cdot(r9+r12)\cdot(r3+r4-r11+r10)\cdot\tan\left(\frac{\mathrm{Pi}}{8}\right)\cdot\frac{1}{2}\right)\Big/\left((r9+r12)\cdot(r9+r12)\cdot\tan\left(\frac{\mathrm{Pi}}{8}\right)+2\cdot(r9+r12)\cdot(r3+r4-r11+r10)\cdot\tan\left(\frac{\mathrm{Pi}}{8}\right)\right) :$$

$$CM4 := \mathrm{r16}\cdot\frac{\left(r16\cdot r16\cdot\tan\left(\frac{\mathrm{Pi}}{8}\right)\cdot\frac{2}{3}+2\cdot r16\cdot(r3+r4-r11+r10+r9+r12)\cdot\tan\left(\frac{\mathrm{Pi}}{8}\right)\cdot\frac{1}{2}\right)}{r16\cdot r16\cdot\tan\left(\frac{\mathrm{Pi}}{8}\right)+2\cdot r16\cdot(r3+r4-r11+r10+r9+r12)\cdot\tan\left(\frac{\mathrm{Pi}}{8}\right)} :$$

$$M1 := \frac{2\cdot(r3+r4-r11)\cdot(r3+r4-r11)\cdot\tan\left(\frac{\mathrm{Pi}}{8}\right)}{1000\cdot 1000}\cdot 2.7 :$$

$$M2 := \frac{2\cdot\left(2\cdot(r3+r4-r11)\cdot\tan\left(\frac{\mathrm{Pi}}{8}\right)\cdot r10+r10\cdot r10\cdot\tan\left(\frac{\mathrm{Pi}}{8}\right)\right)\cdot 2.7}{1000\cdot 1000} :$$

$$M3 := \frac{1}{1000\cdot 1000}\left(2\cdot\left((r9+r12)\cdot(r9+r12)\cdot\tan\left(\frac{\mathrm{Pi}}{8}\right)+2\cdot(r9+r12)\cdot(r3+r4-r11+r10)\cdot\tan\left(\frac{\mathrm{Pi}}{8}\right)\right)\cdot 2.7\right) :$$

$$M4 := \frac{1}{1000\cdot 1000}\left(2\cdot\left(r16\cdot r16\cdot\tan\left(\frac{\mathrm{Pi}}{8}\right)+2\cdot r16\cdot(r3+r4-r11+r10+r9+r12)\cdot\tan\left(\frac{\mathrm{Pi}}{8}\right)\right)\cdot 2.7\right) :$$

$$I1 := 2700\cdot\frac{2}{1000}\cdot\int_0^{\frac{r3+r4-r11}{1000}}\int_0^{2\cdot x\cdot\tan\left(\frac{\mathrm{Pi}}{8}\right)}\left(x-0-\frac{CM1}{1000}\right)^2 dy\,dx :$$

$$I2 := 2700\cdot\frac{2}{1000}\cdot\int_{\frac{r3+r4-r11}{1000}}^{\frac{r3+r4-r11+r10}{1000}}\int_0^{2\cdot x\cdot\tan\left(\frac{\mathrm{Pi}}{8}\right)}\left(x-\frac{(r3+r4-r11)}{1000}-\frac{CM2}{1000}\right)^2 dy\,dx :$$

$$I3 := 2700\cdot\frac{2}{1000}\cdot\int_{\frac{r3+r4-r11+r10}{1000}}^{\frac{r3+r4-r11+r10+r9+r12}{1000}}\int_0^{2\cdot x\cdot\tan\left(\frac{\mathrm{Pi}}{8}\right)}\left(x-\frac{(r3+r4-r11+r10)}{1000}-\frac{CM3}{1000}\right)^2 dy\,dx :$$

$$I4 := 2700\cdot\frac{2}{1000}\cdot\int_{\frac{r3+r4-r11+r10+r9+r12}{1000}}^{\frac{r3+r4-r11+r10+r9+r12+r16}{1000}}\int_0^{2\cdot x\cdot\tan\left(\frac{\mathrm{Pi}}{8}\right)}\left(x-\frac{(r3+r4-r11+r10+r9+r12)}{1000}-\frac{CM4}{1000}\right)^2 dy\,dx :$$

$$Rcm1 := point0-\frac{CM1}{r3}\cdot R3 :$$

$$Rcm2 := point8-\frac{CM2}{r10}\cdot R10 :$$

(1.2.1.1)

$$Rcm3 := point7+\frac{CM3}{r12}\cdot R12 :$$

$$Rcm4 := \mathrm{point9}+\frac{CM4}{r16}\cdot R16 :$$

Trajectories

plot([*Rcm1*[1], *Rcm1*[2], *t* = 0 ..*tf*], *labels* = ["X", "Y"], *title* = "Trajectory of CM1", *scaling* = *constrained*, *view* = [0 ..6000, 0 .. -1800])

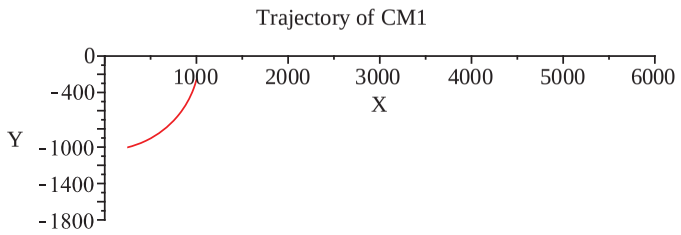

plot([*Rcm2*[1], *Rcm2*[2], *t* = 0 ..*tf*], *labels* = ["X", "Y"], *title* = "Trajectory of CM2", *scaling* = *constrained*, *view* = [0 ..6000, 0 .. - 1800])

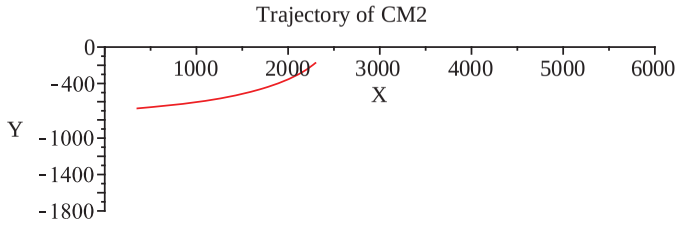

plot([*Rcm3*[1], *Rcm3*[2], *t* = 0 ..*tf*], *labels* = ["X", "Y"], *title* = "Trajectory of CM3", *scaling* = *constrained*, *view* = [0 ..6000, 0 .. - 1800])

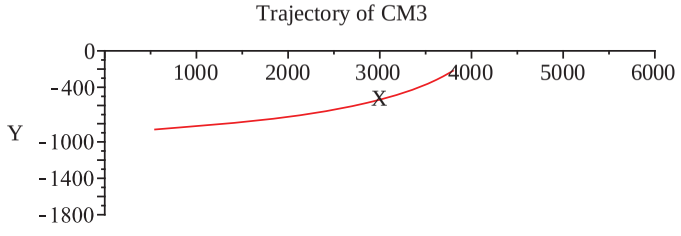

plot([*Rcm4*[1], *Rcm4*[2], *t* = 0 ..*tf*], *labels* = ["X", "Y"], *title* = "Trajectory of CM4", *scaling* = *constrained*, *view* = [0 ..6000, 0 .. - 1800])

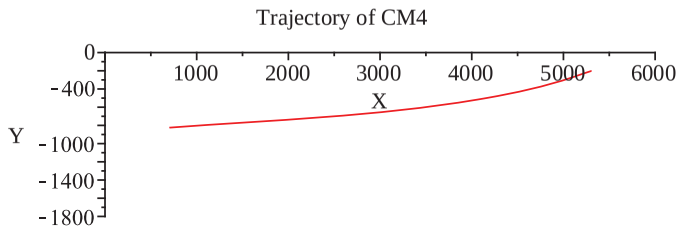

Inertial Forces

$g := 9.81$:

$$aCM1x := \frac{d}{dt}\left(\frac{d}{dt}\frac{Rcm1[1]}{1000}\right):$$
$$aCM1y := \frac{d}{dt}\left(\frac{d}{dt}\frac{Rcm1[2]}{1000}\right):$$

$FCM1x := -M1 \cdot aCM1x$:
$FCM1y := -M1 \cdot aCM1y$:

$$aCM2x := \frac{d}{dt}\left(\frac{d}{dt}\frac{Rcm2[1]}{1000}\right):$$
$$aCM2y := \frac{d}{dt}\left(\frac{d}{dt}\frac{Rcm2[2]}{1000}\right):$$

$FCM2x := -M2 \cdot aCM2x$:
$FCM2y := -M2 \cdot aCM2y$:

$$aCM3x := \frac{d}{dt}\left(\frac{d}{dt}\frac{Rcm3[1]}{1000}\right):$$
$$aCM3y := \frac{d}{dt}\left(\frac{d}{dt}\frac{Rcm3[2]}{1000}\right):$$

$FCM3x := -M3 \cdot aCM3x$:
$FCM3y := -M3 \cdot aCM3y$:

$$aCM4x := \frac{d}{dt}\left(\frac{d}{dt}\frac{Rcm4[1]}{1000}\right):$$
$$aCM4y := \frac{d}{dt}\left(\frac{d}{dt}\frac{Rcm4[2]}{1000}\right):$$

$FCM4x := -M4 \cdot aCM4x$:
$FCM4y := -M4 \cdot aCM4y$:

Plots

plot([*g*, *aCM1x*, *aCM1y*], *t* = 0 ..*tf*, *labels* = ["time, s", "aCM1, N"], *title* = "aCM1 vs g=f(t)")

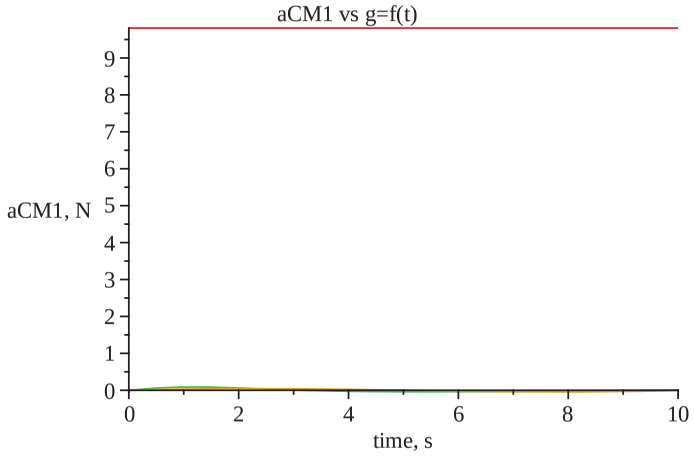

plot([*FCM1x*, *FCM1y*], *t* = 0 ..*tf*, *labels* = ["time, s", "FCM1x,FCM1y, N"], *title* = "FCM1x,FCM1y=f(t)")

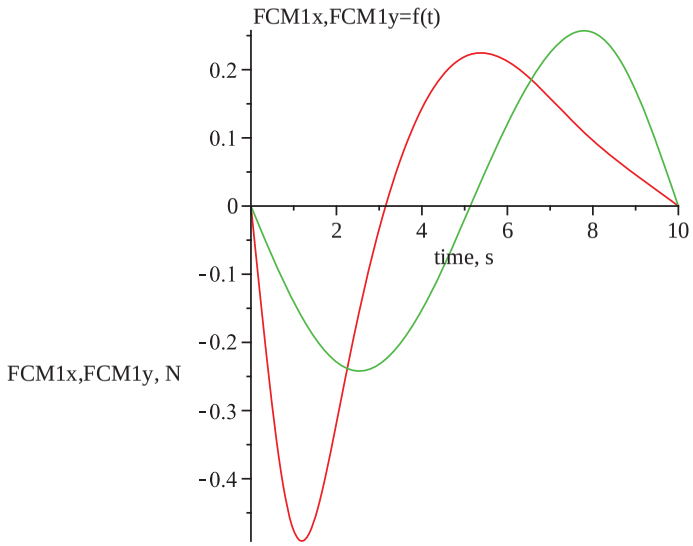

plot([*g*, *aCM2x*, *aCM2y*], *t* = 0 ..*tf*, *labels* = ["time, s", "aCM2, N"], *title* = "aCM2 vs g=f(t)")

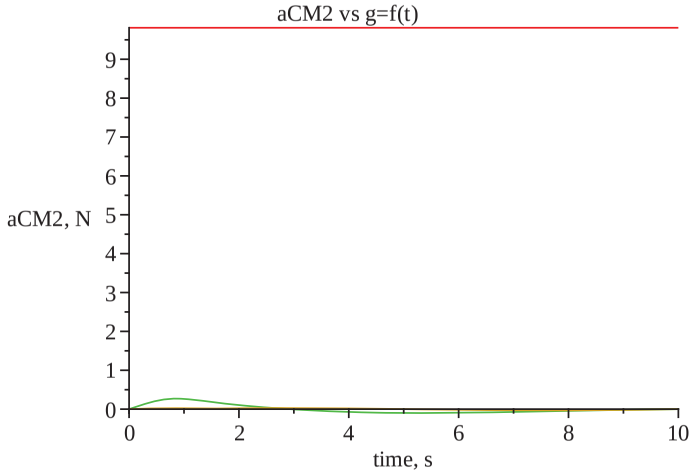

plot([*FCM2x*, *FCM2y*], *t* = 0 ..*tf*, *labels* = ["time, s", "FCM2x,FCM2y, N"], *title*

= "FCM2x,FCM2y=f(t)")

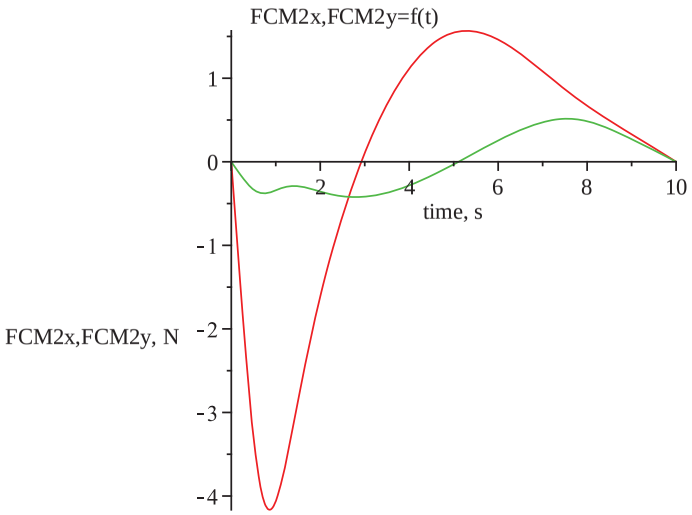

plot([*g*, *aCM3x*, *aCM3y*], *t* = 0 ..*tf*, *labels* = ["time, s", "aCM3, N"], *title* = "aCM3 vs g=f(t)")

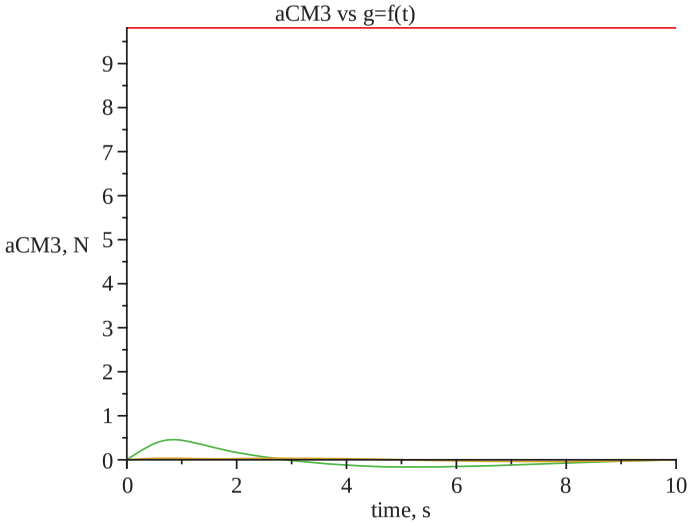

plot([*FCM3x*, *FCM3y*], *t* = 0 ..*tf*, *labels* = ["time, s", "FCM3x,FCM3y, N"], *title*

= "FCM3x,FCM3y=f(t)")

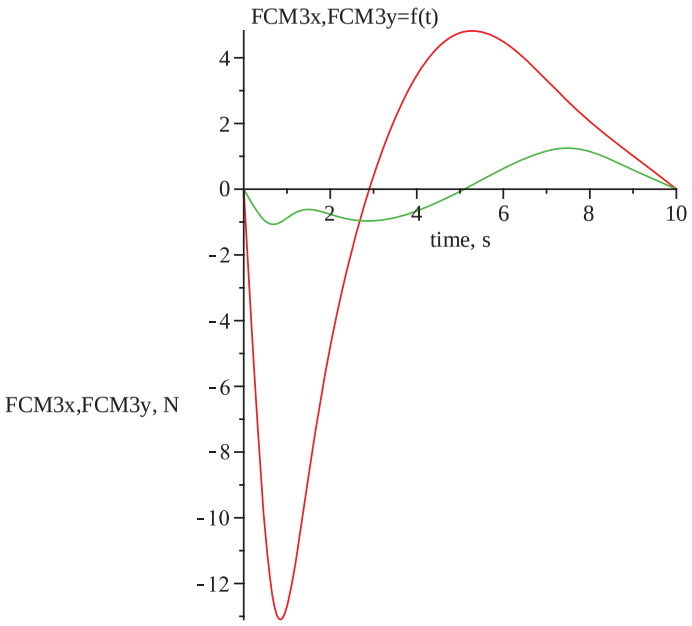

plot([*g*, *aCM4x*, *aCM4y*], *t* = 0 ..*tf*, *labels* = ["time, s", "aCM4, N"], *title* = "aCM4 vs g=f(t)")

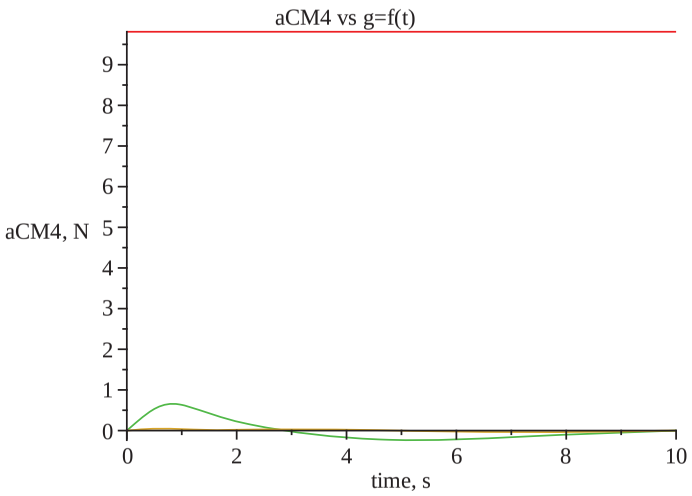

plot([*FCM4x*, *FCM4y*], *t* = 0 ..*tf*, *labels* = ["time, s", "FCM4x,FCM4y, N"], *title* = "FCM4x,FCM4y=f(t)")